WARWICK
THE UNIVERSITY OF WARWICK

A Thesis Submitted for the Degree of PhD at the University of Warwick

Permanent WRAP URL:
http://wrap.warwick.ac.uk/95085

Copyright and reuse:
This thesis is made available online and is protected by original copyright.
Please scroll down to view the document itself.
Please refer to the repository record for this item for information to help you to cite it.
Our policy information is available from the repository home page.

For more information, please contact the WRAP Team at: wrap@warwick.ac.uk

warwick.ac.uk/lib-publications

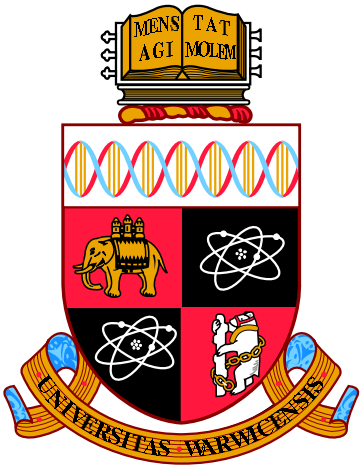

First-Principles Simulation of Functional Materials Interfaces

by

Ebiyibo Collins Ouserigha

Thesis

Submitted to the University of Warwick

for the degree of

Doctor of Philosophy

Department of Physics

April 2017

THE UNIVERSITY OF WARWICK

Contents

List of Tables **iv**

Acknowledgments **vi**

Declarations **vii**

Abstract **x**

Chapter 1 Introduction **1**

1.1 Overview 1
1.2 Structures of the Transition Metal Pnictide MnSb 4
1.3 Half-Metals 5
1.4 Electron Counting Rule for III-V Semiconductor Polar Surfaces 9
1.5 Organization of the Thesis 13

Chapter 2 Theoretical Background **15**

2.1 Density Functional Theory 15
2.2 Generalized Gradient Approximation 19
2.3 Hubbard U and DFT+U 24
2.4 Plane waves and Pseudopotentials 27
2.4.1 Plane-waves basis sets 28
2.4.2 Pseudopotentials 29
2.5 Broyden-Fletcher-Goldfarb-Shanno Scheme 33
2.6 Computational Code and Softwares 36
2.6.1 CASTEP Package 36
2.7 Surface, Slab and Interface Models 37

Chapter 3 Half-metallicity of *c*-MnSb and *c*-MnSb/InSb(111) interfaces **42**
3.1 Introduction . . . 42
3.2 Computational Methods and Calculated bulk Properties . . . 43
3.3 *c*-MnSb(111)/InSb(111) superlattices . . . 49
3.4 Summary . . . 56

Chapter 4 Ferromagnetic *n*-MnSb on III-V Semiconductors **57**
4.1 Introduction . . . 57
4.2 *n*-MnSb(0001)/InP(111) superlattices . . . 58
4.2.1 Model Preparation . . . 58
4.2.2 Results . . . 59
4.3 *n*-MnSb(0001)/GaAs(111) superlattices . . . 64
4.3.1 Model Preparation . . . 64
4.3.2 Results . . . 65
4.4 Summary . . . 68

Chapter 5 The Sb(0001)/*n*-MnSb(0001) superlattice **71**
5.1 Introduction . . . 71
5.2 Models and Computational Method . . . 75
5.3 Results . . . 76
5.4 Summary . . . 81

Chapter 6 NiO/MgO heterostructures **82**
6.1 Introduction . . . 82
6.2 NiO/MgO(111) . . . 85
6.2.1 Models and Computational Method . . . 85
6.2.2 Results . . . 85
6.3 NiO/MgO(001) . . . 92
6.3.1 Models and Computational Method . . . 92
6.3.2 Results . . . 92
6.4 NiO/MgO(110) . . . 96
6.4.1 Models and Computational Method . . . 96
6.4.2 Results . . . 98
6.5 Summary . . . 102

Chapter 7 Conclusion **103**

List of Tables

1.1 Structural properties of the three polymorphs MnSb. 5
1.2 Illustration of electron counting for the (2×2) GaAs(111)A reconstruction given in figure 1.6(a). 12

3.1 Lattice parameters (Å) of InSb and *c*-MnSb. 45
3.2 The optimized bond length between the interfacial atoms, the calculated work of separation and spin magnetic moment of the interface Mn atom for the four considered configurations of the *c*-MnSb/InSb (111) interfaces. An asterisk (∗) indicates the magnetic moment for cases where the Mn atom is located in the subinterface layer. 51

4.1 The optimized bond length (L) between the interfacial atoms and the calculated work of separation (W) for the various interface ordering studied. (the interface order Mn-P is spin polarized and more stable than others). 60
4.2 Spin polarization P and magnetic moments μ in μ_B at the *n*-MnSb(0001)/InP(111) interfaces for the first two layers of *n*-MnSb and InP slabs from the interface, for the four terminations. An asterisk (*) denotes atoms in the second atomic layer of InP slab. 62
4.3 Interfacial bond length (L) and work of separation (W) for the *n*-MnSb(0001)/GaAs(111) interfaces. 66

4.4 Spin polarization P and magnetic moments μ in μ_B at the n-MnSb(0001)/GaAs(111) interfaces for the first two layers of n-MnSb and GaAs slabs from the interface, for the four terminations. An asterisk (*) denotes atoms in the second atomic layer of GaAs slab. 68

5.1 Growth conditions for Sb/MnSb heterostructures. The Sb cap layer was deposited for 90 s while cooling from 250 to 230 $°C$. And the flux ($J_{Sb/Mn}$) was not measured between the Sb cap and MnSb(2) layer. 72
5.2 Measured a lattice parameters of the films grown compared with their bulk values. The films a lattice parameters are computed from GaAs scaling. 74
5.3 The optimized bond length (L) between the interfacial atoms, the calculated work of separation (W_R) for the various interface ordering studied and there average magnetic moments. 79
5.4 Interfacial separation for the n-MnSb/Sb(0001) interfaces, and given in brackets are changes in percentage of the interlayers. . 79

6.1 Comparison of the computed lattice parameters and band gap for MgO and NiO with previous works. 84
6.2 The calculated work of separation (W_R) for the various interface ordering studied, there optimized bond length (L) between the interfacial atoms, and the interlayer distances (d). 86
6.3 The calculated work of separation (W_R), interlayer distances and optimized bond length (L) between the interfacial atoms for the various interface ordering studied. 94
6.4 The calculated work of separation (W) and interlayer distances between the interfacial atoms for the various interface ordering studied. 100

Acknowledgments

I will like to thank my supervisor Dr. Gavin R. Bell for giving me the opportunity to work under him and for being very supportive of my research work. Niger Delta University, Wilberforce Island, Nigeria, gave me the opportunity to go on a Study Leave and supported my studies, which I am grateful for. My thanks also goes to my lovely wife Mrs Glory E. Ouserigha, for being supportive and understanding during my PhD studies. And for taking good care of our daughters, Laurel and Cherish in my absence. Also, my heartfelt appreciation goes to my family and friends, for their words of encouragement and prayers.

A special thanks goes to the following friends and colleagues: Mr. Philip Mousley for the initial proof-reading of my thesis and some suggestions for improvement, Dr. Haiyuan Wang for technical support on the calculations, useful discussions concerning my results and words of encouragement in this thesis. Dr. Christopher W. Burrows for providing the XRD and RHEED data used in chapter five. We had useful discussions and I got some advice from him. Others that contributed to the successful completion of this thesis through words of advice and encouragement are: Dr. Daesung Phark, Dr. Sepher Farahani V., Dr. Geanina Apachitei, Dr. Preye Ivry Milton, Dr. Thank-God Isaiah, Mrs Alifah Rahman, Mrs Susan Tatlock, Mrs Tombra B. Akana, Mr. Princewill B. Olali, Mr. Ayibapreye Kelvin and Miss Ebitare Ouserigha.

Declarations

I declare that this thesis contains an account of my research work carried out at the Department of Physics, University of Warwick between February 2013 and April 2017 under the supervision of Dr. Gavin R. Bell. The research reported here has not been previously submitted, wholly or in part, at this or any other academic institution for admission to a higher degree.

The results presented in this thesis have been generated via CASTEP calculations performed on several high-performance computing clusters (Syrah, Minerva, and Tinis) in both the Surface, Interface and Thin Film Group and the Centre for Scientific Computing at the University of Warwick. The results presented in this thesis have been analysed using Accelrys Materials Studio. RHEED and XRD data presented in Chapter 5 was provided by Dr. Christopher W. Burrows.

Ebiyibo Collins Ouserigha

April 2017

Work presented in this thesis that has been published or awaiting submission to a refereed journal.

- *Enhanced spin polarization at n-MnSb(0001)/InP(111) interface*, **C. E. Ouserigha**, H. Wang, C. W. Burrows and G. R. Bell (conference paper), June 2016. DOI: 10.1109/ICIPRM.2016.7528648.

- *Spin polarization enhancement at the n-MnSb(0001)/InP(111) and n-MnSb(0001)/GaAs(111) interfaces*, **C. E. Ouserigha**, H. Wang, C. W. Burrows and G. R. Bell (in preparation for submission to App. Phys. Lett.).

- *ab initio study of the stability and electronic properties at the cubic (c)-MnSb/InSb(111) interface*, **C. E. Ouserigha**, H. Wang, C. W. Burrows and G. R. Bell (in preparation for submission).

The work presented in this thesis has been presented at the following conferences.

- *First-principles investigation of atomic structure and half-metallic properties at the MnSb/InSb(111) interface*, **C. E. Ouserigha**, J. Robinson and G. R. Bell (Poster presentation), 11th international conference on the structure of surfaces, University of Warwick, Coventry, UK (21st-25th July, 2014).

- *Enhanced spin polarization at n-MnSb(0001)/InP(111) interface*, **C. E. Ouserigha**, H. Wang, C. W. Burrows and G. R. Bell (Poster presentation), Compound Semiconductor Week 2016, Toyama, Japan (26th-30th June, 2016).

- *Enhancement of spin polarization at interfaces of the novel layered structures: n-MnSb(0001)/InP(111) and n-MnSb(0001)/GaAs(111) interface*, **C. E. Ouserigha**, H. Wang, C. W. Burrows and G. R. Bell (Poster presentation), Materials Research Society fall meeting 2016, Boston, MA, USA (27th November-2nd December, 2016).

Trainings and project work undertaken by the author during this PhD.

- NAG/HECToR Training course on CASTEP in Computer Science Building, University of Warwick (25th-26th March, 2013).
- KKR Green functions for calculations of spectroscopic, transport and magnetic properties University of Warwick (9th-12th July, 2013).
- Excitations in Realistic Materials using Yambo on Massively Parallel Architectures, CECAM-HQ-EPFL, Lausanne, Switzerland (13th-17th April, 2015).
- CASTEP training workshop in Department of Materials, University of Oxford (17th-21st August, 2015).

The skills acquired from the CASTEP trainings have been implemented in this PhD work. A Research work was carried out on a joint project funded by Innovate UK and driven by a company, European Thermodynamics using the SPR-KKR skills of the author. This Project work has been successfully completed under the supervision of Prof. Julie B. Staunton at the University of Warwick in the period from 1st February to 30th April in 2016.

Abstract

The epitaxial growth of functional materials onto semiconductor substrates have successfully driven new technologies and tailor materials properties over some decades. We report on the structural, electronic and magnetic properties of several interfaces between MnSb and the III-V semiconductors (InSb, InP and GaAs) as well as the semi-metal Sb, using spin-polarized density functional theory simulations. In addition, the low index oxide interfaces between NiO and MgO were studied. This work is motivated by the potential application of these material combinations in spintronics. Spin polarization at the interfaces between MnSb and non-magnetic materials (III-V semiconductors and a semi-metal) have been predominantly computed from density functional theory calculations.

Initially, multilayers of zinc blende MnSb(111)/InSb(111) are investigated. The Mn-to-Sb termination of the interface between a zinc blende half-metallic ferromagnet, MnSb, with 100% spin polarization and InSb both in the (111) direction, is energetically more stable and maintains a high spin polarization of 92.6%. Spin polarization, which is usually reduced or destroyed at the interfaces of half-metallic ferromagnets, is seen to behave differently in the Mn-to-Sb termination of the MnSb(111)/InSb(111) interface structure. And this high spin polarization of 92.6% is injected into the first atomic layer of the InSb(111) slab, before reducing to 40.0% in the fourth atomic layer of the semiconductor slab.

Then the interfaces between niccolite (n)-MnSb(0001) and InP(111) and GaAs(111) were studied in the following chapter. The studies of the n-MnSb(0001)/InP(111) and n-MnSb(0001)/GaAs(111) interfaces show that the Mn-to-P termination of the n-MnSb(0001)/ InP(111) and Mn-to-As termination of the n-MnSb(0001)/GaAs(111) superlatices have an enhanced spin polarization of 63.9% and 61.1% respectively, which is far higher than the bulk n-MnSb spin polarization of approximately 18%. These interfaces become less energetically unfavourable than in the bulk n-MnSb, while the other possible atomic terminations at the interface are more unfavourable.

In the case of the models of Sb(0001)/n-MnSb(0001) interfaces designed. The Sb layer prevents oxidation of the MnSb surface and the Mn-to-Sb termination of these epitaxial models shows that Sb can grow on MnSb with interesting properties, which agrees with ongoing experimental results. Ionic-covalent bond mix is observed on the Mn-to-Sb termination of the Sb(0001)/n-MnSb(0001) interface, which have a reverse spin polarization of -57.7%.

At the low index interfaces NiO(111)/MgO(111), NiO(001)/MgO(001) and NiO(110)/ MgO(110) a half-metallic ferrimagnetic behaviour is seen on the Ni-to-O termination of the NiO(001)/ MgO(001) interface. Whereas the energetically more favourable Ni-to-O termination of the NiO(111)/ MgO(111) interface structure display a half-metallic like property at its interface.

The main aim of this study is to find new interfacial systems with highly spin polarized interface, which may be used for an efficient spin injection device and spin polarization calculation have revealed such interfaces.

Chapter 1

Introduction

1.1 Overview

Spintronics is an emerging field of nanotechnology that utilizes the spin state of electrons instead of their fundamental charge to process data in electronic devices. This involves the detection of electron spins and injecting it from one material to another. By utilizing the electron spin, it led to faster and higher density computer hard disk drives. For several decades now metal-based spintronics has being used in device manufacturing to make spin-valve head (in hard disk as magnetic sensor), magnetic random access memory (MRAM) and magnetic tunnel junction magnetoresistive random access memories (MTJ MRAM) devices with improved storage capacity [1, 2, 3, 4, 5]. These devices are basically made by sandwiching a non-magnetic layer (metal or insulator) in between multilayered structure of ferromagnetic materials and uses the giant magnetoresistance (GMR) or tunnel magnetoresistance (TMR) principle. Combining semiconductors with ferromagnetic materials to form heterostructures has been considered and shown to exhibit new and interesting features [6, 7]. This is expected to combine storage, detection, logic and communication capabilities on a single spintronic device [8]. New device concepts, such as a spin polarized field effect transistor (Spin FET) have been proposed [9]. In semiconductor-based spintronics devices, advantages such as increased data processing speed, improved way of storing information, decreased electric power consumption and non-volatility can be achieved when the spin degree of freedom is added to conventional electronic devices [10, 11]. A typical

spin-FET device structure is shown in figure 1.1 with a semiconductor channel between two ferromagnets. Spin-polarized charge from the source, passes through the channel to the drain. The spins in FM1 and FM2 layers can point in the same or opposite direction. The spins can process or not process, depending on the gate voltage. However, injecting an efficient spin-polarized current into the semiconductor structure from ferromagnetic contacts is a complex issue and is an important aspect of spintronic devices [12]. Spin injection is difficult due to the following reasons: conductivity mismatch, interface reactivity, chemical stability of the interface and Schottky barrier height between the ferromagnetic and semiconducting material [13, 14, 15]. Also, increase in temperature causes a reduction in the spin polarization [6].

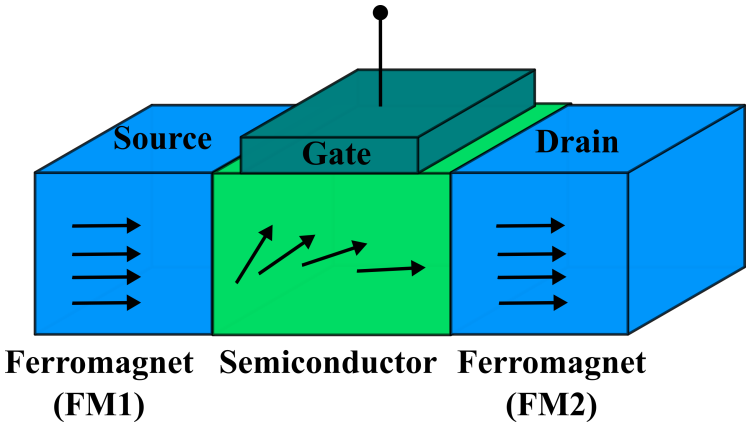

Figure 1.1: A spin polarized field effect transistor (Spin-FET) device structure.

To tackle the challenge of inefficient spin injection, either a tunnel barrier (an insulator) or an effective spin source is needed, or a structurally compatible semiconductor host which will minimise mismatch and allow a smooth transmission of the spin current generated. Presently, functional materials such as transition metal pnictides (TMP), ferromagnetic half metals (HM), antiferromagnets, functional oxides and their interfaces with semiconductors are explored [16, 17]. Antiferromagnets (e.g. NiO and CuMnAs) can complement or replace ferromagnets as the active components of spintronic devices, which are then called antiferromagnetic spintronic devices [17, 18]. The net magnetic moment of antiferromagnets is zero and its magnetism is externally invisible. This makes it a promising material for application in robust

non-volatile memory devices, such as spin transfer torque (STT) MRAM and magnetic cloaking. STT MRAM is based on magnetic switching without big magnetic fields (spin torque effect), which requires only a small bi-directional current (<150 μA) for its switching operation. While conventional MRAM is based on field induced magnetic switching and requires two high currents (>10 mA) for magnetic field generation purposes [19, 20, 21]. A STT MRAM device has the advantages of low power consumption, high storage density and easy integration with complementary metal-oxide-semiconductor (CMOS) circuits. Such a memory device has the added advantage of been robust and not susceptible to damage from an external magnetic field when made from an antiferromagnetic material due to its net magnetic moment of zero. Magnetic cloaking devices can also take advantage of the zero magnetic moment of an antiferromagnet, because, it will be impossible to detect it using regular magnetic sensors.

An efficient spin generator should have high spin polarization and it is important to measure the spin polarization of conduction electrons when investigating the electronic structure of potential materials. The available methods are spin-resolved photoemission and inverse photoemission, spin-resolved soft X-ray absorption, and transport measurements in point contacts and tunnel junctions, either with two ferromagnetic electrodes or with one ferromagnetic and one superconducting electrode [1] [22]. The degree of spin polarization can be defined in several ways and a more general definition can be written as [23]:

$$P_{nv^i} = \frac{(nv^i)_\uparrow - (nv^i)_\downarrow}{(nv^i)_\uparrow + (nv^i)_\downarrow} \tag{1.1}$$

where $n_{\uparrow(\downarrow)}$ is the density of states (DOS) at the Fermi level and $v^i_{\uparrow(\downarrow)}$ is the velocity of an electron with spin $\uparrow$ ($\downarrow$). When $i = 0$ it is called the DOS spin polarization (see equation 1.2). The velocity of the spin up ($\uparrow$) electrons could be very slow compared to the spin down ($\downarrow$) electrons even if their DOS were the same, hence a strong polarization in ballistic transport.

$$P_n = \frac{n_\uparrow - n_\downarrow}{n_\uparrow + n_\downarrow} \tag{1.2}$$

[1] http://www.nsrrc.org.tw/NsrrcWebSystem/UPLOADS\%5CCHINESE\%5CPUBLISH_YEARLY\%5C2001~2002/10-13.pdf

A half-metallic binary alloy (e.g. cubic MnSb) [6] has 100% spin polarization at the Fermi level, a high Curie temperature (above 400 K) [14, 6] and a large magnetic moment per unit cell (4.00 μ_B) which are important ingredients for a successful fabricated spintronic device to have [24, 25]. However the structures of these half-metallic binary alloys are metastable. But growing metastable half metals (HM) on III-V semiconductors could produce films with stable structures. The half-metallicity in the bulk is affected by increase in temperature and is usually not preserved at the interface [6]. Here, I will not be dealing with temperature but we are looking at the interfaces in particular.

A half-metallic binary alloy such as zinc blende MnSb has the needed structural compatibility with conventional zinc blende (ZB) semiconductors [24, 26]. Combining these two important classes of materials can pave the way for new devices with improved performance. In this work III-V semiconductors with exceptional properties and antimony (Sb) has been combined with a promising TMP MnSb by modelling their heterostructures using first principles simulation method to find new behaviors at their interface. The HM variant of nickel oxide (NiO) interfaced with the popularly used insulator material, magnesium oxide (MgO) was also studied. The TMP MnSb will be introduced briefly in the next section.

1.2 Structures of the Transition Metal Pnictide MnSb

Transition metal pnictides are made of a transition metal atom (e.g. Mn, Cr or Ni) and a pnictogen atom (e.g. Sb or As). These materials can crystalize in a range of crystallographic structures (e.g. NiAs-type, zinc blende) and MnSb is a typical example. MnSb usually forms a double hexagonal niccolite (n) structure with an ABAC stacking order and belongs to the space group $P6_3/mmc$ (see figure 1.2 (a)). The stacking arrangement is such that the transition metal occupies the 'A' sites, while the pnictogen (Group V) atom occupies the alternating 'B' and 'C' sites. Although, MnSb prefers the NiAs-type (niccolite) structure, it also exists in two other metastable (cubic [zinc blende] and wurtzite) phases [6]. Figure 1.2 gives an illustration of the three

Table 1.1: Structural properties of the three polymorphs MnSb.

Polymorph	Structure Type	Space Group	Lattice Parameter (Å)	
			a	c
n-MnSb	Niccolite	$P6_3/mmc$ (no. 194)	4.12	5.77 [14]
c-MnSb	Zinc blende	$F\bar{4}3m$ (no. 216)	6.21	6.21 [27]
w-MnSb	Wurtzite	$P6_3mc$ (no. 186)	4.29	7.00 [6]

polymorphs of MnSb, namely: (a) niccolite (n)-MnSb, (b) cubic (c)-MnSb and (c) wurtzite (w)-MnSb structures. Their crystallographic information and lattice parameters are listed in table 1.1. The atoms of a zinc blende unit cell are said to be tetrahedrally coordinated and those of a niccolite structure forms a trigonal prismatic geometry.

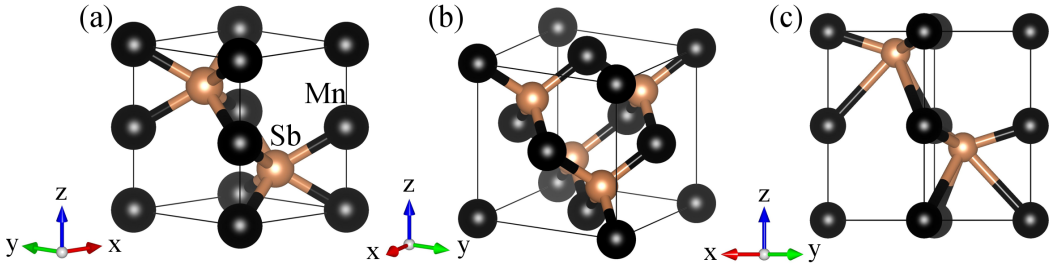

Figure 1.2: MnSb crystallizes in these Polymorphs: (a) niccolite (n) (b) cubic (c) and (c) wurtzite (w) structure.

1.3 Half-Metals

Half-Metals (HM) are materials that behave like an insulator in one spin direction and a metal in the other. Their DOS plot has 100% spin-polarized conduction electrons at the Fermi level resulting from a gap, usually in the spin-down direction [28]. HMs are mainly ferromagnetic (or ferrimagnetic), which include Heusler alloys, oxides, and binary compounds. They are ideal for spin-dependent electronics because the efficiency of any spin-dependent device is maximized if the current is 100% spin polarized. Whereas in conventional electronics the charge of the electrons plays the key role of conduction and the spin is simply used for storing information, in HM-based devices,

spin is injected from the HMs to semiconductors. It is imperative to have an efficient spin injection for the device to be effective.

The three main classes of HMs based on their crystal structure systems are: Heusler alloys (e.g. NiMnSb), oxides (e.g. CrO_2) and zinc blende (e.g. MnAs, and *c*-MnSb) type. All HMs have at least one transition metal (TM) atom (Co, Mn or Fe) in them and their *d*-states play a major part in the half-metallicity. When the *d*-states interacts with other TM atoms *d*-states, the *p*-states of oxygen atoms, pnictides or elements of Group IV, a number of distinctive properties can be seen. Due to the nature of the atoms involved and distinct crystal strucuture for each class of HM, their density of states features are dissimilar [11]. Generally the DOS shows *s*-like states from the non-TM atoms (oxygens, pnictides and Group IV elements) in the low-energy region of the valence manifold. In cubic or tetrahedral environment, TM *d*-states are divided into triply and doubly degenerate multiplets. For the cubic case, triply degenerate states are denoted t_{2g} and have lower energy compared to the doubly states designated e_g. This results as sections of the d_{xy}, d_{yz}, and d_{zx} states point in the direction of neighboring atoms while parts of the e_g states to second-nearest neighbors. The order of the two states is inverted in a tetrahedral case. Contingent upon how strong the *d*-*d* interaction amongst nearby TM elements is in relation to the *d*-*p* interaction (TM and non-TM elements), the topmost occupied states can either be *d* or *d*-*p* hybridized (see figure 1.3). The half-metallicity in all three classes of HMs is related to the *d*-*d* and *d*-*p* interactions which can be understood in terms of the crystal field, hybridization, and exchange interaction. In the next paragraph, this discussion will focus on HMs with the zinc blende structure while interested readers should look at reference [11, 10, 29] for information on Heusler alloys and the oxides types.

In the zinc blende structured HMs, the anion for bonding can be a valence IV, V or VI element whose electronegativity is weaker than that of an O atom. The anion *s* and *p* states form sp^3 type orbitals and the five-fold degenerate *d*-orbitals of the cation (a TM element) split into t_{2g} and e_g-type states as a result of the tetrahedral environment. Energies of the t_{2g} (d_{xy}, d_{yz} and d_{zx}) states are higher than those of the e_g states. The sp^3 type orbitals of the anions and linear combinations of the cations d_{xy}, d_{yz} and

d_{zx} orbitals point towards each other when close enough and then interact to form bonding and antibonding states. Given in figure 1.3 are the MnAs structure and its d-p hybridization. On the left hand side, Mn and As atoms are represented by black and pink spheres respectively. In the cubic unit cell Mn atom is positioned at $(0.25,\ 0.25,\ 0.25)a$ along the body diagonal and the primitive cell contains one atom each of Mn and As, where the lattice parameter a of MnAs is 5.77 Å. An overlap of Mn d-orbital and As sp^3 orbital is shown on the right-hand side of Fig. 1.3. This overlap generates bonding and antibonding states. The bonding states, i.e., d-p hybrid states are covalent in character (charge sharing). The p-t_{2g} hybrid states bonding has lower energy than the e_g states and more p-character. Figure 1.4 (a) depicts the schematic diagram of the ordering of orbital energies. The d-states energy

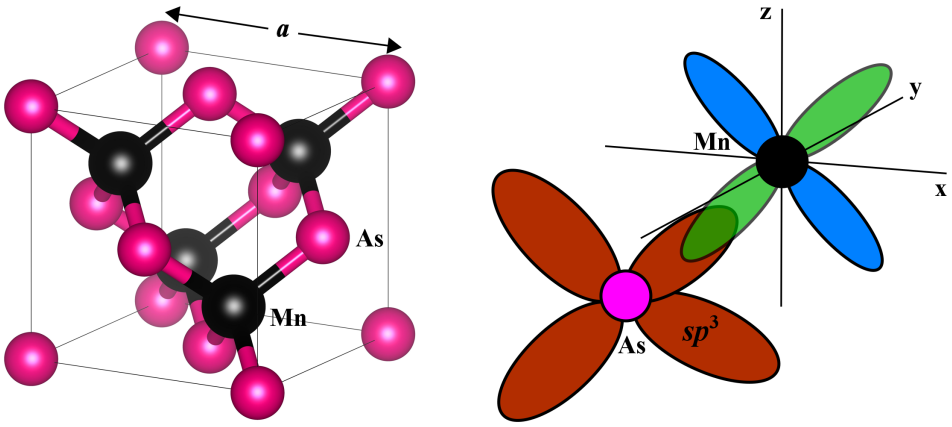

Figure 1.3: On the left hand side is the MnAs structure with Mn (As) atoms indicated by black (pink) spheres. And on the right hand side is a schematic representaion of the d-p hybridization. Figure from reference [11].

levels of a TM element is given at the left end, while on the right end s- and p-states energy levels of chalcogenide, pnictide, or carbide can be found. Crystal field splitting effects can be seen as the centre is approached. The five-fold degenerate d-states of TM atom split into triply t_{2g} and doubly e_g degenerate states due to the crystal field. sp^3-type orbitals are formed by the non-TM element. Consequential upon the d-p hybridization, are the bonding (p-t_{2g}) and antibonding (t^*_{2g}) states given at the middle of figure 1.4 (a). A DOS representation of the orbital states ordering is shown in figure 1.4 (b) and

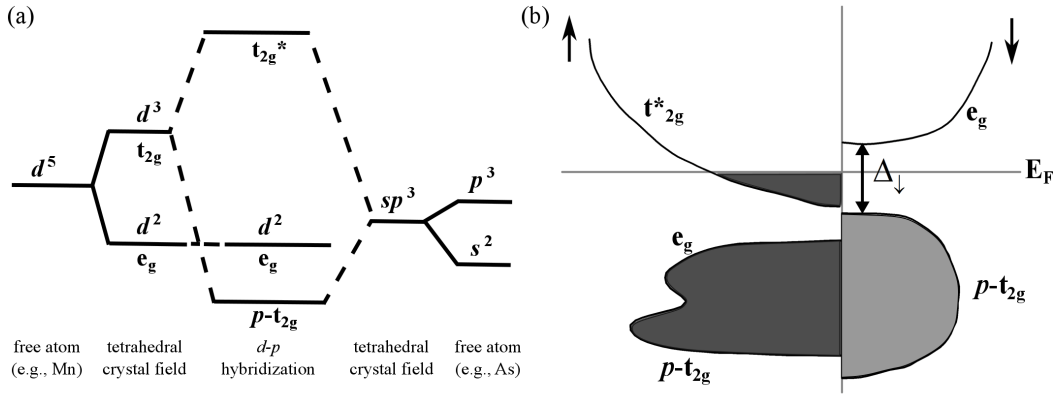

Figure 1.4: (a) Splitting from the crystal-field under tetrahedral symmetry in the $3d$ orbitals for a given spin as well as the d-p orbitals hybridization in the ZB structure. Superscripts represent degeneracy. (b) A typical DOS of an HM in the ZB structure. Figure is adapted from reference [11].

only states around the Fermi energy level E_F are visible in the diagram. The e_g (i.e d_{z^2} and $d_{x^2-y^2}$) states form the nonbonding states because they point toward second neighbors instead of the closest neighboring cations. Their energy bands can overlap with or be detached from the d-p bonding states (p-t_{2g}) and a gap is formed if they are separated. As can be seen in the spin down ($\downarrow$) channel, the bonding p-t_{2g} states and nonbonding e_g states are separated by a gap with E_F cutting through this gaps. The bonding p-t_{2g} and nonbonding e_g states in the majority-spin ($\uparrow$) states overlap as shown in the figure. A substantial anion-p character is in the bonding states whereas d-p hybrid states with mostly transition-element d character are antibonding states. In order to allow the unit cell to contain the total number of valence electrons, the smallest-energy antibonding states in the majority-spin channel are occupied owing to the exchange splitting of majority- and minority-spin states. Hence half-metallicity emerges as a result of the partial occupation (of the t^*_{2g} band) in the majority-spin channel. It is worth mentioning that among the three classes of HMs, hybridization is strongest in the zinc blende (ZB) HMs because of its d-p hybrid character near E_F. In the case of Heusler alloys and oxide HMs, d-states are the leading character near the E_F.

For stoichiometric HMs, the last occupied minority-spin band is filled (see figure 1.4 (b)) and contains an integer number of valence electrons. Hence

the magnetization M $/\mu$B $= (N_\uparrow - N_\downarrow)$ gives an integer total moment per cell. This leads to the Slater-Pauling rule which says the total magnetic moment M is given by the difference $Z - 18$ (a general expression), where Z is the total number of valence electrons [30, 31, 32].

1.4 Electron Counting Rule for III-V Semiconductor Polar Surfaces

In the preceeding section I talked about the behaviour of bulk HM, but as soon as an interface is made, the bulk symmetries will be broken and the crystal field picture no longer works because the symmetry environment is now different. I now need to think carefully about what happens at interfaces and surfaces to a HM (e.g. Does it maintain the half-metallicity?). A useful way to check if a semiconductor surface that obeys the electron counting rule is still a semiconductor (i.e not metallic at the surface) and retains its band gap at the surface is the electron counting rule. This is analogous to HM, as it is important that the minority spin gap is maintained at the interface and it does not behave metallic at the surface. Also, the Slater Pauling approach which says HMs have integer magnetic moment, could be used to check whether this carries on to the interface [32]. Metals at the surfaces generally relax because they lack directional bonding while semiconductor surfaces reconstruct because they have strongly directional bonding. HMs do have covalent bonding and they might reconstruct on their surface (or interface) [33].

The electron counting rule (ECR) is a method used for predicting the stability or properties of inorganic compounds. This method can also be extended from bulk structures to surface and interface models [34, 35, 36]. When a bulk crystal is cleaved, it forms an energetically unfavorable surface as a result of the dangling bonds (DB) formed during the cleaving process. Figure 1.5 gives an illustration of the zinc blende and niccolite surfaces that are relevant to this thesis. In figure 1.5(a) and (b) the (001) and (0001) surfaces are respectively given. The cubic system (001) face is a non-polar square symmetric surface and forms two dangling bonds per atom. The niccolite (0001) surface is a non-centrosymmetric crystal with no polarity due to the symmet-

rical stacking sequence of the three up and three down bonding, which then cancels the potential to zero. The Miller index plane (0001) is equivalent to the (001) plane. Note here that the non semiconductor surface (0001) has been included because, it is relevant to this thesis. The (110) surface depicted in figure 1.5(c) is also a non-polar surface since it has equal numbers of anions and cations. And the (111) surface of a zinc blende crystal shown in figure 1.5(d), which has alternately charged planes is polar. This is a typical Tasker type 3 surface [37].

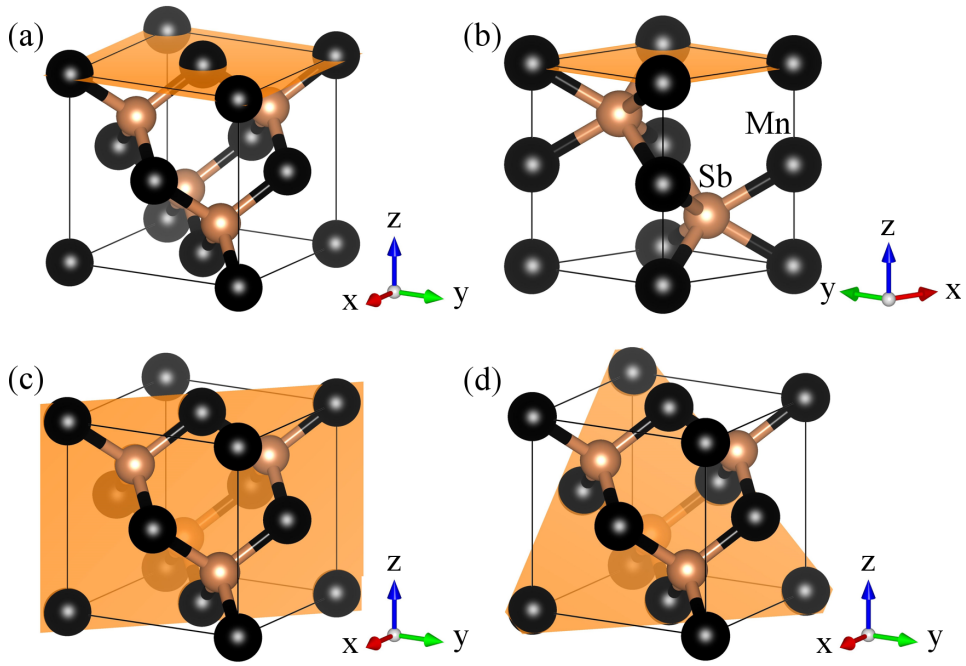

Figure 1.5: Crystal surfaces showing the: (a) (001) surface of a ZB crystal, (b) (0001) surface of a niccolite structure (e.g. *n*-MnSb), (c) (110) surface and (d) (111) surface of ZB crystal within the unit cell. The orange shaded area indicates the position of the surface plane.

The more complex surface (111), has an inequivalent number of dangling bonds at its surface. Considering the polar GaAs(111) face with two possible terminations, A and B. The surface is called (111)A surface, if it is Ga-terminated and (111)B when it is As-terminated. In the GaAs(111)A surface, each top layer Ga atom has a dangling bond. Removing one of these Ga atoms exposes three As-dangling bonds from the As-layer below, which is

energetically unstable. To ensure that it is energetically favourable, it reconstructs to a (2×2)GaAs(111)A surface with one in four of Ga atoms as surface vacancies (see Fig. 1.6). This vacancy formation allowed for the surface to transit from metallic-to-semiconducting. From figure 1.6, the removal of one out of the four surface Ga atoms leaves three dangling bonds in the surface layer. These can then give their electrons to the three As dangling bonds in the layer underneath made by the expulsion of the Ga atom. This results in a filled As dangling bonds and an empty Ga dangling bonds [38, 39, 40]. Reducing the number of dangling bonds, minimises the energy of the surface. The III-V semiconductors achieve this through the transfer of electrons from the dangling bonds of the Group III element to the dangling bonds of the Group V element. This electron transfer occurs because of the presence of sp^3 hybridised bonding orbitals in zinc blende structure.

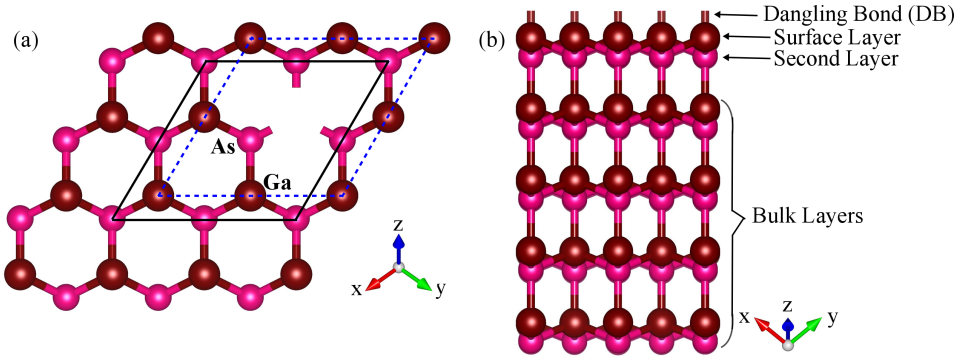

Figure 1.6: (a) Schematic showing the (2×2) GaAs(111)A-Ga vacancy surface reconstruction when viewed from the surface top. The dashed blue (solid black) lines marks the unit cell bounded by Ga (As) atoms. (b) Lateral view of the GaAs(111)A surface slab.

Based on the electron counting rule, the lowest energy surface structure is obtained when all the available electrons in the surface layer exactly fills the entire dangling bonds on the Group V element and empty dangling bonds from Group III element. Note that partially filled dangling bonds may result to a metallic behavior of the surface. In order to verify if the reconstructed (2×2) GaAs(111)A surface is ECR compliant, the number of electrons required by the reconstruction is compared with the total number of valence electrons available for bonding in the layers close to the surface. For III-V semiconductor

Table 1.2: Illustration of electron counting for the (2×2) GaAs(111)A reconstruction given in figure 1.6(a).

	Group III bonds	**Group V bonds**	**Group III DB**	**Group V DB**	**Total e^-**
Charge	$3/4e^-$	$5/4e^-$	$0e^-$	$2e^-$	
(2×2)	9	9	3	3	**24**
Total e^- from Ga					9
Total e^- from As					15
Total Valence					**24**

surfaces, each of Group III and Group V atoms averagely contributes $3/4e^-$ and $5/4e^-$ respectively, to make up the total charge of $2e^-$ needed to form a bond. And charges on Group III dangling bond transfer to Group V dangling bonds [38]. The total number of dangling bonds and existing dimers on the surface are added to the non-bulk sigma bonds from the second layer, which is the layer below the surface. Each of these bonds has $2e^-$ and together makes up the entire electrons required for the surface reconstruction. This is then matched with the total number of valence electrons available in the non-bulk bonding configurations (some valence electrons contributes to the bulk bonding). With the (2×2) reconstruction of the GaAs(111)A surface, given in figure 1.6, as a case study, there are 3 Ga atoms on the surface and 4 As atoms in the layer underneath, but one As atom contributes valence electrons in the bulk bonding on the third layer (see fig 1.6(a) and (b)). This leaves 3 As atoms available for non-bulk bonding near the surface. Each of the Ga atoms has a single dangling bond and three III-V sigma bonds and there is no dimer on this surface, but a Ga vacancy is present. Table 1.2 gives a summary of the computed values for this structure and it can be seen that the quantity of electrons required matches the quantity of accessible valence electrons thus the structure obeys the ECR. Semiconductors such as: Si, Ge, InP, InSb and others also reconstruct on their surfaces to form stable surface structures.

Zhang et al, proposed an extension of the ECR to account for metal-induced surface reconstruction of compound semiconductors [41]. These adjusted principles are known as the generalized electron counting rules (GECR) and they depend on three extra requirements. The first, is concerned with the preferred location of metal adatoms on the surface. It entails that d metal

adatoms (Mn, Cr or Fe) prefer to occupy interstitial sites near the III-V surfaces and *sp* (or *s*) metals like Ag, Al, as well as Au prefer to occupy the substitutional sites. The second GECR suggests that a metal adatom will serve as a donor or an acceptor depending on its Pauling electronegativity value relative to those of the constituent elements of the semiconductor. The third GECR states that surface reconstructions which minimize (maximize) the total number of valence electrons on the metal atoms (n_R) for metal donors (acceptors) are the lowest in energy. n_R can be given as:

$$n_R = v_M n_M + 3n_{III} + 5n_V - 2n_{bonds} \tag{1.3}$$

where v_M represent the number of valence electrons on a metal adatom and n_{bonds} is the total number of bonds (both sigma bonds and occupied DBs) formed around the surface. On the reconstructed surface n_M, n_{III} and n_V are respectively the number of metal, Group III and Group V atoms. The net charge transfer from the metal adatoms to the substrates is given by $v_M n_M - n_R$. Equation 1.3 reverts to the classic ECR for low-energy surface reconstructions, if there is no metal adatom (i.e $n_M = 0$ and $n_R \equiv 0$). Hence, with the adsorption of metal adatoms, the preferred structure is one that yields the lowest possible value of n_R.

1.5 Organization of the Thesis

In this thesis, we use density functional theory (DFT) to investigate the interface properties between the transition metal pnictide, MnSb and some III-V semiconductors. Also, the characteristics of half-metallic NiO and insulating MgO interfaces are investigated. This study aims to determine the structural, electronic and magnetic properties at the interfaces of these epitaxial growth models. Chapter 2 reviews the theoretical background and underlying principles for a DFT approach, and software packages used to successfully implement a simulation are briefly introduced. The half-metallicity of cubic (c)-MnSb and its interfaces with the high mobility semiconductor InSb is described in Chapter 3. Chapter 4 is devoted to the study of niccolite (n)-MnSb/InP and n-MnSb/GaAs interfaces, where the stability and polarization of these inter-

facial systems are compared. Chapter 5 discusses the interaction of n-MnSb with the semi-metal Sb. Chapter 6 focuses on NiO/MgO interfaces in different crystal directions. Finally, a summary and the key conclusions of this study together with some suggestions for future work are presented in Chapter 7.

Chapter 2

Theoretical Background

2.1 Density Functional Theory

DFT is an effective method of approximately solving the many body Schrödinger equation for electrons, which describes the properties of materials at the atomic, molecular and condensed scales [42, 43]. It is widely used by researchers across various disciplines because of its low computational cost compared to full quantum mechanical calculations [43, 44, 45]. The foremost notion of DFT is to make use of the density of the electron $n(\mathbf{r})$ as the argument to functionals, which determine the properties of a many body system [44, 46].

To study the various properties of a material I approach it based on the true, fundamental Hamiltonian of the many-electron system. This approach is called ab-initio or first principles [42]. A simple way to start is to write the time-independent, non-relativistic case, of the many-body Schrödinger equation for the material as:

$$H\Psi = E_\lambda \Psi_\lambda \tag{2.1}$$

where, H is the Hamiltonian operator, E_λ is an energy eigenvalue and Ψ_λ an eigenstate of the Hamiltonian. If the system were to be a particle in a box or a harmonic oscillator case which has a simple Hamiltonian, the Schrödinger equation can be solved exactly.But the physical system I have to deal with has many electrons interacting with many nuclei in a complex way [43]. So, the Schrodinger equation is:

$$\left[-\frac{\hbar^2}{2m}\sum_{i=1}^{N}\nabla_i^2+\sum_{i=1}^{N}V(\mathbf{r}_i)+\sum_{i=1}^{N}\sum_{j<i}U(\mathbf{r}_i\mathbf{r}_j)\right]\Psi_\lambda=E_\lambda\Psi_\lambda \tag{2.2}$$

where m is the mass of each electron, the terms in bracket are: the kinetic energy operator $\hat{T}$ of the individual electron, the potential energy $\hat{V}$ between each electron and the collection of atomic nuclei, and the electron-electron interaction energy $\hat{U}$ respectively. I can rewrite equation 2.2 based on $\hat{T}$, $\hat{V}$ and $\hat{U}$ for the ground state wave function and ground state energy.

$$\left[\hat{T}+\hat{V}+\hat{U}\right]|\Psi_o\rangle=E|\Psi_o\rangle \tag{2.3}$$

The wave function Ψ for this many-body problem of N electrons has $3N$ spatial coordinates $\mathbf{r}_i$, and N spin coordinates σ_i, hence, $\Psi=\Psi(\mathbf{r}_1\sigma_1,\ldots,\mathbf{r}_N\sigma_N)$. In equation 2.2 I have ignored the motion of the atomic nuclei (Born-Oppenheimer approximation) and choose to look at the ground state wave function Ψ_o with ground state energy E. Various methods have been developed to approximately solve the many-body Schrödinger equation given in equation 2.2. The Hartree-Fock (HF) approximation is the oldest and simplest one. There are others such as the free electron model (FEM) and Thomas-Fermi model [43, 42].

Now let us look at the DFT method of approximately solving the many-body system. Foundation is given by Hohenberg and Kohn (HK) theorems and the Kohn-Sham (KS) equations [46, 47]. Consider a non-magnetic system with a non-degenerate ground state described by the non-relativistic time-independent Schrödinger equation 2.2 or 2.3. The first HK theorem says: The ground-state energy E can be expressed as a unique functional of the electron density $E[n(\mathbf{r})]$. This means the information about the ground state properties is contained in the ground state electron density. The second HK theorem goes on to tell us about a feature of this functional: the true ground state electron density agreeing with the complete solution of the Schrödinger equation minimizes the total energy functional $E[n(\mathbf{r})]$. In order words, one should vary the likely densities and choose the one that gives the minimum energy [43, 44]. Let us rewrite equation 2.3 based on the total energy functional

(i.e. its expectation value) given by HK theorem [46],

$$E[n(\mathbf{r})] = \langle \Psi_o | [\hat{T} + \hat{V} + \hat{U}] | \Psi_o \rangle \tag{2.4}$$

$$E[n(\mathbf{r})] = T[n(\mathbf{r})] + U[n(\mathbf{r})] + \int d^3 r V_{ext}(\mathbf{r}) n(\mathbf{r}) \tag{2.5}$$

The kinetic energy of the electrons T and Coulomb potential from the electron-electron interaction U are independent of the external potential V_{ext}. I can further rewrite equation 2.5 as:

$$E[n(\mathbf{r})] = T_s[n(\mathbf{r})] + \frac{1}{2} \int d^3 r d^3 r' \frac{n(\mathbf{r}) n(\mathbf{r}')}{|\mathbf{r} - \mathbf{r}'|} + E_{xc}[n(\mathbf{r})] + \int d^3 r V_{ext}(\mathbf{r}) n(\mathbf{r}) \tag{2.6}$$

T_s is the kinetic energy of a putative non-interacting particle system with a ground state density n($\mathbf{r}$), and the second term is the classical Coulomb interaction. $E_{xc}[n(\mathbf{r})]$ is the exchange and correlation energy functional which has all remaining many-particle effects in it: the many-particle input to the kinetic energy and Pauli exclusion principle effects [44]. At this stage it is still impossible to solve the many-body Schrödinger equation because the functionals $T_s[n(\mathbf{r})]$ and $E_{xc}[n(\mathbf{r})]$ are unknown, though numerous fairly accurate functionals have been suggested for the later.

To find the minimum energy solutions of the total energy functional, Kohn and Sham (KS) came up with a scheme that transforms the many-particle problem to a single-particle one and gives a set of equations similar to Schrödinger's [44, 47]. It is called the Kohn-Sham (KS) equation and is given as:

$$\left[-\frac{1}{2} \nabla^2 + V_{ext} + \int d^3 r' \frac{n(\mathbf{r})}{|\mathbf{r} - \mathbf{r}'|} + \frac{\delta E_{xc}[n(\mathbf{r})]}{\delta n(\mathbf{r})} \right] \psi_i(\mathbf{r}) = \epsilon_i \psi_i(\mathbf{r}) \tag{2.7}$$

where, from the left-hand side, the second term is the external potential V_{ext} due to the interaction between an electron and the collection of atomic nuclei. The third term is the Hartree potential V_H which is the Coulomb repulsion between the electron under consideration and the total electron density. The next term is the functional derivative of E_{xc} with respect to $n(\mathbf{r})$. This is the potential V_{xc} of the single-particle equations due to the exchange-correlation

energy E_{xc}. Solving equation 2.7 self-consistently we obtain the electron density at ground state:

$$n(\mathbf{r}) = \sum_{i=1}^{N} |\psi_i(\mathbf{r})|^2 \tag{2.8}$$

Knowing the solution $\{\epsilon_i, \psi_i(\mathbf{r})\}$ to equation 2.7, I can now write the unknown functional $T_s[n(\mathbf{r})]$ as

$$T_s[n(\mathbf{r})] = \sum_{i=1}^{N} \epsilon_i - \int d^3r \left\{V_{ext}(\mathbf{r}) + V_H(\mathbf{r}) + V_{xc}(\mathbf{r})\right\} n(\mathbf{r}) \tag{2.9}$$

The KS equations are solved in an iterative way until a self-consistent solution is obtained. The Kohn-Sham approach has proven to be reliable for calculating ground state properties for many-body systems with a precision that matches experimental data [44, 45]. Now I can write the total energy expression as

$$E[n(\mathbf{r})] = \sum_{i=1}^{N} \epsilon_i - \frac{1}{2} \int d^3r d^3r' \frac{n(\mathbf{r})n(\mathbf{r}')}{|\mathbf{r} - \mathbf{r}'|} - \int d^3r V_{xc}[n(\mathbf{r})]n(\mathbf{r}) + E_{xc}[n(\mathbf{r})] \tag{2.10}$$

There is still one more complication which is that the true exchange correlation functional is not known. This term is approximated in some way to get an approximate energy and this makes the variational principle somewhat suspect. However, variational principle is still used and the density obtained is taken as the ground state density. The variational principle says: the computed energy from any trial wave functions will be higher than the true ground state energy, but equals it if the trial wave function is identical to the true ground state wave function. Several approximations for $E_{xc}[n(\mathbf{r})]$ are in use today and the popular ones are: local density approximation (LDA), generalized gradient approximation (GGA) and hybrid functionals. LDA uses only the local electron density to replace the exact exchange-correlation functional by

$$E_{xc}^{LDA}[n(\mathbf{r})] = \int d^3r n(\mathbf{r}) \epsilon_{xc}(n(\mathbf{r})) \tag{2.11}$$

where $\epsilon_{xc}(n(\mathbf{r}))$ is the exchange and correlation energy per particle of a homogeneous electron gas with density $n(\mathbf{r})$. Though it works very well but it often overestimates bonding, which leads to slightly small lattice parameters

(about 0.5 Å less) and slightly large bulk moduli (say 5 more) from the actual values for a given material [44]. It can give incorrect order of phase stability and errors in the energetics of magnetic materials, hence GGA is often used in this work [48]. Note that the HK and KS treatment above can also be applied to magnetic systems, in which case the spin component (e.g, $n = n_\uparrow n_\downarrow$) is included. Rewriting equation 2.11 to represent the local spin density (LSD) approximation for an electron gas of uniform spin densities $n_\uparrow(\mathbf{r}), n_\downarrow(\mathbf{r})$ gives:

$$E_{xc}^{LDA}[n_\uparrow(\mathbf{r}), n_\downarrow(\mathbf{r})] = \int d^3r n(\mathbf{r}) \epsilon_{xc}(n_\uparrow(\mathbf{r}), n_\downarrow(\mathbf{r})) \tag{2.12}$$

GGA uses the electron density and its gradient which gives rise to a huge number of different GGA functionals, because it needs a mix of $n(\mathbf{r})$ and $\nabla n(\mathbf{r})$ to be decided ad hoc. The two most common are Perdew-Wang functional (PW91) and Perdew-Burke-Ernzerhof functional (PBE), which in section 2.2 I have provided further details on. Although GGA is better than LDA in some ways, it still does not deal with the issues of strongly correlated systems, for instance transition metal oxide and heavy fermion systems. To correct this, schemes such as LDA+U or GGA+U are used, which have an orbital-dependent interaction term called the Hubbard U parameter [43, 44]. Hybrid functionals are made from an orbital-dependent Hartree-Fock part and an explicit density functional. They are usually preferred by quantum chemists over LDA and GGA for atomic and molecular calculations [44].

2.2 Generalized Gradient Approximation

The generalized gradient approximation (GGA) is an extension of LDA where information about the electron density $n(\mathbf{r})$ as well as its gradient $\nabla n(\mathbf{r})$ is used to provide an account of the non-homogeneity of the true electron density. These functionals are at the centre stage of modern DFT and can be expressed generally as:

$$E_{xc}^{GGA}[n_\uparrow, n_\downarrow] = \int d^3r f(n_\uparrow, n_\downarrow, \nabla n_\uparrow, \nabla n_\downarrow) \tag{2.13}$$

where $f(n_\uparrow, n_\downarrow, \nabla n_\uparrow, \nabla n_\downarrow)$ is some parametrized analytic function, that has no analytically defined form. Several suggestions for $f(n_\uparrow, n_\downarrow, \nabla n_\uparrow, \nabla n_\downarrow)$ exist,

but a rational choice can be made by considering the derivations and prescribed properties of a given GGA fuctional and its suitability for the material system under study. GGA typically provides a more accurate description of atoms, molecules and solids than the local spin density (LSD) approximation. It typically minimizes the error due to bond dissociation energy as well as improves the total energies, atomization energies, transition-state energy barriers and structural energy differences [49, 50, 51, 52]. $E_{xc}^{GGA}[n_\uparrow, n_\downarrow]$ is usually separated into its exchange and correlation terms, i.e.

$$E_{xc}^{GGA} = E_x^{GGA} + E_c^{GGA} \tag{2.14}$$

A prominent representation to simplify this GGA was first given by Perdew and Wang in 1986 [53]. In order for this functional to be used routinely in self-consistent calculations for atoms, molecules and solids, the exchange energy as a functional of the density was approximated as:

$$E_x^{GGA}[n] = A_x \int d^3r n^{4/3} F_x(s) \tag{2.15}$$

where,

$$A_x = -\frac{3}{4}(3/\pi)^{1/3} \tag{2.16}$$

$$s = \nabla n/(2k_F n) \tag{2.17}$$

$$k_F = (3\pi^2 n)^{1/3} \tag{2.18}$$

and

$$F_x(s) = (1 + 1.296s^2 + 14s^4 + 0.2s^6)^{1/15} \tag{2.19}$$

The function $F_x(s)$ is an analytical fit. The functional form of equation 2.15 scales properly as an exchange energy [54]:

$$E_x[n_\gamma] = \gamma E_n[n] \tag{2.20}$$

where $n_\gamma(\mathbf{r}) = \gamma^3 n(\gamma \mathbf{r})$ represent the scaled density. A corresponding spin-scaling exchange energy for a spin density functional can be constructed as:

$$E_x[n_\uparrow, n_\downarrow] = \frac{1}{2}E_x[2n_\uparrow] + \frac{1}{2}E_x[2n_\downarrow] \tag{2.21}$$

The functional derivative of exchange energy $E_x^{GGA}[n]$ is the exchange potential needed for a self-consistent calculation

$$\frac{\delta E_x}{\delta n(\mathbf{r})} = A_x n^{1/3} \left[\frac{4}{3} F - t s^{-1} \frac{dF}{ds} - \left(u - \frac{4}{3} s^3 \right) \frac{d}{ds} \left\{ s^{-1} \frac{dF}{ds} \right\} \right] \tag{2.22}$$

where,

$$t = (2k_F)^{-2} n^{-1} \nabla^2 n \tag{2.23}$$

and

$$u = (2k_F)^{-3} n^{-2} \times \nabla n \cdot \nabla \left| \nabla n \right| \tag{2.24}$$

As $|\mathbf{r}| \to \infty$, the functional derivative for this GGA tends to zero. For a spin-density functional, one constructs the exchange potential from:

$$\frac{\delta E_x[n_\uparrow, n_\downarrow]}{\delta n_\sigma(\mathbf{r})} = \frac{\delta E_x[n]}{\delta n(\mathbf{r})}\Big|_{n(\mathbf{r})=2n_\sigma(\mathbf{r})} \tag{2.25}$$

This real-space cutoff construction of GGA functional was later extended from exchange to correlation, which led to Perdew-Wang 1991 (PW91) GGA for E_{xc} [55, 56]. Then in 1996, Perdew, Burke and Ernzerhof (PBE) came up with a much simpler way of constructing PW91 functional with some improvements [57]. Practically, PBE is equivalent to PW91 and they produce essentially the same results, however PBE describes the linear response of uniform electron gas more accurately. PBE achieves this accuracy by allowing the electron gas to behave correctly under uniform scaling and have a smoother potential.

To construct the PBE functional, it is normal and important to impose the real-space cutoff condition used for the construction of PW91 [53, 58]. The PBE derivation will be summarized here, an interested reader can look at the references [57, 56] for a detailed discussion. A GGA(PBE) construction for correlation energy begins in the form

$$E_c^{GGA}[n_\uparrow, n_\downarrow] = \int d^3 r n [\epsilon_c(r_s, \zeta) + H(r_s, \zeta, t)] \tag{2.26}$$

where r_s is the Seitz radius, which refers to the radius of a sphere that typically

has one electron and is defined in the equation below:

$$n = \frac{3}{4\pi r_s^3} = \frac{k_F^3}{3\pi^2} \tag{2.27}$$

The relative spin polarization ζ is given as:

$$\zeta = \frac{n_\uparrow - n_\downarrow}{n} \tag{2.28}$$

and t is the reduced density gradient, which is a dimensionless quantity.

$$t = \frac{|\nabla n|}{2\phi k_s n} = \left(\frac{\pi}{4}\right)^{1/2} \left(\frac{9\pi}{4}\right)^{1/6} \frac{s}{\phi r_s^{1/2}} \tag{2.29}$$

Here ϕ is a spin-scaling factor [59],

$$\phi(\zeta) = \frac{[(1+\zeta)^{2/3} + (1-\zeta)^{2/3}]}{2} \tag{2.30}$$

and

$$k_s = \sqrt{\frac{4k_F}{\pi a_0}} \tag{2.31}$$

is Thomas-Fermi screening wave number ($a_0 = \hbar^2/(me^2)$). The density parameters r_s and ζ are local, while the density n is equivalent to $n_\uparrow + n_\downarrow$ in cases that involves spin-densities. $H(r_s, \zeta, t)$ is the density gradient contribution. Under uniform density scaling of $n_\gamma(r) = \gamma^3 n(\gamma \mathbf{r})$ to the high-density limit ($\gamma \to \infty$), $E_c^{GGA}[n_\uparrow, n_\downarrow]$ from equation 2.26 tends to a negative constant:

$$E_c^{GGA}[n_\gamma] \to -\frac{e^2}{a_0} \int d^3r n\gamma\phi^3 \ln\left[1 + \frac{1}{\chi s^2/\phi^2 + (\chi s^2/\phi^2)^2}\right] \tag{2.32}$$

where the dimensionless density gradient s is defined by equation 2.17 and $\chi = (\beta/\gamma)c^2 \exp(-\omega/\gamma) \cong 0.72161 (\beta \cong 0.066725, \gamma \cong 0.031091, c \cong 1.2277$ and $\omega \cong 0.046644)$. For a two-electron ion of nuclear charge $Z \to \infty$, the correlation energy is exactly -0.0467.

To construct the PBE GGA for the exchange energy, apply the spin-scaling relation of equation 2.21 to 2.15, which brings it to the form of equation

2.33 for $\zeta = 0$ everywhere. The uniform gas exchange energy $\epsilon_x = -3e^2 k_F/4\pi$.

$$E_x^{GGA} = \int d^3r n \epsilon_x(n) F_x(s) \tag{2.33}$$

In order to recover the useful LSD description of the linear response of the uniform gas, the gradient coefficient for exchange must cancel that for correlation (as $s \to 0$). This leads to,

$$F_x(s) \to 1 + \mu s^2 \tag{2.34}$$

where $\mu = \beta(\pi^2/3) \cong 0.21951$. Also, we want the Lieb-Oxford bound

$$E_x[n_\uparrow, n_\downarrow] \geq E_{xc}[n_\uparrow, n_\downarrow] \geq -1.679 e^2 \int d^3r n^{4/3} \tag{2.35}$$

to be satisfied [56]. This can be achieved with the simple form

$$F_x(s) = 1 + k - \frac{k}{(1 + \mu s^2/k)} \tag{2.36}$$

which satisfies equation 2.34 as well. Here k is a constant less than or equal to 0.804.

A good way to portray the nonlocality of the PBE GGA exchange and correlation, is to write

$$E_{xc}^{GGA}[n_\uparrow, n_\downarrow] = \int d^3r n \epsilon_x(n) F_{xc}(r_s, \zeta, s) \tag{2.37}$$

by defining an enhancement factor $F_{xc}(r_s, \zeta, s)$ over spin-unpolarized ($\zeta = 0$) local exchange [49]. The effects of correlation (r_s-dependence), spin polarization (ζ), and nonlocality (s-dependence) can be shown by the enhancement factor. Figure 2.1(a) displays the s-dependence of the enhancement factor for a spin-unpolarized ($\zeta = 0$) system. While, Figure 2.1(b) shows the enhancement factor for the difference between the fully spin-polarized ($\zeta = 1$) and unpolarized ($\zeta = 0$) $F_{xc}(r_s, \zeta, s)$ [56]. The high-density-limit ($r_s \to 0$) is dominated by the exchange-only enhancement factor. By definition $F_x(\zeta = 0, s = 0) = 1$ as $r_s \to 0$, see figure 2.1(a). At fixed r_s (decrease r_s), as the reduced gradient s increases, exchange is strongly turned on, whereas correlation is turned off. On the other hand, correlation is very strong in comparison with exchange

in the low-density-limit ($r_s \to \infty$), as a result nonlocality is dominated by correlation. Note that for a fully spin-polarized system ($r_s \to \infty, \zeta = 1$), nonlocality is approximately cancelled in the low-density-limit and the exchange-correlation hole becomes local. In the range $0 \leq s \leq 1$, the exchange and correlation nonlocalities are opposite, and tend to cancel for valence-electron densities ($1 \leq r_s \leq 10$).

2.3 Hubbard U and DFT+U

The local density approximation (LDA) and generalized gradient approximation (GGA) have been successful in describing a nearly uniform electron density, but they fail in the non-uniform bound of localized electronic states with strongly correlated electrons. In other words, on-site Hubbard-like (Coulomb) interactions are not correctly treated in the LDA/GGA formalism, while screening correlation effects can be well described by these functionals [60, 44]. DFT+U is based on a correction to the standard functional, by providing an improved description of the electronic states of strongly correlated systems (typically, localized d or f orbitals). This is done by adding an on-site Hubbard-like (U) interaction to the approximate DFT total energy of a system [60, 61, 62]:

$$E_{LDA+U}[n(\mathbf{r})] = E_{LDA+U}[n(\mathbf{r})] + E_{Hub}[\{n_m^{I\sigma}\}] - E_{DC}[\{n^{I\sigma}\}] \tag{2.38}$$

where E_{LDA} is the total energy functional being corrected, E_{Hub} encompasses the Hubbard Hamiltonian for correlated states, and E_{DC} is the double-counting (DC) term. The DC functional is not uniquely defined and different forms have been used. However, in the unitary-transformation-invariant formulation of LDA+U, more general expressions of E_{Hub} and E_{DC} were given:

$$\begin{aligned} E_{Hub}[\{n_{mm'}^{I}\}] = \frac{1}{2} \sum_{\{m\},\sigma,I} & \langle m, m'' \left| V_{ee} \right| m', m''' \rangle \, n_{mm'}^{I\sigma} n_{m''m'''}^{I-\sigma} \\ & + (\langle m, m''' \left| V_{ee} \right| m', m''' \rangle - \langle m, m'' \left| V_{ee} \right| m''', m' \rangle) \times n_{mm'}^{I\sigma} n_{m''m'''}^{I\sigma} \end{aligned} \tag{2.39}$$

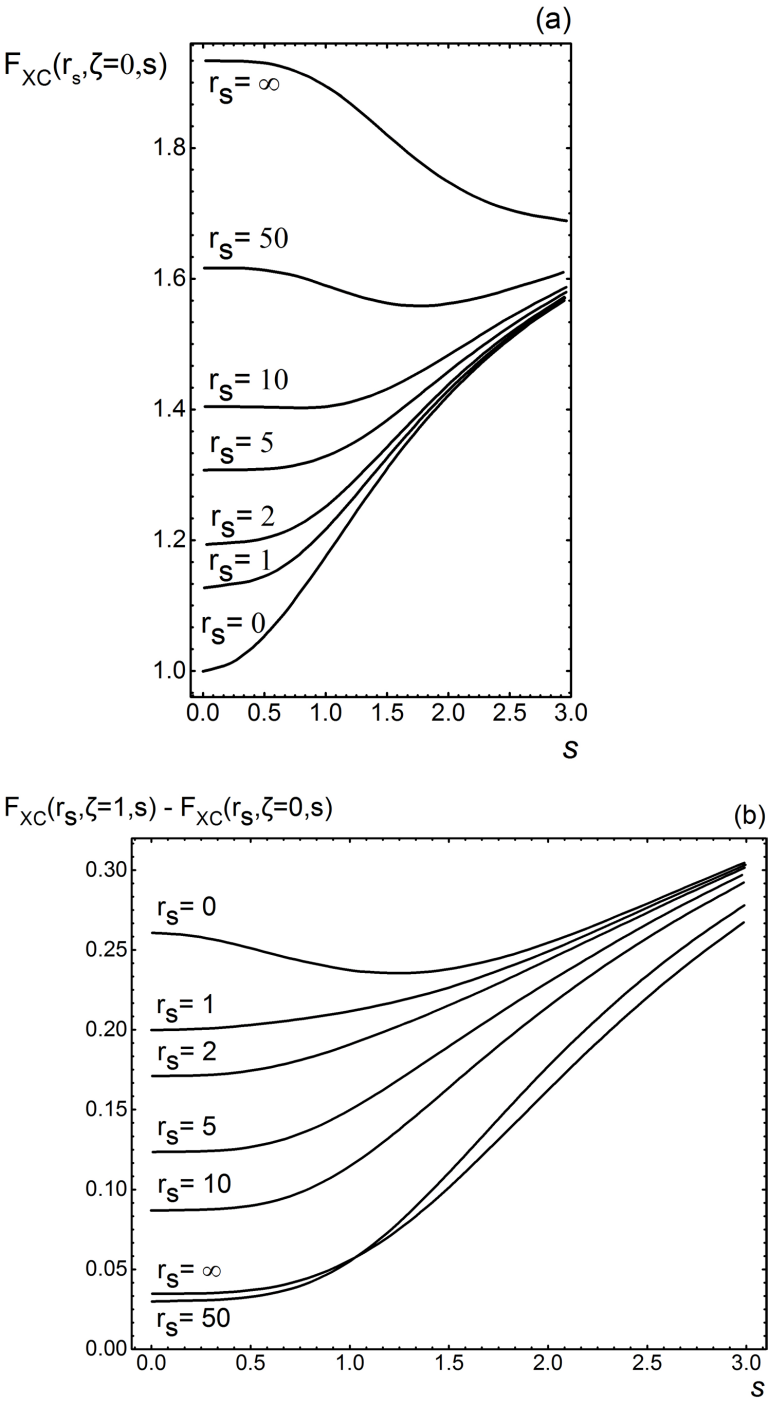

Figure 2.1: The enhancement factor F_{xc} of equation 2.37 for the Perdew, Burke and Ernzerhof GGA, as a function of the reduced density gradient s of equation 2.17. (a) For $\zeta = 0$, and (b) for the difference between $\zeta = 1$ and $\zeta = 0$. Plot was taken from reference [56].

$$E_{DC}\left[\left\{n^I_{mm'}\right\}\right] = \sum_I \left\{ \frac{U^I}{2} n^I(n^I - 1) - \frac{J^I}{2}\left[n^{I\uparrow}(n^{I\uparrow} - 1) + n^{I\downarrow}(n^{I\downarrow} - 1)\right] \right\} \tag{2.40}$$

Here $n^{I\sigma}_m$ are the occupation numbers of localized orbitals, I is the atomic site index, m is state index and σ is the spin. $n^{I\sigma}_{mm'}$ is given as:

$$n^{I\sigma}_{mm'} = \sum_{k,v} f^\sigma_{kv} \left\langle \psi^\sigma_{kv} | \phi^I_{m'} \right\rangle \left\langle \phi^I_m | \psi^\sigma_{kv} \right\rangle \tag{2.41}$$

where the coefficient f^σ_{kv} denote the occupations of KS states. The first term on the right hand side of equation 2.39 inside the bra-ket notation can be written as:

$$\langle m, m'' | V_{ee} | m', m''' \rangle = \sum_{k=0}^{2l} a_k(m, m', m'', m''') F^k \tag{2.42}$$

Here l is the angular moment of the localized (d or f) electrons and a_k the angular factors is given below

$$a_k(m, m', m'', m''') = \frac{4\pi}{2k+1} \sum_{q=-k}^{k} \langle lm | Y_{kq} | lm' \rangle \left\langle lm'' | Y^*_{kq} | lm''' \right\rangle \tag{2.43}$$

The parameters F^k (F^0, F^2, and F^4 for d electrons, while f states require F^6 to compute the matrix elements V_{ee}) are the radial Slater integrals. The screened on-site Coulomb (U) and exchange (J) interaction can be expressed as:

$$U = \frac{1}{(2l+1)^2} \sum_{m,m'} \langle m, m' | V_{ee} | m, m' \rangle = F^0 \tag{2.44}$$

$$J = \frac{1}{2l(2l+1)} \sum_{m \neq m', m'} \langle m, m' | V_{ee} | m', m \rangle = \frac{F^2 + F^4}{14} \tag{2.45}$$

Once U and J have been calculated, the F^k parameters (as well as V_{ee}) are extracted using the above equations by presuming atomic values for F^2/F^4 and F^6/F^4 ratios (e.g., $F^2/F^4 = 0.625$).

A simplified expression of E_{Hub} and E_{DC} for the rotationally invariant scheme which stems from equations 2.39 and 2.40 by keeping just the lowest

order integrals F^0 and setting $F^2 = F^4 = J = 0$ is as follows:

$$\begin{aligned} E_U\left[\left\{n^{I\sigma}_{mm'}\right\}\right] &= E_{Hub}\left[\left\{n^{I}_{mm'}\right\}\right] - E_{DC}\left[\left\{n^{I}\right\}\right] \\ &= \sum_I \frac{U^I}{2}\left[(n^I)^2 - \sum_\sigma Tr\left[(n^{I\sigma})^2\right]\right] - \sum_I \frac{U'}{2} n^I(n^I - 1) \\ &= \frac{U}{2}\sum_{I\sigma} Tr[\mathbf{n}^{I\sigma}(1 - \mathbf{n}^{I\sigma})] \end{aligned} \quad (2.46)$$

Diagonalizing the occupation matrices based on the localized orbitals representation

$$\mathbf{n}^{I\sigma}\mathbf{v}^{I\sigma}_i = \lambda^{I\sigma}_i \mathbf{v}^{I\sigma}_i \quad (2.47)$$

with the constraints $0 \leq \lambda^{I\sigma}_i \leq 1$, where $\lambda^{I\sigma}_i$ and $\mathbf{v}^{I\sigma}_i$ are respectively eigenvalues and eigenvectors. The Hubbard correction for the energy becomes:

$$E_U\left[\left\{n^{I\sigma}_{mm'}\right\}\right] = \frac{U}{2}\sum_{I\sigma}\sum_i \lambda^{I\sigma}_i(1 - \lambda^{I\sigma}_i) \quad (2.48)$$

with this, the corrective functional can be derived from just one interaction parameter (U). It is normal to express the Coulomb interaction U in terms of an effective value that includes the Hunds rule coupling $J : U_{eff} = U - J$. It provides a more accurate account of on-site electron-electron interaction, capturing the localization of electrons. The Hubbard correction occasionally gives close to experimental band gap value in the band structure for some materials (e.g. NiO and MnO) due to crystal field splittings or Hunds rule [63, 64]. The U should not be used as an adjustable parameter to mimic experimental band gaps.

2.4 Plane waves and Pseudopotentials

There are various computational methods employed to solve the Kohn-Sham (KS) equations of 2.7, like Hartree-Fock (HF), Korringa-Kohn-Rostoker (KKR), plane-waves, and others [65]. From KS theory, a general expression of the total

energy for the finished calculation is written as

$$E = -\sum_{i}^{occ} \int d^3r \varphi_i^*(\mathbf{r}) \frac{\nabla^2}{2} \varphi_i(\mathbf{r}) + \int d^3r v_{ext}(\mathbf{r}) n(\mathbf{r}) + \frac{1}{2} \int d^3r \int d^3r' \frac{n(\mathbf{r}) n(\mathbf{r}')}{|\mathbf{r} - \mathbf{r}'|} + E_{xc} \quad (2.49)$$

where on the right on side, the first term is the non-interacting kinetic energy, the second term is the external potential, next is the Hartree term and finally, the exchange-correlation energies. To make equation 2.49 suitable for implementation in most DFT codes, it can be simplified further to yield:

$$E = \sum_{i}^{occ} \varepsilon_i - \int d^3r \left[\frac{1}{2} v_H(\mathbf{r}) + v_{xc}(\mathbf{r}) \right] n(\mathbf{r}) + E_{xc} \quad (2.50)$$

and the electronic density is defined as:

$$n(\mathbf{r}) = \sum_{i}^{occ} |\varphi_i(\mathbf{r})|^2 \quad (2.51)$$

In order to account for interactions between ions (E_{nn}), a repulsive Coulomb term should be added to the total energy in a geometry optimization calculation

$$E_{nn} = \sum_{\alpha,\beta} \frac{Z_\alpha Z_\beta}{|\mathbf{R}_\alpha - \mathbf{R}_\beta|} \quad (2.52)$$

2.4.1 Plane-waves basis sets

To expand the Kohn-Sham electronic wave functions, a plane-wave basis set is essential, since it makes better use of the periodicity of crystals. The number of plane-waves basis set required is very large and it can be truncated to a finite number of plane-wave functions, below a particular cutoff energy [56, 66].

Based on Blochs theorem for a periodic solid, the electronic wave-functions can be written as

$$\varphi_{\mathbf{k},n}(\mathbf{r}) = e^{i\mathbf{k}\cdot r} \sum_{\mathbf{G}} c_{\mathbf{k},n}(\mathbf{G}) e^{i\mathbf{G}\cdot r} \quad (2.53)$$

where $\mathbf{k}$ is the wave vector, the band index is n, and the reciprocal lattice vectors are represented by $\mathbf{G}$. The plane-wave representation of Kohn-Sham equations assume the following form

$$\sum_{\mathbf{G}'} \left[\frac{1}{2}|\mathbf{k}+\mathbf{G}|^2 \delta_{\mathbf{G},\mathbf{G}'} + v_{ion}(\mathbf{G}-\mathbf{G}') + v_H(\mathbf{G}-\mathbf{G}') + v_{xc}(\mathbf{G}-\mathbf{G}') \right] c_{\mathbf{k},n}(\mathbf{G}') = \varepsilon_{\mathbf{k},n} c_{\mathbf{k},n}(\mathbf{G}) \quad (2.54)$$

where the various potentials have been given in terms of their Fourier transforms. Equation 2.54 can be solved by diagonalizing the Hamiltonian matrix, represented by the terms in the brackets. To limit the size of the matrix (or $\mathbf{G}$) an energy cutoff is set up

$$\frac{|\mathbf{k}+\mathbf{G}|^2}{2} \leq E_{cut} \quad (2.55)$$

But a very large $\mathbf{G}$ (many plane waves) is needed to describe accurately the wave functions of material systems, which is a severe problem. This is because the core electrons are tightly bound to the nuclei in solids or molecules and the wave functions of the valence electrons change rapidly in the core region. With the application of the pseudopotential approximation, this challenge can be overcome.

2.4.2 Pseudopotentials

A vital component of many DFT calculations is the pseudopotentials, which uses the fact that most physical properties of solids are mainly due to the valence electrons. The pseudopotential method treats core electrons as frozen entities and approximates the potential felt by the valence electrons to a weaker pseudopotential that can reproduce smooth wave functions (pseudo wave functions) of the valence electrons instead of the true valence wave functions. Figure 2.2 shows an ionic potential, valence wave function then an equivalent pseudopotential and pseudo wave function. The wave function of a valence electron undergoes rapid oscillation in the core electron region owing to the strong ionic potential in this region. As a result of these oscillations the valence electron wave function remains orthogonal to core electron wave func-

tions. The pseudopotential is constructed in such a way that the pseudo wave functions do not have radial nodes in the core region. Outside the core region (beyond the distance $r_c = 1.3$ au), the all electron and pseudoelectron potentials are similar (see fig. 2.2) as well as their wave functions [66]. Generally, pseudopotentials are mostly expressed as:

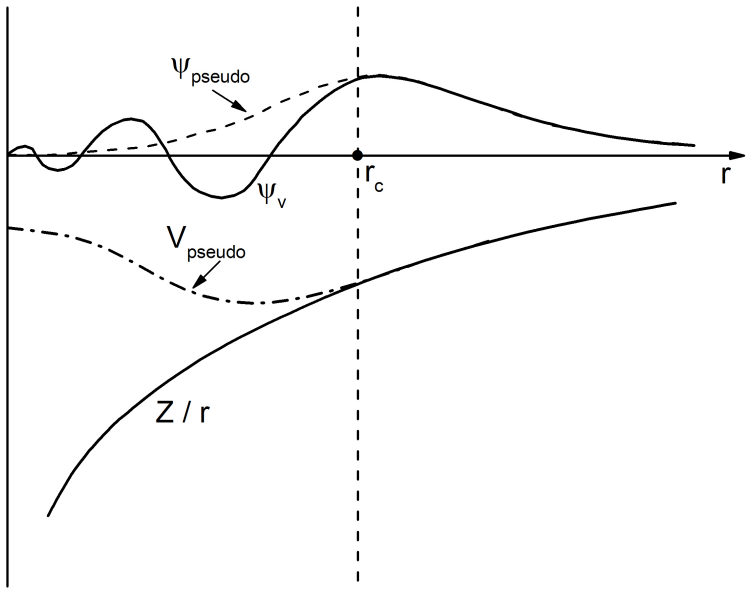

Figure 2.2: Comparison of all electron (solid lines) and pseudoelectron (dashed lines) potentials and the wave functions (ψ) they represents. r_c depicts the radius at which all electron and pseudoelectron values meet. The figure is a remake of figure 5 in Ref. [66].

$$V_{NL} = \sum_{lm} |lm\rangle V_l \langle lm| \tag{2.56}$$

where $|lm\rangle$ are the spherical harmonics and V_l is the pseudopotential for angular momentum l. A pseudopotential is said to be local, when it uses the same potential for all angular momentum components. Local pseudopotentials have a very high computational efficiency compare to nonlocal ones, but just a handful of elements can be described correctly with local pseudopotentials.

In pseudopotential applications, the amount of hardness of a pseudopotential is important. When a pseudopotential requires a small (large) number of Fourier components for its accurate representation, it is a soft (hard) pseu-

dopotential. Norm-conserving pseudopotentials for transition metals and first row elements in the early days of the method were extremely hard due to their high cutoff energy, hence there was the need to find a way to improve convergence properties of this potentials [1].

An approach which involves relaxing the norm-conservation condition in order to generate much softer pseudopotentials was suggested by Vanderbilt [67]. This is the ultrasoft pseudopotential scheme, where calculations with the lowest possible cutoff energy for the plane-wave basis set is allowed. Ultrasoft pseudopotentials have much better energy transferability and accuracy, and it usually treats shallow core states as well a valence states. In the Vanderbilt ultrasoft pseudopotential (usp) scheme, which reduces the number of plane waves and energy cutoff required to describe electronic wave functions [67, 68], the total energy of the valence electrons N_v, described by the wave functions ϕ_i, is given by

$$E_{tot}\left[\{\phi_i\},\{\mathbf{R_I}\}\right] = \sum_i \left\langle \phi_i \right| -\nabla^2 + V_{NL} \left|\phi_i\right\rangle + \frac{1}{2}\int\int d\mathbf{r}d\mathbf{r}' \frac{n(\mathbf{r}), n(\mathbf{r}')}{|\mathbf{r}-\mathbf{r}'|} + E_{xc}[n] + \int d\mathbf{r} V_{loc}^{ion}(\mathbf{r}) n(\mathbf{r}) + U\left(\{\mathbf{R_I}\}\right) \quad (2.57)$$

where $U(\mathbf{R_I})$ is the ion-ion interaction energy, $V_{loc}^{ion}(\mathbf{r}) = \sum_I V_{loc}^{ion}(|\mathbf{r}-\mathbf{R_I}|)$ is the local pseudopotential and the nonlocal pseudopotential is given by

$$V_{NL} = \sum_{nm,I} D_{nm}^{(0)} |\beta_n^I\rangle\langle\beta_m^I| \quad (2.58)$$

where the functions β_n^I and coefficients $D_{nm}^{(0)}$ characterize the pseudopotential and differ for different atomic species. The indices n and m run over the total number of angular momentum eigenfunctions β_n, and I represents an atomic site. The electron density is given by

$$n(\mathbf{r}) = \sum_i \left[|\phi_i(\mathbf{r})|^2 + \sum_{nm,I} Q_{nm}^I(\mathbf{r}) \langle\phi_i|\beta_n^I\rangle\langle\beta_m^I|\phi_i\rangle \right] \quad (2.59)$$

[1] `http://www.tcm.phy.cam.ac.uk/castep/documentation/WebHelp/content/pdfs/castep.htm`

where the augmentation functions $Q^I_{nm}(\mathbf{r})$ are strictly localized in the core regions. In equation (2.59) the electron density has been separated into a soft delocalized contribution given by the squared moduli of the wave functions, and a hard localized part at the cores. The ultrasoft pseudopotential is completely determined by $V^{ion}_{loc}(\mathbf{r})$, $D^{(0)}_{nm}$, $Q^I_{nm}(\mathbf{r})$, and $\beta_n(\mathbf{r})$.

The relaxation of the norm-conserving restraint is achieved by introducing a generalized orthonomality condition

$$\langle\phi_i|S(\mathbf{R}_I)|\phi_j\rangle = \delta_{ij} \tag{2.60}$$

Here the Hermitian overlap operator S is given by

$$S = 1 + \sum_{nm,I} q_{nm}|\beta^I_n\rangle\langle\beta^I_m| \tag{2.61}$$

and q_{nm} is equivalent to the integral of $Q_{nm}(\mathbf{r})$. S is dependent on the ionic positions through the term $|\beta^I_n\rangle$, $\beta^I_n(\mathbf{r}) = \beta_n(\mathbf{r} - \mathbf{R}_I)$. Based on the ultrasoft pseudopotential scheme the Kohn-Sham equations can be expressed as:

$$H|\phi_i\rangle = \varepsilon_i S|\phi_i\rangle \tag{2.62}$$

where ε_i represents Lagrange multipliers, and

$$H = -\nabla^2 + V_{eff} + \sum_{nm,I} D^I_{nm}|\beta^I_n\rangle\langle\beta^I_m| \tag{2.63}$$

The screened effective potential V_{eff}, is given as

$$V_{eff}(\mathbf{r}) = V^{ion}_{loc}(\mathbf{r}) + \int d\mathbf{r}' \frac{n(\mathbf{r}')}{|\mathbf{r} - \mathbf{r}'|} + \mu_{xc}(\mathbf{r}) \tag{2.64}$$

where $\mu_{xc}(\mathbf{r}) = \delta E_{xc}[n]/\delta n(\mathbf{r})$. All the terms arising from the augmented portion of the electron density are grouped with the nonlocal part of the pseudopotential (eq. 2.58) by defining new coefficients

$$D^I_{nm} = D^{(0)}_{nm} + \int d\mathbf{r} V_{eff}(\mathbf{r}) Q^I_{nm}(\mathbf{r}) \tag{2.65}$$

Here D^I_{nm} differs from the parameters $D^{(0)}_{nm}$, in the sense that D^I_{nm} rely on the wavefunctions through V_{eff} (eq. 2.64) and its values are updated in the self-consistent calculation.

The difference between Vanderbilts ultrasoft pseudopotential and the norm-conserving type resides in the presence of the S operator, the wavefunction dependence of the D^I_{nm} and the fact that the number of β^I_n functions is twice as large, for the ultrasoft potential. A number of calculations associated with augmentation functions $Q^I_{nm}(\mathbf{r})$ can be carried out in real space due to the localized nature of the function involved, so that the extra steps generally do not have a large effect on the efficiency. The usp scheme has been implemented in the DFT code used for this work, hence I will leave out the technical details on its algorithm generation and implementation, which can be found in reference [68].

2.5 Broyden-Fletcher-Goldfarb-Shanno Scheme

To concurrently relax the internal coordinates and lattice parameters of a crystal under pressure without destroying the crystal structure symmetry in the process, a quasi-Newton method can be used. The Broyden-Fletcher-Goldfarb-Shanno (BFGS) scheme [69] is the most successful class of quasi-Newton method [70, 71]. BFGS is an iterative optimization algorithm that uses forces and stress to relax crystal structures efficiently. It accumulates information about the shape of the enthalpy surface in the inverse Hessian matrix H. From H, elastic stiffness coefficients, bulk modulus and optical phonon frequencies at the Brillouin zone center can be estimated.

Consider a crystal structure with N atoms in the unit cell under applied pressure p. Its enthalpy $\mathcal{H} = E + p\Omega$ has to be minimized in a $(9 + 3N)$-dimensional space:

$$\mathcal{H} = \mathcal{H}(\varepsilon, s_1, \ldots, s_N) \tag{2.66}$$

Let column vector X represent a point in configuration space, which has nine-element column vector $X_{3(i-1)+j} = \varepsilon_{ij}; i, j = 1, 2, 3$. These nine components are the strain components ε. Then the $s_1, s_2, \ldots, s_N$ terms are the atomic coordinates in the unit cell. The negative derivative of the enthalpy $\mathcal{H}$ with

respect to X is given as force vector F.

$$F = -\frac{\partial \mathcal{H}}{\partial X}|_p \tag{2.67}$$

The derivatives of $\mathcal{H} = E + p\Omega$ with respect to ε are strain components $f^{(\varepsilon)}$ of F. The energy E per unit cell is a function of the lattice vectors matrix $h = a, b, c$ and the unit cell volume Ω is equivalent to $\det(h)$. The strain components can be defined as

$$f^{(\varepsilon)} = -(\sigma + p\Omega)(1 + \varepsilon^T)^{-1} \tag{2.68}$$

where σ is the stress at a given configuration X

$$\sigma = \left(\frac{\partial E((1+\varepsilon')h)}{\partial \varepsilon'}\right)_{\varepsilon'=0} \tag{2.69}$$

and ε can become asymmetric in the course of relaxation. The other $3N$ components of F in the $(9+3N)$-dimensional space of F are obtained by multiplying the forces on the atoms $f_1, \ldots, f_N$ in lattice coordinates with metric tensor $g = h^T h$, hence the complete F is express as

$$F = \left(f^{(\varepsilon)}, gf_1, \ldots, gf_N\right)^T \tag{2.70}$$

Given the first derivative, to find the minima of the multivariable functions (eq. 2.70), the BFGS algorithm is a more reliable choice due to its stability and efficiency [71]. When close enough to a minimum X_{min}, enthalpy change $\delta\mathcal{H}$ can be approximated by

$$\delta\mathcal{H} = \frac{1}{2}(X - X_{min}) \cdot A(X - X_{min}) \tag{2.71}$$

The exact minimum X_{min}, cannot be computed straight away because the Hessian matrix A is unknown, so an initial guess for A is used iteratively to perform the relaxation. Actually it is the inverse $H = A^{-1}$ of A that is being developed. In relaxation step $i+1$, the earlier position X_i is updated according

to the quasi-Newton rules

$$X_{i+1} = X_i + \lambda \Delta X_i \tag{2.72}$$

$$\Delta X_i = H_i F_i \tag{2.73}$$

where F_i is F evaluated at X_i and λ is the step length derived from an approximate line minimization along the step direction ΔX_i. With an initial guess H_0 for H as input, the BFGS quasi-Newton scheme is updated according to

$$H_i = H_{i-1} - \frac{(X_i - X_{i-1}) \otimes (X_i - X_{i-1})}{(X_i - X_{i-1}) \cdot (F_i - F_{i-1})} - \frac{(H_{i-1}(F_i - F_{i-1})) \otimes (H_{i-1}(F_i - F_{i-1}))}{(F_i - F_{i-1}) \cdot H_{i-1}(F_i - F_{i-1})} + [(F_i - F_{i-1}) \cdot H_{i-1}(F_i - F_{i-1})] U \otimes U \tag{2.74}$$

$$U = \frac{(X_i - X_{i-1})}{(X_i - X_{i-1}) \cdot (F_i - F_{i-1})} - \frac{H_{i-1}(F_i - F_{i-1})}{(F_i - F_{i-1}) \cdot H_{i-1}(F_i - F_{i-1})} \tag{2.75}$$

To guarantee a sensible step size during the first few relaxation steps, H_0 should be initialized properly. It is imperative that H_0 does not disrupt the symmetry when it is applied to a force vector F. Dependence of the enthalpy on ε is governed by the bulk modulus. Upon movement of the atomic coordinates from the equilibrium positions, increase in enthalpy is determined by the optical phonon frequencies at the Brillouin zone center. The line minimization needed to find λ in equation 2.72 cannot be performed exactly, and λ is usually assigned a value of 1. With the BFGS method, an approximation to the Hessian matrix is built up over successive electronic minimisation steps.

The initialization of H_0 can be done as block diagonal with (3×3) matrices of the form $g_0^{-1} \bar{M}^{-1} \bar{\omega}_O^{-2}$ and setting the strain part of H_0 to a (9×9) identity matrix multiplied by $(3\Omega B_0)^{-1}$ [71]. H_0 is then express as:

$$H_0 = \begin{pmatrix} (3\Omega B_0)^{-1} & & & & & & 0 \\ & \ddots & & & & & \\ & & (3\Omega B_0)^{-1} & & & & \\ & & & g_0^{-1}\bar{M}^{-1}\bar{\omega}_O^{-2} & & & \\ & & & & \ddots & & \\ 0 & & & & & & g_0^{-1}\bar{M}^{-1}\bar{\omega}_O^{-2} \end{pmatrix}. \tag{2.76}$$

Here B_0 is the bulk modulus, $\bar{M}$ is the average mass of the atoms, g_0 is the initial configuration metric tensor, and $\bar{\omega}_O$ is the average optical phonon frequencies at the Brillouin zone centre. In equation (2.76), B_0 and $\bar{\omega}_O$ are the only free input parameters, which are usually estimated when H_0 is initialised. To initialise H_0 in this PhD study, an initial estimate of 500 GPa and 1668 cm^{-1} has been maintained throughout for the bulk modulus and phonon frequency, respectively.

2.6 Computational Code and Softwares

In this section, I briefly introduce the DFT code used throughout this thesis and other supporting software packages.

2.6.1 CASTEP Package

The density functional theory calculations in this thesis are executed using the software package CASTEP [72], which stands for CAmbridge Serial Total Energy Package. CASTEP is a leading first-principles quantum mechanical modelling code. It uses the plane-wave basis set and pseudopotentials methods for the description of a materials electrons and nuclei. The development of this code started in the late 1980s at the Cavendish Laboratory in Cambridge by M. C. Payne[2]. Typically, CASTEP is applied to study surfaces, structural, electronic and optical properties of materials. CASTEP optimizes the atomic geometry of a system using the BFGS method by default, until the total energy

[2] `www.tcm.phy.cam.ac.uk/about/history`

of the structure is minimized.

CASTEP is written in modern Fortran language and is capable of parallel computing. A high performance computing (HPC) cluster named Minerva was mainly used to run the CASTEP simulations. Minerva was a regional HPC facility based in Warwick University and has been decommissioned in January, 2017. The system configurations for Minerva is as follows: 2500 Westmere cores with 234 compute nodes, based on IBM iDataPlex hardware, with storage capacity 160 TB GPFS[3].

In addition, a smaller cluster called Syrah, which is owned by the Surface, Interface and Thin films group of the Department of Physics, was used to carry out DFT calculations as implemented in CASTEP. Syrah is a Linux system with 48 cores and 6 nodes.

Materials Studio Visualizer was used to construct the input structure models for CASTEP, as well as analyse the band structure, density of states and other properties from the finished calculations. Materials Studio is a wide-ranging modelling and simulation tool designed to allow researchers in the materials fields to predict and understand the characteristics of materials at the atomic and molecular level [73].

2.7 Surface, Slab and Interface Models

Surfaces are usually studied using a DFT code that applies periodic boundary conditions in three dimensions. The basic idea is to build a supercell as shown in figure 2.3 that contains atoms along a portion of the vertical direction only. In the top portion of the supercell an empty space has been left above the atoms, while in the bottom part atoms fill the entire supercell in the x and y directions. This is called a slab model and the empty space above the atoms along the z direction is called the vacuum space. It is essential when using a slab model to create sufficient vacuum space, so that the upper and lower surface of the slab does not interact [43]. In the vacuum region, the electron density of the material decreases to zero. The surface energy, σ (energy needed to cleave the bulk crystal), can be determined from a DFT slab calculation by

[3] `www2.warwick.ac.uk/research/rtp/sc/hpc`

applying equation 2.77.

$$\sigma = \frac{1}{A}\left[E_{slab} - nE_{bulk}\right] \tag{2.77}$$

where the total energy of the surface slab model is represented by E_{slab}, the energy per atom in the bulk material is E_{bulk}, the number of atoms in the slab model is given by n, and the total area of both surfaces in the slab model is A.

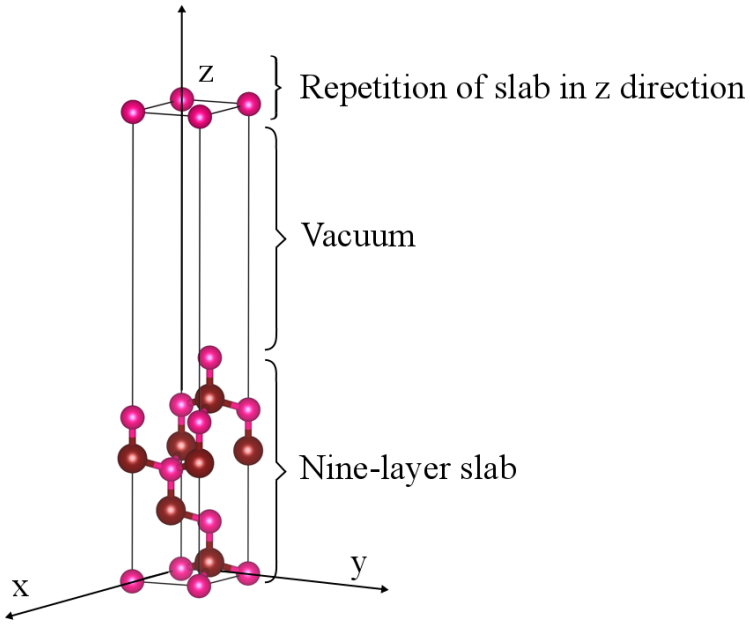

Figure 2.3: Supercell that defines a surface slab model used in a DFT calculation with periodic boundary conditions in all three dimensions.

An interface model in a periodic calculation can be built in two ways: first, with a vacuum separating periodic repeat of the system along the z direction and secondly, without vacuum between periodic repeat of the supercell in all three dimensions. Figure 2.4(a) gives an illustration of the first case where there is a vacuum gap between material I and material II. Here I have a I/II interface, a II/vacuum interface (a surface) and a I/vacuum interface (surface). This increases the computational effort due to the added volume of the simulation cell, and could lead to large surface energy, diverged electrostatic energy and disruptive surface reconstructions in most cubic structures

along the (111) direction. The dangling bonds formed when a III-V system is cleaved in the (111) direction makes the surface unstable and polar (see section 1.3). Now depending on the surface properties and any passivation (e.g termination of a dangling bond with H), a few layers of material I or II might be enough to recover the bulk properties far from the interface and surface(s) in this interface model.

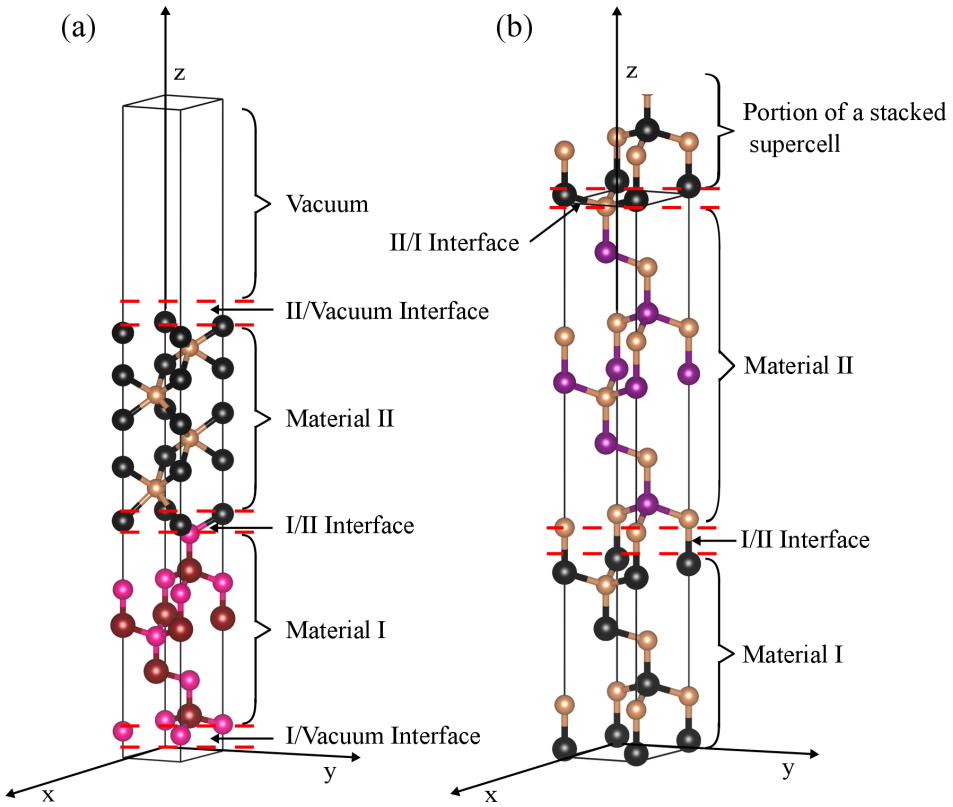

Figure 2.4: (a) Supercell that defines an interface model with vacuum in the z direction. (b) Supercell that defines an interface model without vacuum in all dimensions. A repetition of the supercell is partly shown in the z direction to provide a vivid picture of the II/I interface.

In the second interface model without vacuum separating periodic repeat of the supercell, two non-identical interfaces are formed: I/II and II/I interface, as shown in figure 2.4(b). The supercell should be large enough to recover bulk-like properties at the center of both materials I and II, so that effects of the two interfaces do not overlap. Typically, 7 to 9 atomic layers of each material type should be enough.

Both types of interface models give an approximation of what the exact interface between two macroscopic regions is. The amount of errors introduced in each approach depends on the properties that are being calculated. It is important to choose a cell that has similar interfaces. However, the two interfaces will probably be different, so computing the energy of each requires calculating several interface combinations. To minimize strain energy, it is best to use materials with lattice parameters that match closely. During the interface simulations, the atoms are allowed to undergo full relaxation within the confines of the periodic super cell structure. Although, one can also constrain the movement of the atoms (no movement in the x- and y-direction) by allowing them to relax in the z-direction only, which in turn will save computing time. Depending on the type of atoms connecting materials I and II, a strong or weak interfacial bond is formed, leading to a new material system (if the interface binding is strong enough). The strength of the interface formed between two materials can be computed from the work of separation: the reversible work (W_R) per interfacial area needed to separate an interface into two free surfaces. It describes the binding strength of the interface atoms. Therefore, if an interface has the highest adhesion energy, then it is said to be more stable than the others. In DFT calculations, it is common to express W_R as [74, 75, 76]:

$$W_R = \frac{1}{A}\left[E_I + E_{II} - E_{I/II}\right] \tag{2.78}$$

where E_I and E_{II} are respectively the total energies of the isolated slabs of materials I and II, $E_{I/II}$ is the total energy of the supercell and A is the total area of all interfaces. The total area is given as $2A$ for an interface without vacuum and approximately two identical interfaces (see figure 2.5). But in reality surfaces do reconstruct to form lower energy surfaces. For instance the GaAs(111)A-(1×1) surface usually reconstructs to a (2×2) surface as given in figure 1.6. Surface reconstruction energies need to be accounted for. Also, strain energies at the interface between dissimilar materials will be generated. If the two materials lattice parameters are closely matched, the interfacial strain energy is negligible. Assuming materials I and II have a closely matched

lattice parameters, the strain energy can be ignored and W_R written as:

$$W_R = \frac{1}{A}\left[E_I + E_{II} - E_{I/II}\right] + \left[\sigma'_{IA} - \sigma_{IA} + \sigma'_{IB} - \sigma_{IB}\right] + \left[\sigma'_{IIA} - \sigma_{IIA} + \sigma'_{IIB} - \sigma_{IIB}\right] \quad (2.79)$$

where $\sigma_{IA}(\sigma_{IB})$ and $\sigma'_{IA}(\sigma'_{IB})$ are respectively the reconstructed and unreconstructed but relaxed top (bottom) surface energies of the isolated slab of material I. Similarly, $\sigma_{IIA}(\sigma_{IIB})$ and $\sigma'_{IIA}(\sigma'_{IIB})$ defines the surface energies of the isolated slab of material II. Formation of the interfacial bonds among the atoms at the interface can be described by the charge density difference. The electronic charge density difference when computed with respect to atoms, can be expressed as:

$$\Delta\rho = \rho_{\text{Interface}} - \Sigma\left(p_i\right), \quad (2.80)$$

where $\rho_{\text{Interface}}$ is the charge density of the whole interface system, and ρ_i is the electron density of each atom, with the subscript i running over all atoms. This illustrates the variations in the electron distribution as the bonds are formed.

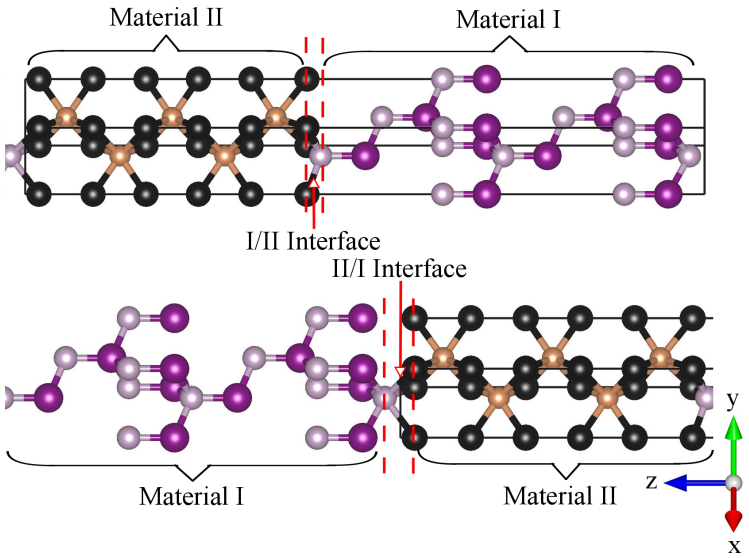

Figure 2.5: The two interfaces in a supercell without vacuum placed side by side for the purpose of comparison. Their interfacial layers are identical.

Chapter 3

Half-metallicity of *c*-MnSb and *c*-MnSb/InSb(111) interfaces

3.1 Introduction

Half-metallic materials with zinc-blende (ZB) structure are promising candidates to design and fabricate stable structures on semiconducting substrates with the capacity for efficient spin injection into semiconductors [77, 78, 79, 80, 81]. These materials have the advantages of being structurally compatible with widely used ZB semiconductors (GaAs, InSb and InP) and possess high Curie temperatures (T_C) as well as large magnetic moments [82, 6, 83]. Thin films of half-metallic MnSb, MnAs, CrAs, and CrSb with ZB structures have been grown successfully at room temperature [6, 84, 85, 86], but there is still the issue of spin polarization being sensitive at the interface region [87, 88, 89]. It is important to address half-metallicity at ZB HMF/ZB semiconductor interfaces.

The ferromagnetic binary compound *c*-MnSb has been predicted to be 100% spin-polarized at the Fermi level, and can be experimentally grown on *n*-MnSb with GaAs substrate through molecular beam expitaxy [6]. The robustly half-metallic cubic (*c*-) polymorph of MnSb is metastable and its epitaxial growth on *n*-MnSb is challenging [6]. However, *c*-MnSb has a reliable experimental lattice parameter from growth on *n*-MnSb-on-GaAs. This lattice parameter is reasonably matched to that of InSb (a small lattice mismatch of

2.3% exist between c-MnSb and InSb), which has a high conductivity. Motivated by this, I have modelled the growth of c-MnSb on InSb along the (111) direction. Here I investigate the structural, electronic and magnetic properties of the interface between the half-metallic binary compound c-MnSb with the III-V semiconductor InSb. By calculating the work of separation I evaluate the interface strength for all the possible interface layer orderings of the c-MnSb(111)/InSb(111) superlattice. One interfacial geometry maintains a high spin polarization while the other three differ greatly from bulk c-MnSb.

3.2 Computational Methods and Calculated bulk Properties

Density functional theory calculations were carried out with the CASTEP package [72], in which the plane wave pseudopotential method has been implemented. The generalized gradient approximation (GGA+U) exchange-correlation functional given by Perdew-Burke-Ernzerhof (PBE) [57] was used due to its ability to account for the Coulomb interactions of strongly correlated systems. A Hubbard U term of 2.0 eV for Mn was used throughout the calculations except in Fig. 3.3(a), where the effect of U parameter on the ground state energy and the magnetic moment was investigated. A Hubbard U of 2.0 eV had little or no influence on the ground state energy and magnetic moment, though the minority spin gap was further opened up. Ultrasoft pseudopotentials [67] have been mainly used for our calculations to model the electron-ion interaction with an added Mn non-linear core correction [90]. I have performed full geometry optimizations for the cell parameters and atomic coordinates of bulk MnSb in the zinc-blende structure (see Fig. 3.1) as well as its interfaces with semiconductor InSb along the (111) direction.

During the calculations, a primitive unit cell was used for the bulk whereas for the (111) interface we adopt multiple supercells with 19 layers of c-MnSb and 13 layers of InSb. A value of 400 eV was used as the cut-off energy in the plane wave expansion, while for the Brillouin zone integration we used $7 \times 7 \times 7$ Monkhorst-Pack ($\mathbf{k}$) mesh [91] for bulk MnSb and $7 \times 7 \times 1$ $\mathbf{k}$ meshes for the c-MnSb/InSb(111) interfaces. Convergence tests with respect to both

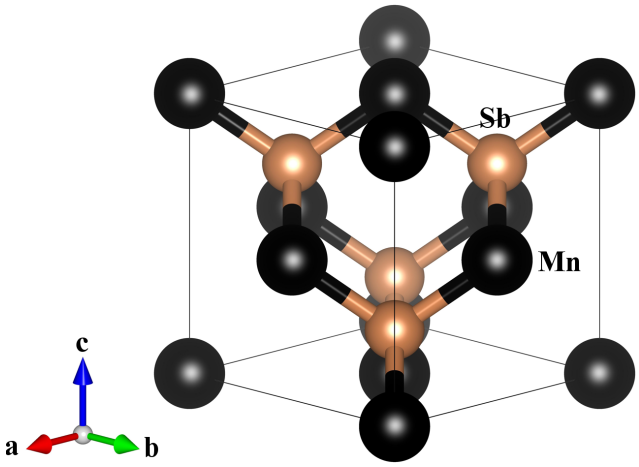

Figure 3.1: Cubic (c)-MnSb in a zinc blende type structure (F4$\bar{3}$m) with Mn (Black) at the (0 0 0) and Sb (Brown) at the (0.25 0.25 0.25) sites.

of these parameters (Fig. 3.2) indicated that the results were well converged at the cut-off energy of 400 eV and **k**-point grid of $7 \times 7 \times 7$.

I calculated equilibrium lattice constants of c-MnSb and InSb by varying their lattice parameter (Å) within the range of values 5.80 Å to 6.60 Å, then fitted the ground state energy versus lattice parameters plot with the Birch-Murnaghan equation of state [92, 93]. This is illustrated in Fig. 3.3(b) for bulk MnSb with lattice parameters ranging from 5.80 Å to 6.60 Å. The computed lattice constants for both ZB InSb and MnSb are generally in good agreement with experimental values and other calculations as shown in table 3.1. Table 3.1 compares the calculated lattice constants from PBE+U and LDA+U functionals with experiment as well as values from previous pseudopotential method calculations. A lattice mismatch of 2.3% between c-MnSb and InSb(111) is observed, and this causes a small strain at the interface when c-MnSb/InSb heterojunctions were constructed. The total magnetic moment, charge density difference, band structure and density of states (DOS) of c-MnSb were calculated in order to see what effect the strain had on the half-metallicity of MnSb.

The calculations in this work yielded an integer value for the net spin magnetic moment per primitive cell of 4.00 μ_B, which is a typical behavior of half-metals [99]. To verify the half-metallicity, the k-resolved band-structure

Table 3.1: Lattice parameters (Å) of InSb and c-MnSb.

Species	**PBE+U**	**LDA+U**	**Other Calculations**	**Experiment**
InSb	6.45	6.45	6.28[94]	6.48[95, 96]
c-MnSb	6.32	6.20	6.21[27], 6.25[97]	6.44[98]

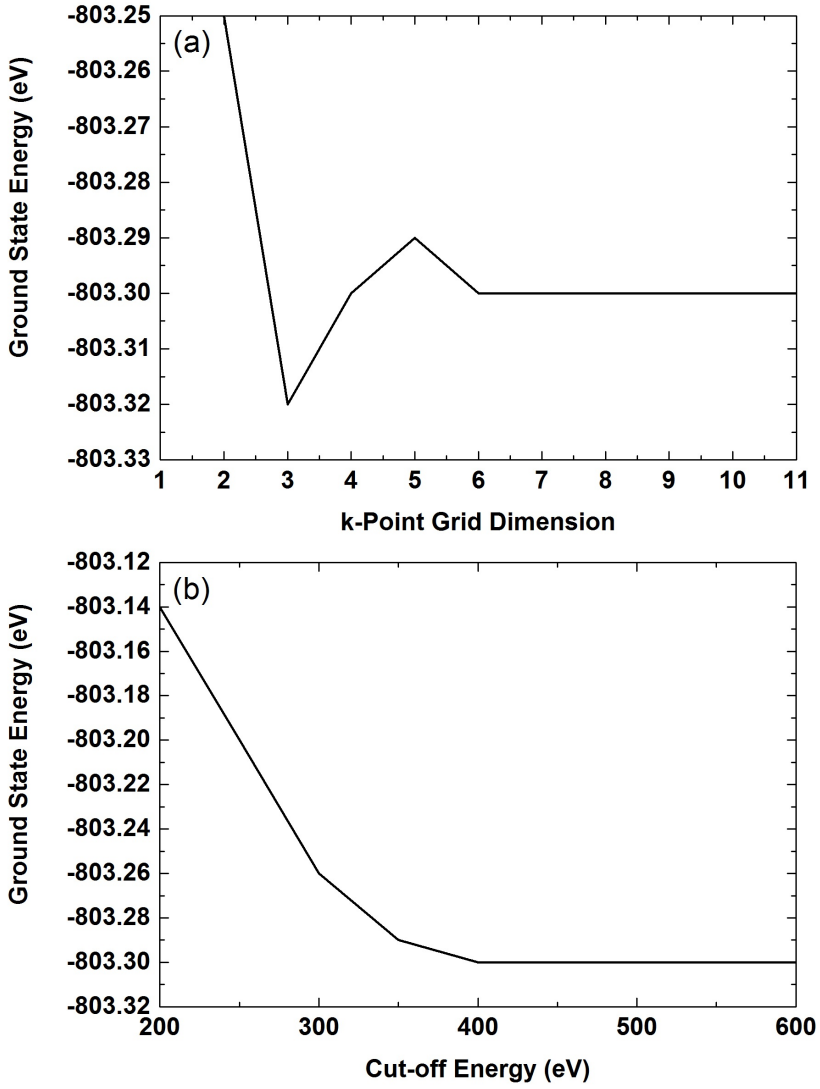

Figure 3.2: Convergence tests done for bulk c-MnSb ground state energy with respect to (a) $\boldsymbol{k}$-point (meshes) sampling and (b) Cut-off energy.

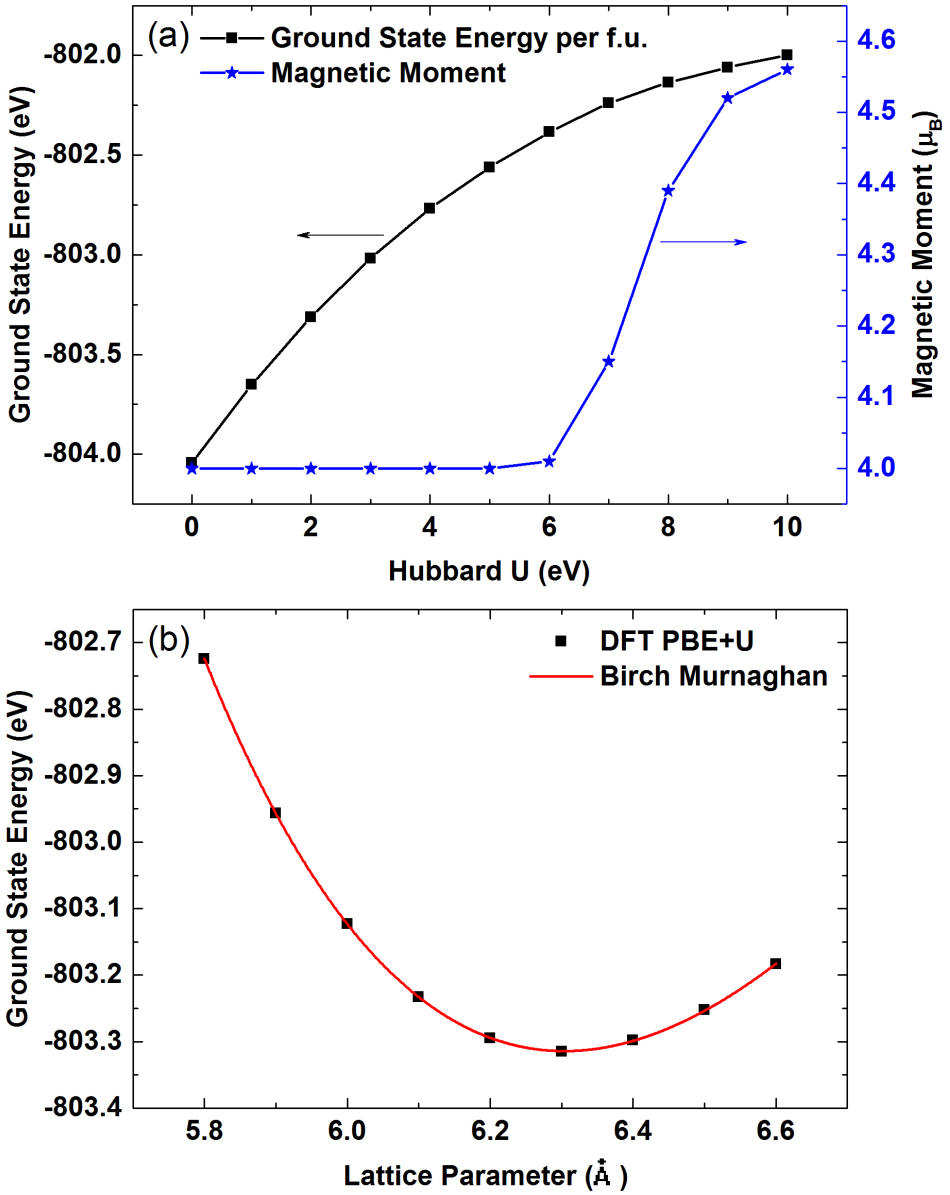

Figure 3.3: (a) The effect of Hubbard U parameters on the ground state energy per formula unit (f.u.) and magnetic moment. (b) Ground state energy vs. lattice parameter for *c*-MnSb within PBE+U. DFT data points indicate by small squares were fitted with the Birch Murnaghan equation represented by the red curve.

plot in Fig. 3.4 was examined. This shows a robust half-metallic character, with the spin-up channel being metallic whereas the spin-down channel displays a bandgap of 1.49 eV around the Fermi level. The value obtained for the bandgap agrees closely with previous works [27, 100]. In addition, the DOS is presented in Fig. 3.5, which exhibit a spin-polarization of 100% at the Fermi level. An electronic charge density difference plot is shown in Fig. 3.6 which illustrates the covalent bonding nature of the Mn-Sb bond [101, 102]. In the contour map red regions represent electron rich areas, and blue regions represent electron deficient areas. While white regions are areas with little interaction.

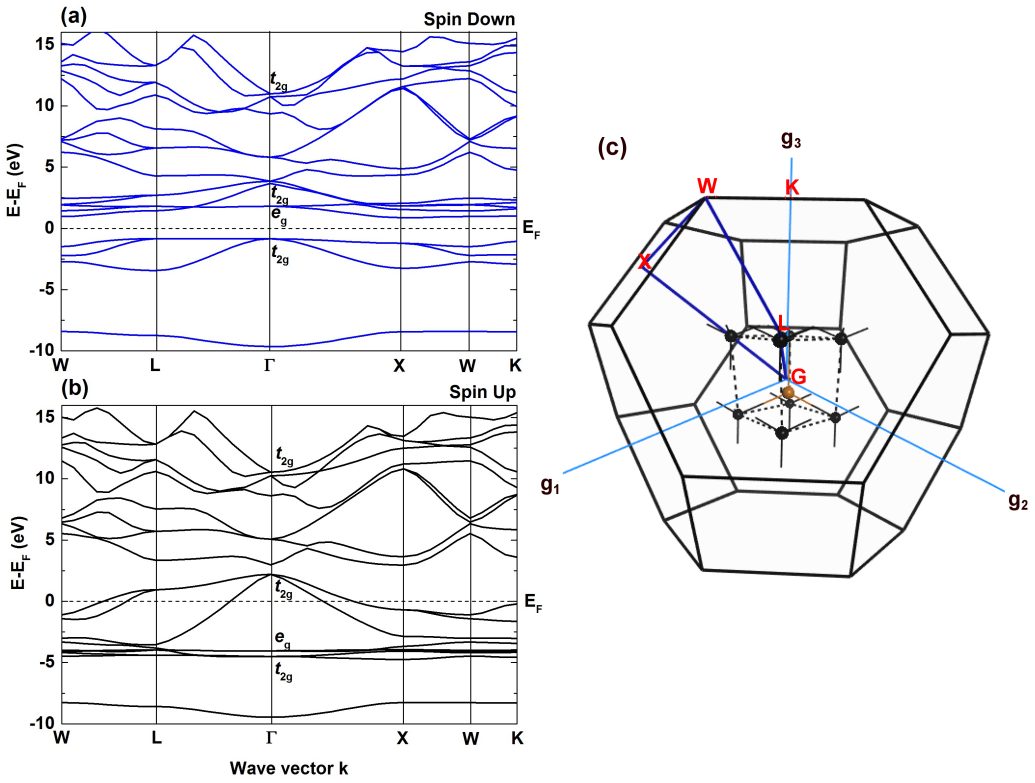

Figure 3.4: Band Structure of bulk MnSb in the zinc blende structure, showing spin-down channel (a), spin-up channel (b) and bulk brillouin zone of cubic MnSb (c). The zero of energy is ascribe the Fermi level and the high symmetry points in the brillouin zone are assigned labels like Γ (G), X, W, K, L.

A closer look at the band structure of fig. 3.4 shows the half-metallicity originating from large bonding-antibonding splitting (weakening the p-d hybridization of p and t_{2g} states) and small exchange splitting (minority e_g states

being pushed up), which agrees with ref [93, 96, 103]. Measured from the gamma point (Γ), the p bands are around -4.50 eV, next the e_g bands around -4.04 eV for majority bands and +1.80 eV for minority bands. Due to weak hybridization of the e_g states, these bands are flat. The antibonding p-t_{2g} hybrids follows with +2.20 eV for majority bands and +3.65 eV for minority bands. Their strong hybridization and high energy position results in a large bandwidth.

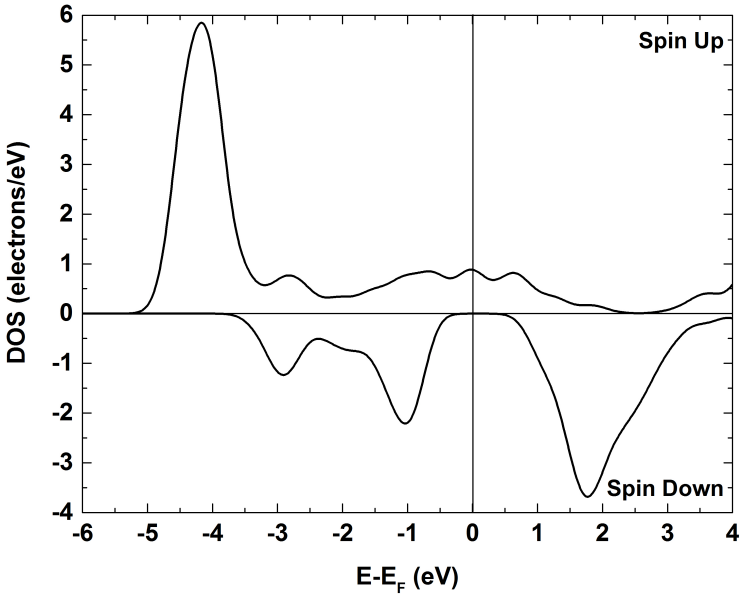

Figure 3.5: The total DOS of c-MnSb. The Fermi level has been set to zero (0) eV on the x-axis.

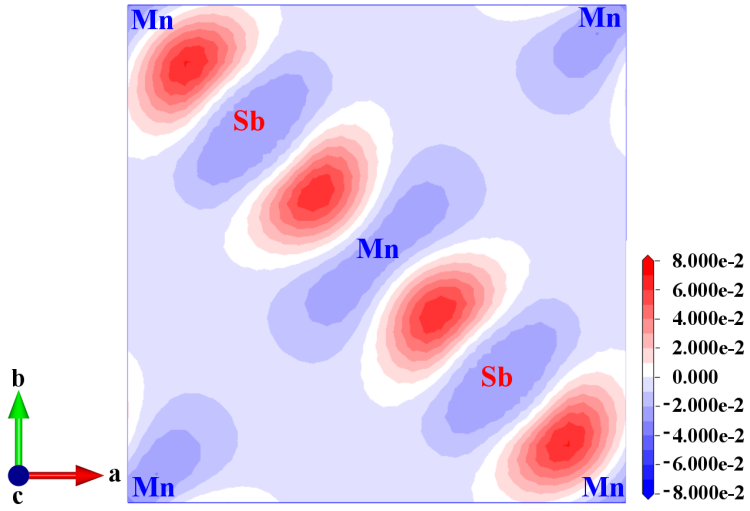

Figure 3.6: Charge density difference 2D plot of *c*-MnSb viewed along the *c*-axis. Contour maps: electron deficient region in blue, and regions in red is electron enrich. Small changes in electron density is white region. The field values ranges from -0.08 to 0.08 e/Å^2.

3.3 *c*-MnSb(111)/InSb(111) superlattices

The cubic MnSb/InSb interfaces were modelled by building up layered structures of *c*-MnSb on InSb layers along the (111) planes. The surface of *c*-MnSb (111) can be terminated with Mn or Sb atom, likewise, InSb (111) can be In-terminated or Sb-terminated. Hence, I considered the four possible ways of making the *c*-MnSb/InSb (111) interface as shown in fig. 3.7. In fig. 3.7(a) *c*-MnSb (111) surface is terminated with Mn, and an Sb atom terminates the InSb (111) surface. I call this interface Mn-Sb and in a similar fashion Mn-In, Sb-In as well as Sb-Sb terminations are named [fig. 3.7(b)-(d)]. In the interfacial calculations I used periodically repeating unit supercells constructed from three MnSb unit cells and two InSb unit cells along the [111] direction. The in-plane lattice parameters of the slabs were set to the surface lattice parameter of InSb (111) (a / ($\sqrt{2}$) = 4.56 Å) given a = 6.45 Å from our DFT bulk-relaxed structure, while the out-of-plane inter-layers for the interface models and atoms fractional coordinates went through full structural relaxation using the BFGS algorithm [70, 71]. The optimized interfacial bond length, after

the structures were fully relaxed is given in Table 3.2. From the table it is shown that the Mn-Sb (Sb-In) bond lengths of 2.78 Å (2.87 Å) at the Mn-Sb (Sb-In) interfaces are quite close to their optimized bond lengths 2.74 Å (2.75 Å) in the bulk systems, which means atomic bonding exists at the interface of c-MnSb with InSb.

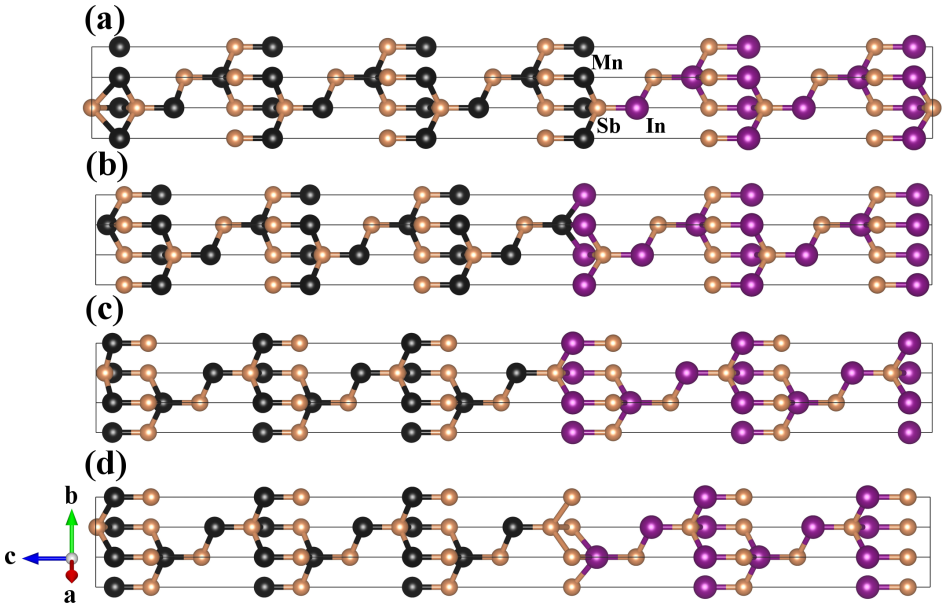

Figure 3.7: Optimized *c*-MnSb/InSb(111) heterojunction. Black (brown) spheres represent Mn (Sb) atoms, while purple spheres represent In atoms. The four possible terminations at the interface for this layered structure are: (a) Mn-Sb, (b) Mn-In, (c) Sb-In and (d) Sb-Sb terminations.

The work of adhesion or separation (W_R) for the fully relaxed interface configurations of MnSb/InSb layered structures were calculated, in order to investigate their interface stability (see equation 2.78). Considering the interfaces of *c*-MnSb/InSb (111), the work of separation W_R can be computed using equation 2.78. The expression for work of separation or adhesion energy (W_R) given in equation 2.78 has been used throughout this study to determine the adhesion energy. There are two identical interfaces in each supercell which the factor one-half accounts for. The calculated work of separation for the *c*-MnSb/InSb (111) interfaces are listed in Table 3.2. I find that the interface with Mn-Sb termination has the highest adhesion energy of 1.65 J/m^2 among

the four configurations, which points to the fact that it is the most stable model, due to its smaller atomic bonding distance of 2.72 Å when compared to the other *c*-MnSb/InSb(111) interfaces. Conversely, Mn-In with the least work of separation will be difficult to form as the cation-cation interaction is energetically unstable.

Table 3.2: The optimized bond length between the interfacial atoms, the calculated work of separation and spin magnetic moment of the interface Mn atom for the four considered configurations of the *c*-MnSb/InSb (111) interfaces. An asterisk (∗) indicates the magnetic moment for cases where the Mn atom is located in the subinterface layer.

Interface termination	**Bond Length (Å)**	**Work of Separation (J/m^2)**	**Magnetic Moment (μ_B)**
Mn-Sb	2.78	1.65	4.31
Sb-In	2.87	1.36	4.09∗
Sb-Sb	2.98	1.13	4.12∗
Mn-In	3.07	0.82	4.43

Atomic bonding at the interface can give insight to the structural properties of an interface. Presented in Fig. 3.8 is the charge-density difference in two dimensional (2D) contour maps for (a) lateral view of the Mn-Sb termination, slicing through the interfacial Sb atom and (b) top view along the *c*-axis with the slice cutting through the interfacial bonds. The charge density difference is calculated by subtracting individual atomic charge densities from the electron density of the whole system. It is clear from the figure that a substantial bonding charge (red areas at the interface region) has been redistributed between Mn and Sb ions, which is an indication of covalent bonding [101, 102].

In order to investigate whether the bulk *c*-MnSb half-metallic property is preserved at the interface of *c*-MnSb/InSb heterojunctions, I show the partial density of states (PDOS) for the first three layers of the *c*-MnSb slabs in Fig. 3.9. It can be seen from the figure that the half-metallicity was not preserved at all four interfaces. However, it was maintained from the bulk up to the subinterface layer (Layer2) except for the Sb-Sb configuration as in Fig. 3.9(d). Taking a closer look at the Mn-Sb and Sb-In interface configura-

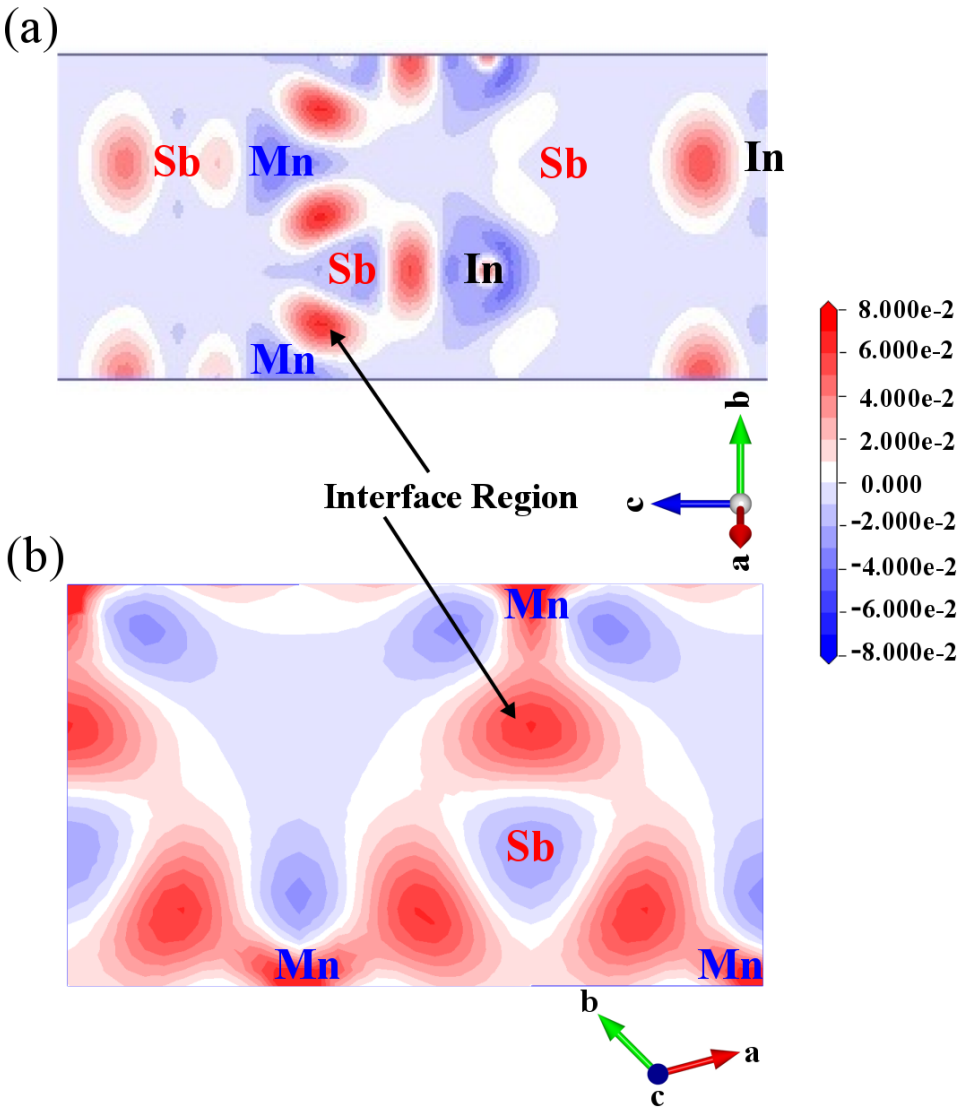

Figure 3.8: Charge density difference maps of the atoms in Mn-Sb model, sliced at the interface; (a) lateral view (b) viewed along the c-axis. Contour maps: electron deficient region in blue, and regions in red is electron enrich. Small changes in electron density is white region. The field values ranges from -0.08 to 0.08 e/Å^2.

tions reveals a 92.6% spin polarization (using equation 1.2) for the interface layer of Mn-Sb termination and 29.2% polarization for Sb-In termination respectively, as shown in Fig. 3.10. The atom-resolved DOS in bulk c-MnSb and InSb is compared with their respective interface atoms, which gives an idea of how much the electronic structure of these systems changes at the interface. As can be seen for the case of Sb-In interface order fig. 3.10(a), the atomic DOS at the interface changed a lot from is bulk shape and the half-metallic gap destroyed. The interface Mn PDOS in Mn-Sb termination did not change much, as shown in fig. 3.10(b). Interestingly, the interface Sb from InSb slab increases the spin polarization (see Fig. 3.11(a)) a bit by mimicking the Sb PDOS shape of bulk *c*-MnSb as can be seen in the bottom figures of Fig. 3.10(a) and (b). A 40% spin polarization was observed well into the InSb slab as indicated by the blue triangular data points in fig. 3.11(a) representing the first and second In atomic layer. Also, for the Mn-Sb layer order, the magnetic moment of Mn atom at the interface increases by 0.31 μ_B when compared with the magnetic moment per Mn atom in bulk *c*-MnSb (see table 3.2).

Now I explore the electronic properties of the Mn-Sb and In-Sb terminated interfacial structures further. Figure 3.11 shows the behavior of spin polarization for these models as a measure of distance from their interface. In both cases the spin polarization is 100% from the middle of *c*-MnSb slab (i.e around -18.5 Å) up until the sub-interface layer and this supports the claim that the *c*-MnSb/InSb(111) slabs are thick enough to recover the half-metallicity of *c*-MnSb. At the In-Sb interfacial termination, spin polarization decreases significantly at the interface layer to 29.2% and increases to 47.0% on the first atomic layer of the InSb slab. The Mn-Sb interface spin polarization drops slightly to 92.6%, then rises to 95.1% at the interface layer of the InSb slab, before dropping further towards the middle of the InSb slab. This shows that the size of InSb slab is also sufficient, since the gap states induced by spin polarized calculation decays deeper into the semiconductor [104, 105].

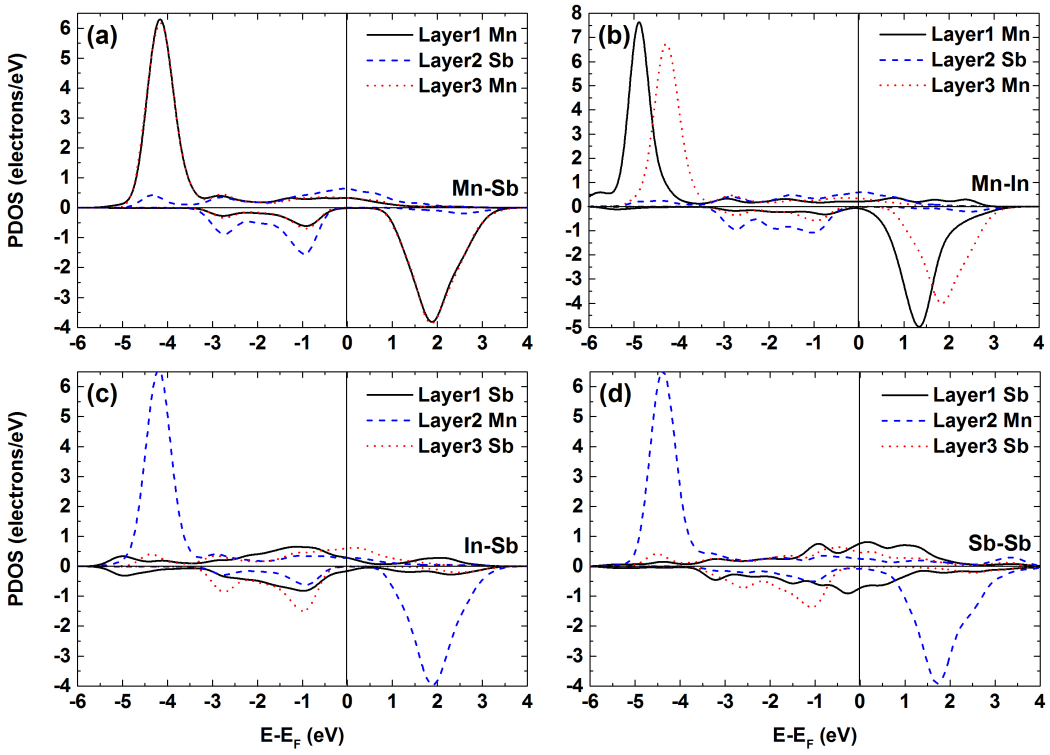

Figure 3.9: Partial density of state plots for the three layers of MnSb closest to the interface for the four different interface terminations with (a) Mn-Sb showing an enhanced polarization of 92.6% at the interface. Then, (b) Mn-In (c) Sb-In and (d) Sb-Sb terminations.

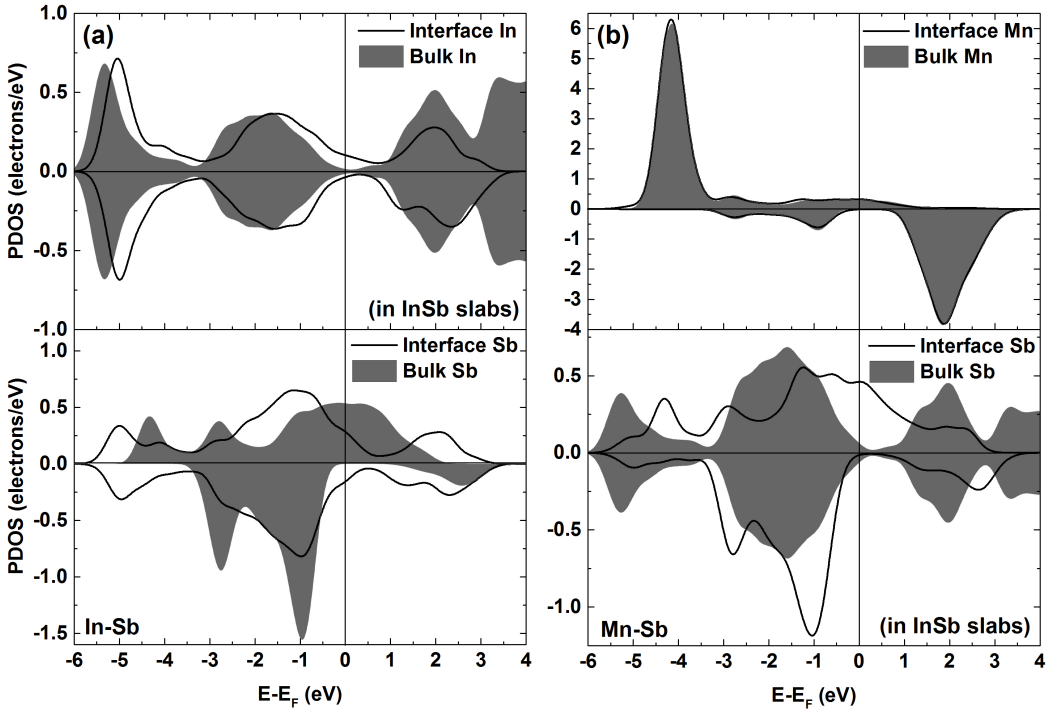

Figure 3.10: Partial DOS for the interfacial atoms of the *c*-MnSb/InSb(111) for the configurations of (a) Sb-In and (b) Mn-Sb. The atomic partial DOS in bulk systems, indicated by gray shaded areas are presented for comparison.

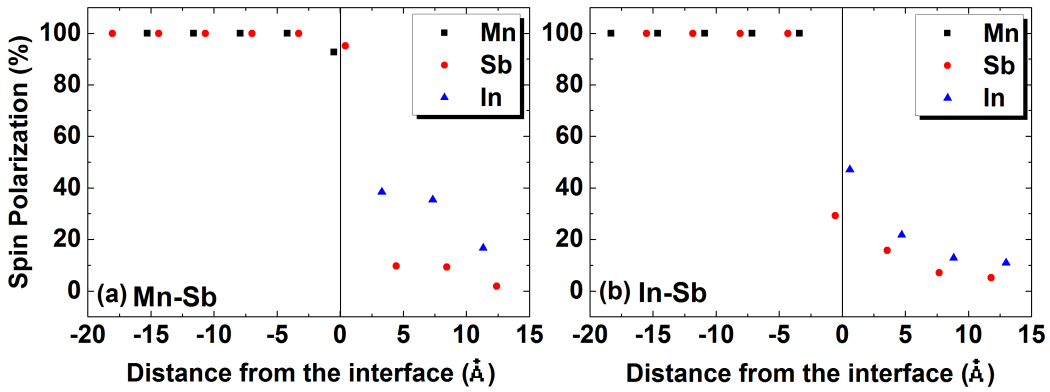

Figure 3.11: Spin Polarization as a function of the distance from the *c*-MnSb/InSb(111) interface, (a) Mn-Sb and (b) Sb-In termination. Zero marks the interface and each data point represents an atomic layer.

3.4 Summary

Multilayered structure of c-MnSb(111)/InSb(111) has been modelled using the plane wave pseudo-potential method. The Mn-Sb interface termination of c-MnSb(111)/InSb(111) is energetically more stable with the shortest bond distance of 2.78 Å and has a high spin polarization of 92.6% at the interface. Normally interfaces are seen as problematic in half-metallic FM structures, reducing or even reversing spin polarization [89], so this behavior is unusual. This is the first time a spin polarization that is close to 100% is obtained at the interface between zinc blende compounds. Although, high spin polarization at the interface between a HM and III-V semiconductor has been reported before [106]. Spin polarization of about 40% was seen well into the InSb slab. An increase in Mn spin magnetic moment from a bulk value of 4.0 μ_B to the interface layer value of 4.31 μ_B is observed. The other sequences of the interface layers are ferromagnetic but not half-metallic. Thus controlling the growth conditions in an experiment may lead to further stabilization of the c-MnSb/InSb(111) interface.

Chapter 4

Ferromagnetic *n*-MnSb on III-V Semiconductors

4.1 Introduction

The ferromagnetic binary compound MnSb [6, 12] is a highly promising material for room temperature semiconductor spintronic applications [6, 16, 107], such as information storage devices [14]. I decided to model the growth of *n*-MnSb on InP and GaAs substrates for several reasons. This was motivated by the works of Aldous *et al*, on MnSb and the suggestion of Sanvito and Hill (2000) [103] that a volume stretch may lead to a phase transition from the NiAs type structure to zinc blende structure. The interface polarization may be achieved by tetrahedral-like coordination of Mn at the interface [99]. Also, Ploog's [108] experimental work has provided evidence of spin-injection for similar material systems. The *n*-MnSb polymorph (hexagonal; $a = 4.12$ Å, $c = 5.77$ Å) does not grow well on InP directly but its a lattice constant conveniently matches the symmetry and surface lattice parameter of InP(111) ($a/\sqrt{2} = 4.15$ Å) [14]. Here I report on the electronic and structural properties of the interfaces between the niccolite (*n*-) polymorph of ferromagnetic (FM) MnSb and the III-V semiconductor InP and GaAs.

I have studied the *n*-MnSb(0001)/InP(111) and *n*-MnSb(0001)/GaAs(111) directions by performing plane-wave pseudopotential DFT [43] calculations as implemented in the CASTEP code [72], to investigate the structural, electronic

and magnetic properties at the interface of these heterostructures. Various interface ordering for the layered structures of n-MnSb(0001)/InP(111) and n-MnSb(0001)/GaAs(111) were modelled, with the BFGS optimization performed using ultra-soft pseudopotentials to relax the structures [67, 71]. The GGA+U PBE exchange correlation functional was used with cutoff energy of 400 eV and Monkhorst Pack **K** points 7×7×1 [57, 91]. Hubbard U value of 1.0 eV on Mn was adopted to properly account for the electronic structure and magnetic moment of the n-MnSb slab. Here, a different U value on Mn atom for MnSb has been used because different crystal structures ought not to have the same values of U [61]. And a Mn U value of 1.0 eV on n-MnSb, generate theoretical properties (magnetic moment and lattice parameters) that are in good agreement with experimental results.

All the details stated in the preceding paragraph, as well as the computational conditions are maintained throughout this chapter with few exceptions.

4.2 *n*-MnSb(0001)/InP(111) superlattices

4.2.1 Model Preparation

The n-MnSb(0001)/InP(111) supercell was constructed in a way that the two interfaces within the supercell are identical and have an interface atomic arrangement which allows both layers to be connected with three bonds. The four possible interface orders are: Mn-P, Mn-In, Sb-In and Sb-P terminations. This multilayer consist of 11 and 13 atomic layers for n-MnSb and InP, respectively. These thickness are sufficient to replicate the bulk features of the ferromagnetic part and the semiconducting one around the middle of the slabs. An in-plane lattice parameter of $a = b = 4.15$ Å was chosen in accordance with the surface lattice parameter of InP(111). However the cell parameters are fixed, the atomic coordinates were all allowed to relax from their initial positions. The fully relaxed heterostructures are shown in Fig. 4.1.

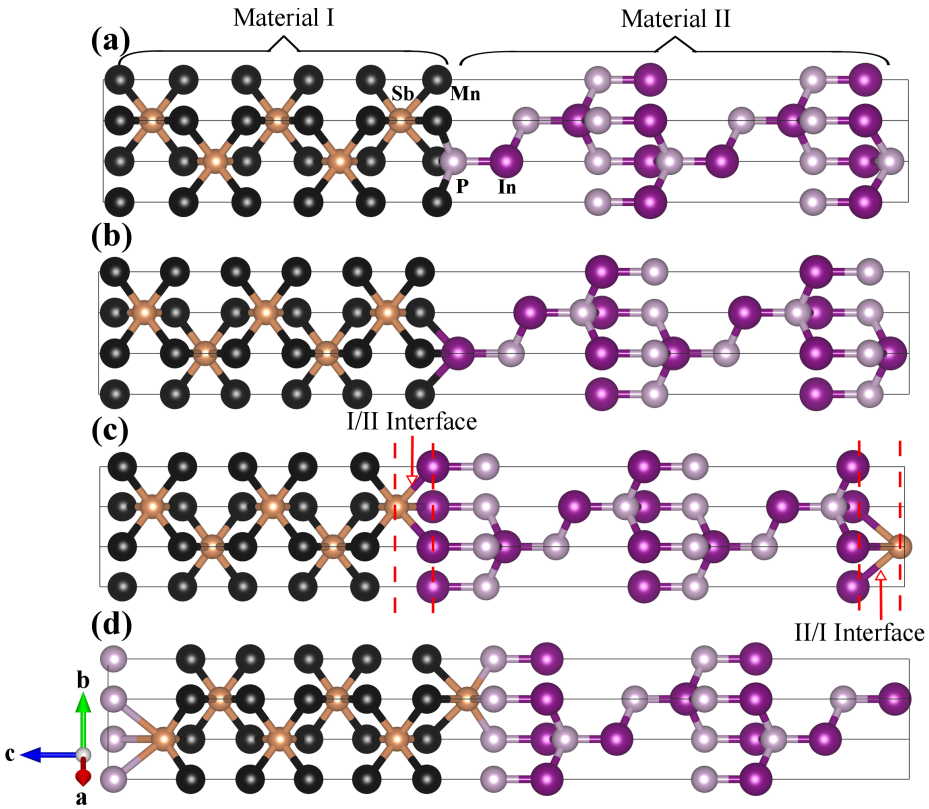

Figure 4.1: Optimized heterostructure, made of 11 atomic layers of n-MnSb(0001) and 13 atomic layers of InP(111). Black (brown) spheres represent Mn (Sb) atoms, while Purple (gray) spheres represent In (P) atoms. The four possible terminations at the interface for this layered structure are: (a) Mn-P, (b) Mn-In, (c) Sb-In and (d) Sb-P termination. N/B: There are two identical interfaces here.

4.2.2 Results

To probe the stability of the n-MnSb(0001)/InP(111) interfaces, total energies of the relaxed interface for the four possible terminations as well as their isolated surface slabs were calculated. The ideal W_R is computed using equation 2.78, here $E_{n-\mathrm{MnSb}(I)}$, $E_{\mathrm{InP}(II)}$, and $E_{n-\mathrm{MnSb/InP}(I/II)}$ are the total energies after relaxation of an isolated n-MnSb(0001) slab, isolated InP(111) slab, and n-MnSb(0001)/InP(111) heterostructures, respectively. The area of each interface is given by $\mathrm{A}_{\mathrm{Interface}}$ and the factor of 2 accounts for the two identical interfaces in the supercell (see the arrows indicating the identical interface

regions between material I and II in figure 4.1(c)).

Shown in table 4.1 are the calculated work of separation and bond lengths for the four possible interface terminations after atomic relaxation. The most probable structural model with interface order Mn-P [Fig.4.1(a)] has the strongest work of separation of 2.80 J/m^2 as well as the shortest bond length of 2.54 Å at the interface. Because this is the most favourable interface, the charge density difference of this interface is given in Fig. 4.2. Portions in red indicate electron enrichment and can be seen midway between the atomic positions, which illustrates a covalently bonded structure [101]. Figure 4.2(a) is a 2D slice of the interface as viewed from the side, while Fig. 4.2(b) cuts through the interfacial bonds when viewed from top.

Table 4.1: The optimized bond length (L) between the interfacial atoms and the calculated work of separation (W) for the various interface ordering studied. (the interface order Mn-P is spin polarized and more stable than others).

Interface termination	**Bond Length (Å)**	**Work of Separation (J/m^2)**
Mn-P	2.54	2.80
Sb-In	3.05	0.64
Sb-P	2.76	1.02
Mn-In	3.08	1.44

Figure 4.3 shows the sum of the partial density of states (PDOS) per atomic layer from the interface up till the third layer into the ferromagnetic material. The spin polarization for the more stable interface structure (Mn-P termination) based on the earlier work of separation analysis [100] was computed using equation 1.2. Spin polarization, which is usually reduced or destroyed at the interfaces of half-metallic FM, is seen to behave differently in this material combination [89, 105]. Presented in Fig. 4.3(a) is the spin-polarized PDOS plot of the Mn-P terminated interface, which shows a gap opening at the Fermi level for the spin down direction. This interface seems to be moving towards a half-metallic behavior and shows 63.9% spin polarization, that is far higher than the bulk *n*-MnSb polarization of 18% and should be very favorable for spin transport applications [6]. Normally interfaces are seen as problematic in half-metallic FM structures, deteriorating or even reversing

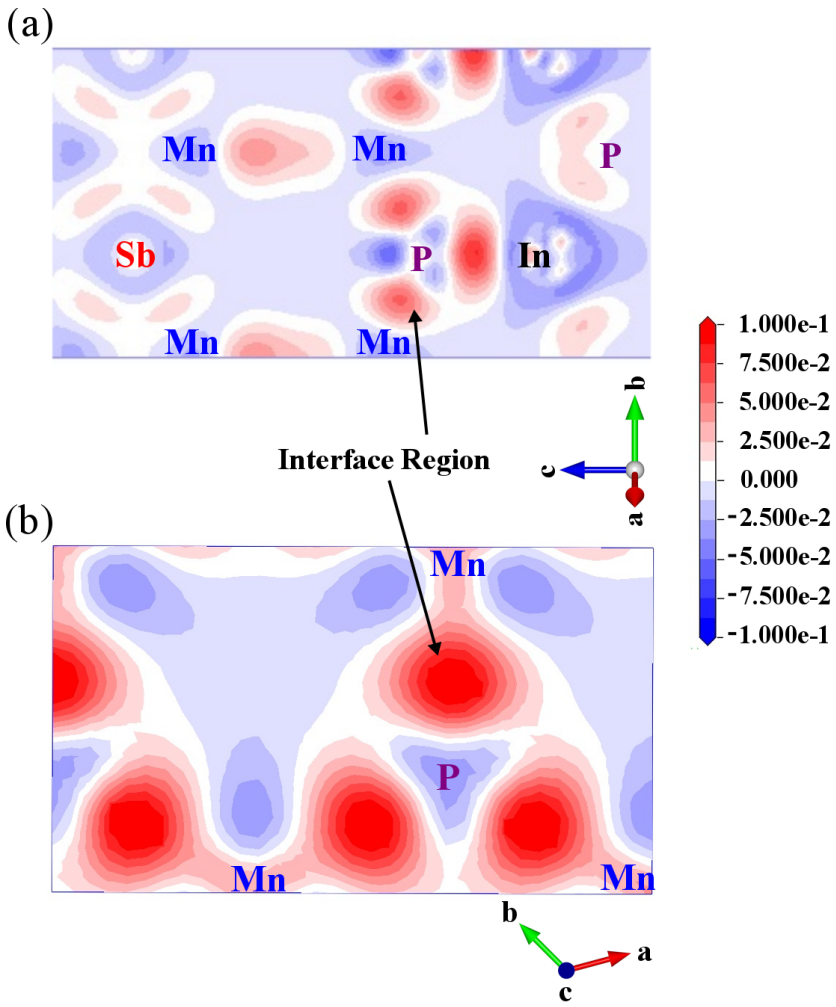

Figure 4.2: Electronic charge density difference of the atoms in Mn-P model sliced at the interface; (a) lateral view, similar to Fig.4.1(a); (b) viewed along the c-axis. Contour maps: electron deficient region in blue, and regions in red is electron enrich. Small changes in electron density is white region. The field values ranges from -0.1 to 0.1 eV/Å^2.

Table 4.2: Spin polarization P and magnetic moments μ in μ_B at the n-MnSb(0001)/InP(111) interfaces for the first two layers of n-MnSb and InP slabs from the interface, for the four terminations. An asterisk (*) denotes atoms in the second atomic layer of InP slab.

Orientation	**P(%)**				μ (μ_B)				
	Mn	Sb	In	P	Mn	Sb	In	P	Total
Mn-P	63.9	58.5	69.8*	87.6	4.50	-0.70	0.02*	-0.44	3.36
Mn-In	-40.2	81.9	-5.2	57.5*	4.72	-0.56	-0.30	0.00*	3.86
Sb-In	-35.0	18.1	-14.9	-50.7*	4.58	-0.26	0.10	0.08*	4.42
Sb-P	-39.9	-26.1	-37.3*	-27.8	4.78	-0.22	0.04*	0.14	4.70

spin polarization, but here it is enhanced. The p orbital contribution from P atom and d orbital from Mn are responsible for the enhanced spin polarization at the Mn-P interface as shown in Fig. 4.4(a) & (b). The tetrahedral arrangement of the Mn and P atoms is another contributing factor. At all four interfaces the ferromagnetism of the n-MnSb slab survives at the interface but with different spin polarizations as depicted in table 4.2. Spin polarization and spin magnetic moment of the atoms which are on the sub-interface layer of the semiconductor slabs are shown with an asterisk (*).

For these interfaces, the Mn atom's total spin moment at the interface depends on the hybridization with the nearest semiconductor atoms. Hence, its total spin moment was computed with that of the neighboring atom of the semiconductor layer. At the Mn-P interface, there is strong hybridization between the Mn d states with the P p states and thus the Mn spin moment is reduced to 3.36 μ_B from the computed value of 3.62 μ_B for bulk n-MnSb. The interfacial P atom shows a negative induced spin moment. This value of total spin moment is not far from the experimental magnetic moment of n-MnSb, 3.57 μ_B [97, 109]. In the case of Mn-In interface, the same situation occurs with In inducing a negative spin moment. But the p-d (In-Mn) hybridization is weaker than the Mn-d-P-p one and the Mn spin moment at the interface is higher here. The induced negative spin moments from P and In atom at the interfaces of Mn-P and Mn-In terminations, respectively, is probably why these terminations have higher work of separations than the other two, which results in a strong p-d hybridization. Similar features have been observed in NiMnSb/InP contacts by Galanakis *et al*, [106].

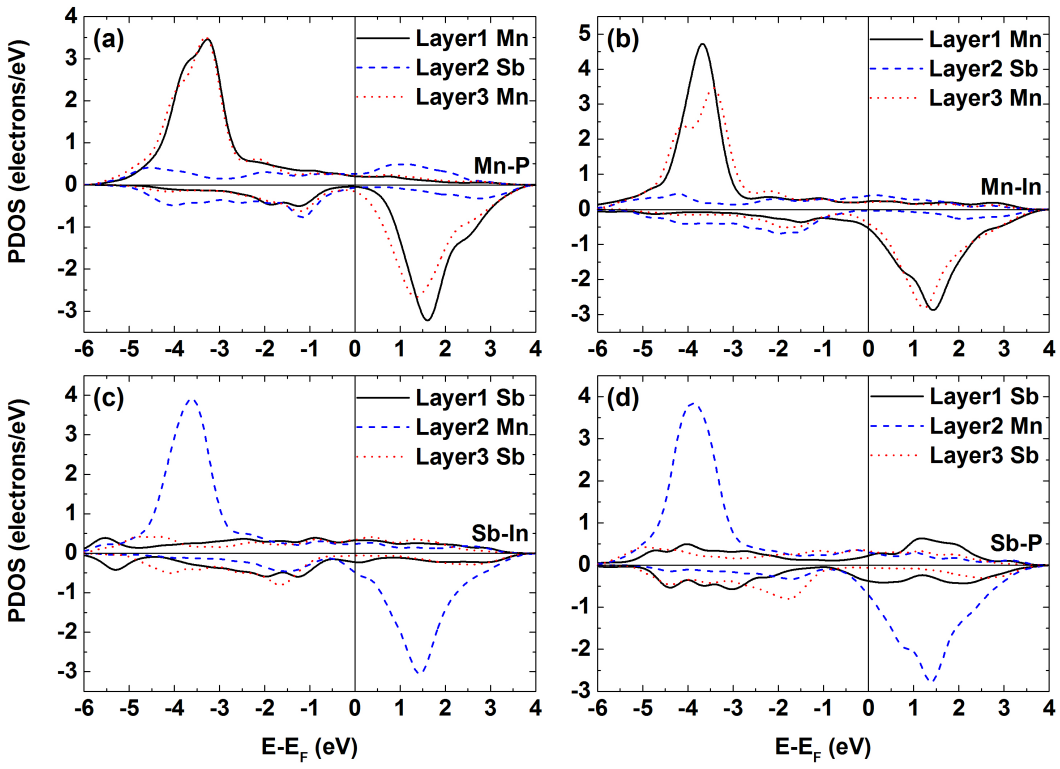

Figure 4.3: Partial density of state plots for the first three layers for the different interface terminations with (a) Mn-P showing an enhanced polarization of 63.9% at the interface. In contrast, (b) Mn-In (c) Sb-In and (d) Sb-P terminations retain their original ferromagnetic behavior.

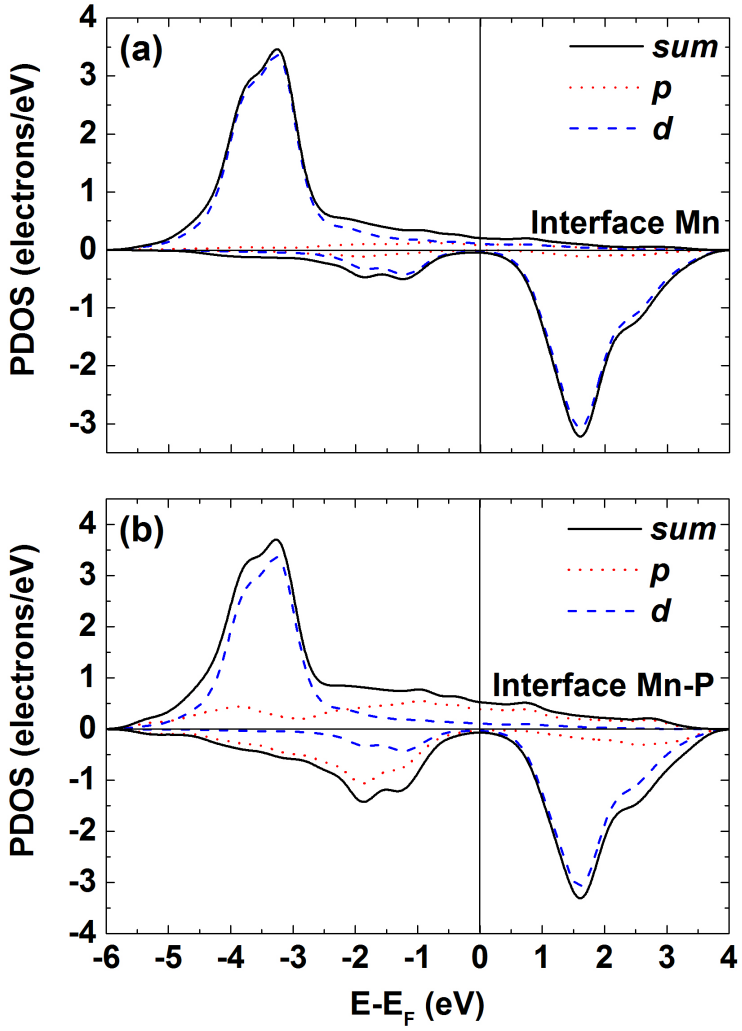

Figure 4.4: Orbital resolved PDOS. (a) first Mn layer at the interface of the Mn-P termination. (b) The Mn-P bi-layer at the interface. Both the p and d orbitals contribute to the polarization.

4.3 n-MnSb(0001)/GaAs(111) superlattices

4.3.1 Model Preparation

The model preparations here is similar to that of the n-MnSb(0001)/InP(111) interfaces and that as discussed earlier in section 2.7. This makes it easier to compare their results. An epitaxial growth model of 11 atomic layers of n-MnSb(0001) on 13 atomic layers of GaAs(111) was made with interfacial

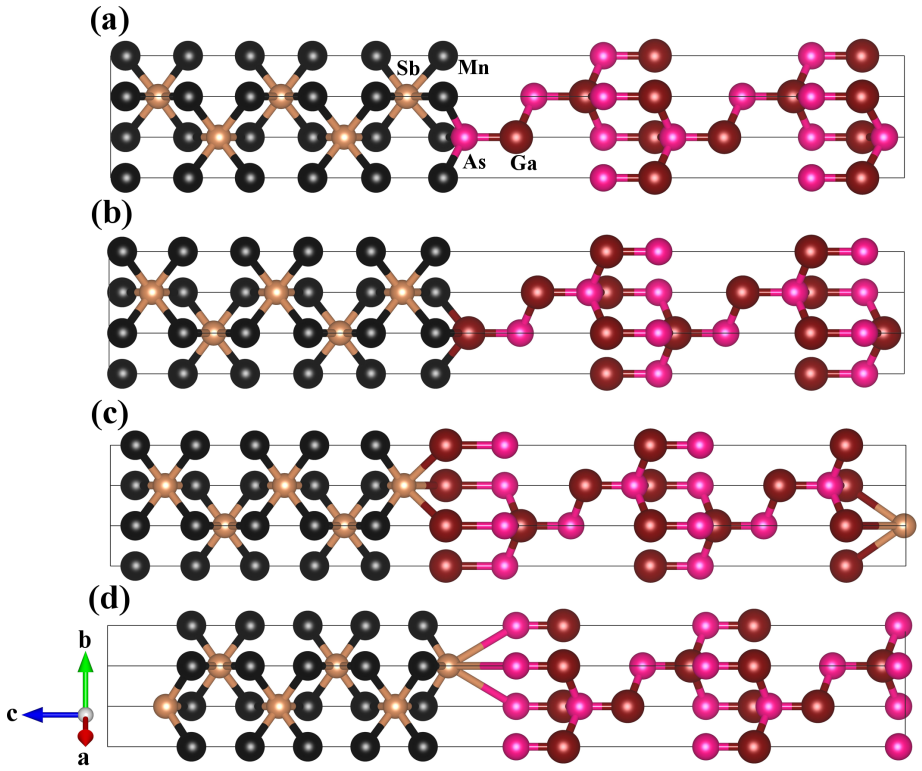

Figure 4.5: Fully relaxed supercell structures, made of 11 atomic layers of n-MnSb(0001) and 13 atomic layers of GaAs(111): (a) Mn-As terminated interface, (b) Mn-Ga terminated interface, (c) Sb-Ga terminated and (d) Sb-As terminated interface. Colour code: Black (brown) spheres represent Mn (Sb) atoms, while Dark brown (pink) spheres represent Ga (As) atoms.

lattice mismatch of 1.0%. The four possible terminations at the interface for this layered structure are: Mn-As, Mn-Ga, Ga-Sb and As-Sb terminations given in Fig. 4.5.

4.3.2 Results

Adhesion strength of the interface atoms between n-MnSb(0001)/GaAs(111) can be described by the work of separation given in equation 2.78. After relaxation of the structure, the calculated W_R and interface bond length for the different terminations are listed in Table 4.3. It can be inferred from the table, that the inter-layer bond length of interface order Mn-As is smaller than the others, while its W_R is the largest, which implies it has the stronger

interfacial atomic binding force and interface stability.

Table 4.3: Interfacial bond length (L) and work of separation (W) for the n-MnSb(0001)/GaAs(111) interfaces.

Interface termination	**Bond Length (Å)**	**Work of Separation (J/m^2)**
Mn-As	2.63	2.02
Ga-Sb	3.23	0.48
Mn-Ga	2.93	1.31
As-Sb	4.23	0.08

The display of the electronic charge density difference for Mn-As termination of the n-MnSb(0001)/GaAs(111) interface shown in Fig. 4.6, helps one to understand what bonding mechanism is partly responsible for the stabilization of the Mn-As terminated interface. From both views, figures 4.6(a) and (b), one can clearly see the charge distributed half way (regions in red) on the bonds between the interfacial atoms, a clear covalent chemical bond formed at the interface.

To analyze the electronic and magnetic properties, I present the layer-resolved partial DOS for the first three layers into the n-MnSb slab of the n-MnSb(0001)/GaAs(111) interfaces in Fig. 4.7. Also, given in table 4.4 are the spin polarization and spin magnetic moments for the first two layers of each slab close to the interfaces. From Fig. 4.7 and Table 4.4 it can be seen that the various interfaces maintain a ferromagnetic behavior at different polarization (spin polarization reversed in some cases). But interestingly, Mn-As termination shows an enhanced polarization of 61.1% at the interface.

Further consideration of the Mn-As terminated interface by analyzing the orbital resolved PDOS shown in Fig. 4.8 for the interface Mn layer and interface Mn-As bilayer, indicates that a strong p-d hybridization exists at the interface, which is due to the As p and Mn d states. The reduction of the Mn total spin moment to 3.26 μ_B in Table 4.4 supports this point, with a negative induced moment on the As atom [106]. The hybridization between the d states of the Mn and the p states of the As atom at the interface is

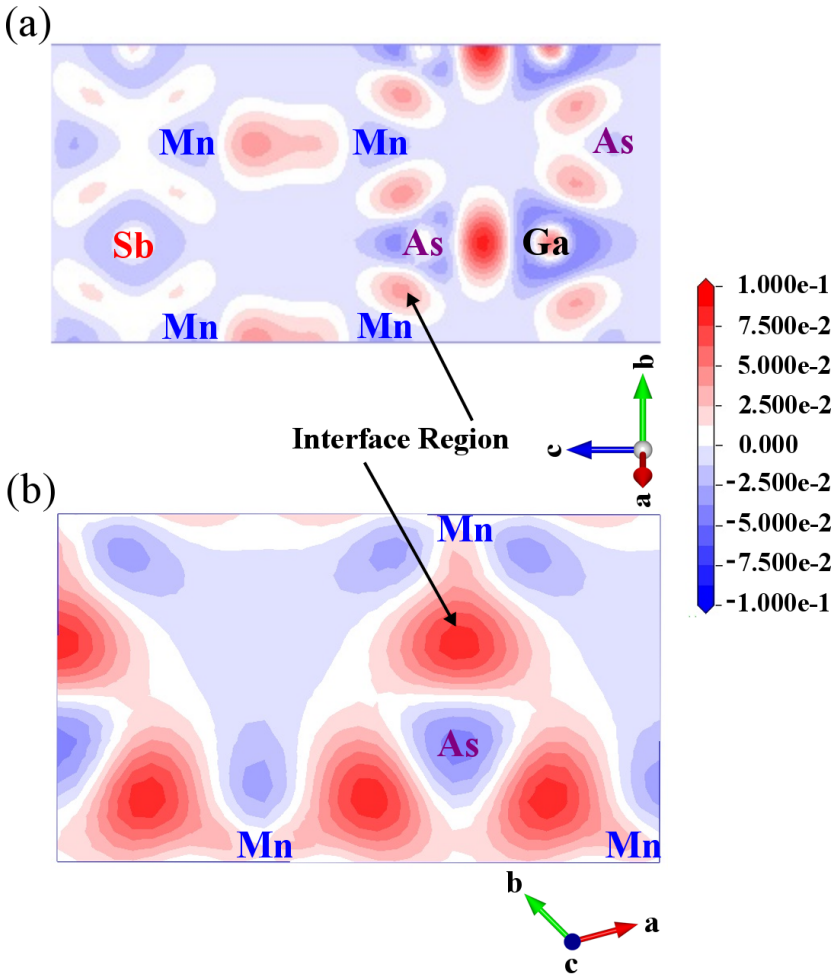

Figure 4.6: Electronic charge density difference of the atoms in Mn-As model sliced at the interface; (a) lateral view and (b) viewed along the c-axis. Contour maps: electron deficient region in blue, and regions in red is electron enrich. Small changes in electron density is white region. The field values ranges from -0.1 to 0.1 e/Å^2

such that the net polarization is 61.1%. Also enhancing the spin polarization at the Mn-As interface is the tetrahedral coordination of the interface atoms. In a similar way, negative spin moment was induced on the Ga atom for the Mn-Ga interface model, but with a weaker hybridization and the next best work of separation (see table 4.3).

Table 4.4: Spin polarization P and magnetic moments μ in μ_B at the n-MnSb(0001)/GaAs(111) interfaces for the first two layers of n-MnSb and GaAs slabs from the interface, for the four terminations. An asterisk (*) denotes atoms in the second atomic layer of GaAs slab.

Orientation	**P(%)**				μ (μ_B)				
	Mn	Sb	Ga	As	Mn	Sb	Ga	As	Total
Mn-As	61.1	58.1	55.5*	78.2	4.50	-0.66	0.02*	-0.58	3.26
Mn-Ga	-30.8	84.4	-12.9	45.6*	4.74	-0.58	-0.32	0.02*	3.84
Sb-Ga	-24.8	17.8	8.3	-29.8*	4.34	-0.52	-0.02	0.00*	3.80
Sb-As	-11.2	-1.5	8.9*	-1.1	4.04	-0.74	-0.02*	0.04	3.34

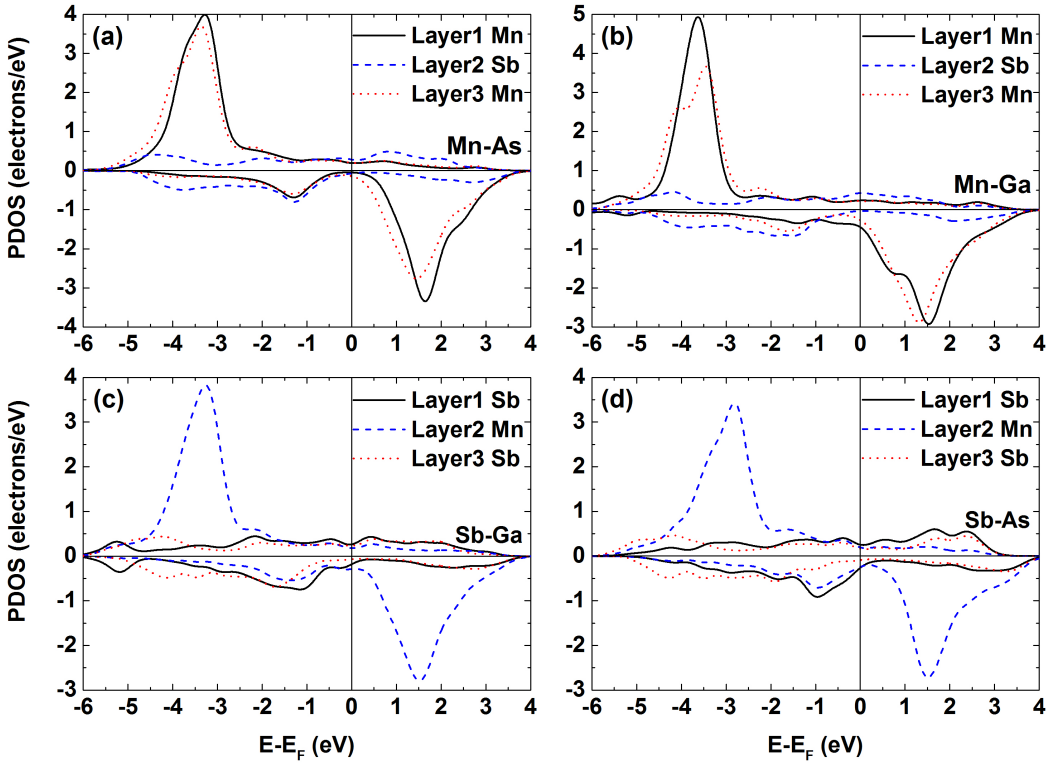

Figure 4.7: Spin-Polarized PDOS for the first three atomic layers of the n-MnSb(0001)/GaAs(111) interfaces for (a) Mn-As (b) Mn-Ga (c) Sb-Ga and (d) Sb-As interface.

4.4 Summary

Overall, I have investigated the structural, electronic and magnetic properties of the (0001) interface between MnSb and the semiconductors InP and GaAs

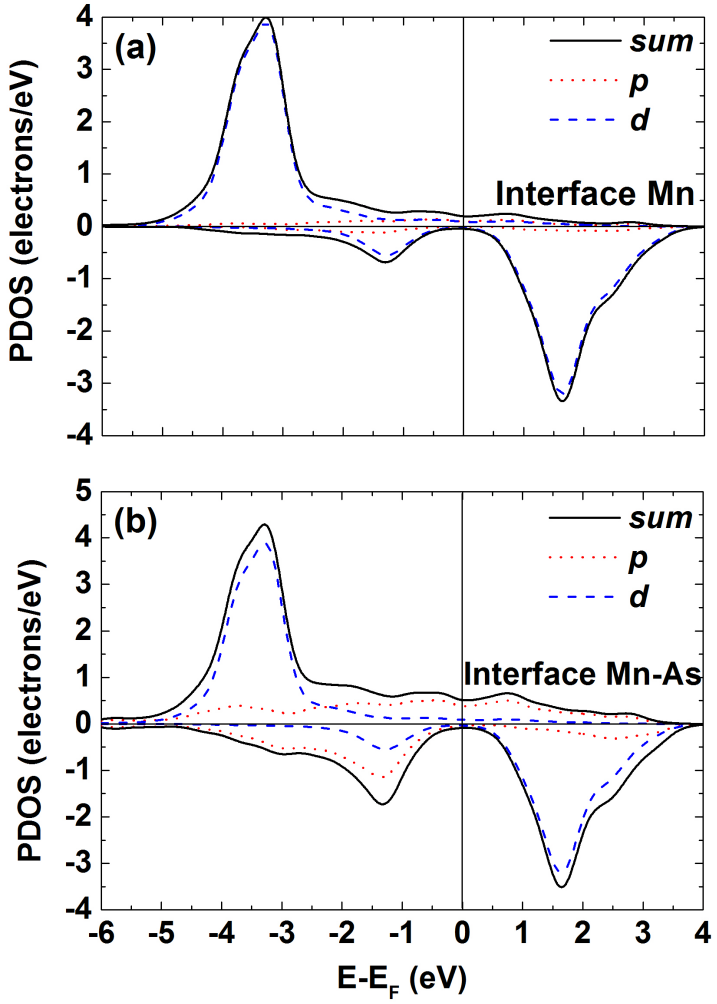

Figure 4.8: Orbital resolved PDOS. Top: first Mn layer at the interface of the Mn-As termination. Bottom: The Mn-As bi-layer at the interface. Both the p and d orbitals contribute to the polarization.

in the (111) direction. The results have shown that the Mn-P interface termination of n-MnSb(0001)/InP(111) is energetically more stable at 2.8 J/m^2 with the shortest bond distance 2.54 Å and shows an enhanced spin polarization of 63.9%. Similarly, the Mn-As interface model was predicted to be stable with high spin polarization of 61.1%. They also show a strong p-d hybridization. These spin polarizations are far higher than the bulk polarization of 18% and should be very favorable for spin transport applications. Thus controlling the growth conditions in an experiment may lead to further stabilization

of the n-MnSb(0001)/InP(111) and n-MnSb(0001)/GaAs(111) interface. The other sequences of the interface layers are ferromagnetic with lower or negative polarization. Electronic transport properties will be calculated on the favorable structure to determine its suitability for a current perpendicular to plane device model.

Chapter 5

The Sb(0001)/*n*-MnSb(0001) superlattice

5.1 Introduction

Antimony(Sb) is a non-magnetic semimetal that forms in the trigonal crystal structure (space group R$\bar{3}$m No. 166) under ambient condition. In this structure layers of closed, irregular, six-membered rings of Sb are formed as shown in figure 5.1. An irregular octahedral complex is formed by the nearest and next-nearest neighbors, with the atoms within a bilayer being closer together than with the atoms in the other bilayers. The Sb-Sb distance within the bilayer is 2.908 Å, while the Sb-Sb distance between two bilayers is at least 3.355 Å [110]. This arrangement of Sb atoms yields an hexagonal form of the crystal structure. The element antimony can be used for producing III-V antimony-based semiconductor materials, optoelectronic devices and high speed transistors [111, 112]. It is usually used as a dopant or an adsorbate to improve the properties of other compounds, such as tin oxide, magnesium silicide, nickel manganese antimonide and manganese antimonide [113]. For instance, doping magnesium silicide with Sb increases the thermoelectric conversion efficiency, which is useful for power generating thermoelectric devices. Sb doped tin oxide thin films have exceptional electrical conductivity and optical properties, which makes them suitable for hetero-junction solar cells, and displays application [114, 115, 116, 117]. In a recent study in G. R. Bell's

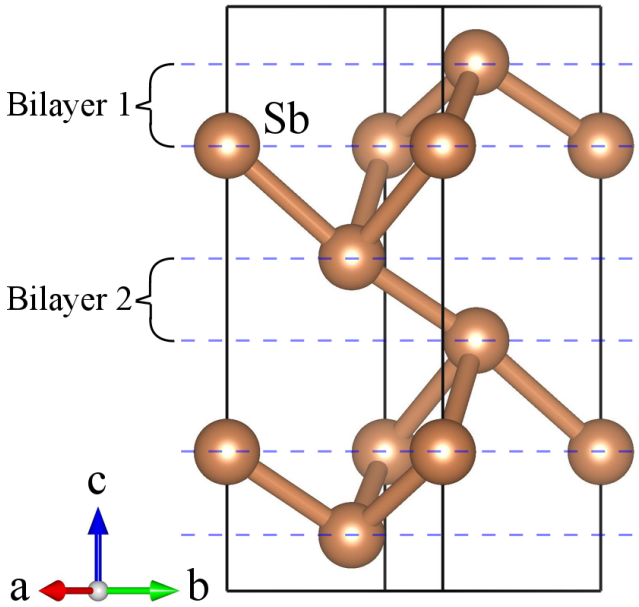

Figure 5.1: Crystal structure of trigonal Sb. Atoms in each bilayer are slightly close together than with those in the adjacent bilayers. This is in the hexagonal Sb structure.

group, Dr. C. W. Burrows grew thin films of Sb on MnSb as a capping layer using a molecular beam epitaxy (MBE) system [38, 118]. The capping layer was used to prevent oxidation of the MnSb film below (see figure 5.2). A GaAs substrate has been used in the Sb/MnSb spin valve structure: Sb(0001)/MnSb(0001)/Sb(0001)/MnSb(0001)/GaAs(111)A and the growth conditions are given in table 5.1. After the growth process X-ray diffraction (XRD) data and a reflection high-energy electron diffraction (RHEED) images were taken.

Table 5.1: Growth conditions for Sb/MnSb heterostructures. The Sb cap layer was deposited for 90 s while cooling from 250 to 230 $°C$. And the flux ($J_{Sb/Mn}$) was not measured between the Sb cap and MnSb(2) layer.

Layer	$\mathbf{T}_{sub}(°C)$	$\mathbf{J}_{Sb/Mn}$	**Growth time**
MnSb (1)	350/415	6.53	18 m 11 s
Sb interlayer	250	-	50 s
MnSb (2)	300/410	Cell temps as MnSb(1)	9 m 6 s
Sb cap	250 ->230	-	1 m 30 s

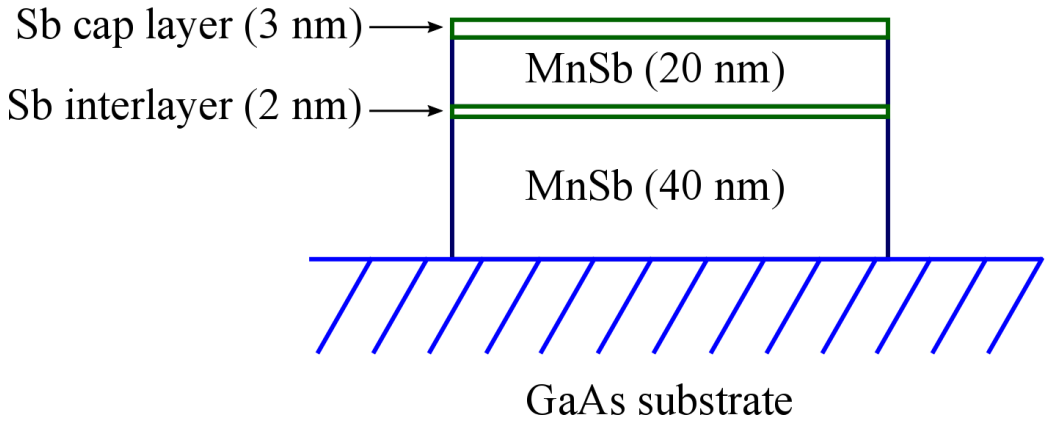

Figure 5.2: Simple schematic highlighting structure of the Sb/MnSb spin valve structure discussed in the text.

Throughout growth of the spin valve structure, RHEED patterns were obtained. These were collected for each of the layers in the structure at the end of their respective growth stages. The RHEED images given in figure 5.3 shows sharp streaks throughout (indicating good crystallinity) with distinct reconstructions between the MnSb and Sb layers. Lattice parameters from the RHEED images differ between MnSb and Sb layers, and are consistent with the bulk values as given in table 5.2. The lattice parameters derived from RHEED measurements suggest that the MnSb films are slightly strained by an amount of 0.04 Å (likely due to residual strain in these relatively thin layers) while the Sb layers are more heavily strained (by about 0.10 Å) to the MnSb due to their very low thicknesses. The good crystal quality of the MnSb and Sb layers was confirmed through XRD, shown in figure 5.4, and shows a symmetric MnSb peak while the Sb cap has broad peaks due to finite size broadening, but the peaks remain reasonably symmetric. The lattice parameter of the thin Sb layer was partially strained to that of MnSb and its measured c lattice parameter is 11.479±0.012 Å, which is comparable to the bulk value of 11.273 Å [119, 120]. Note that the XRD is from a MnSb/Sb cap sample (not the multilayer) but should be very similar. The XRD data and RHEED images suggest that the Sb caps are generally good and high quality films of Sb can be grown on MnSb. These results are consistent with previous Sb/MnSb growth studies [38, 12, 121].

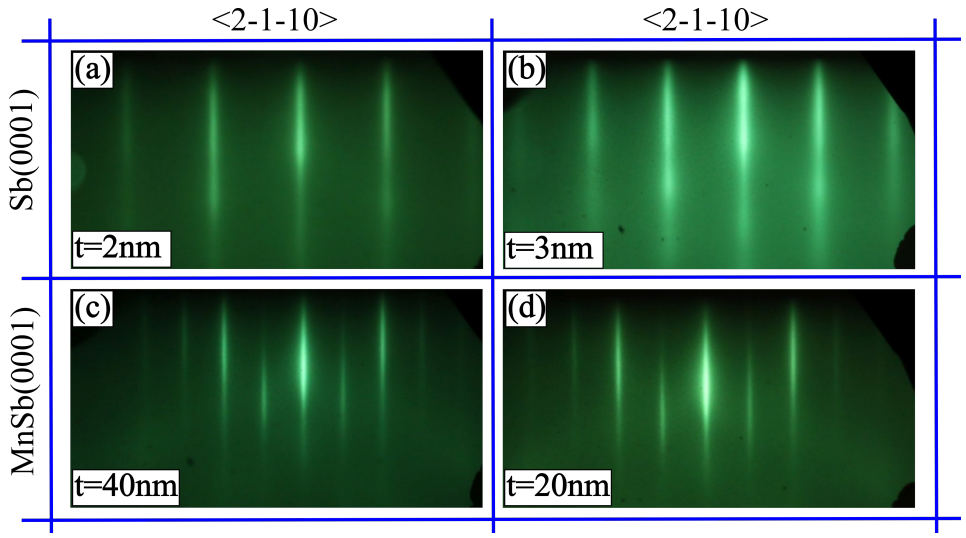

Figure 5.3: RHEED images of the different layers of the Sb/MnSb heterostructure with the thickness(t) per layer indicated and the growth direction shown. The image for substrate is not given here.

Motivated by the experimental results from the use of Sb caps to prevent oxidation, which shows good crystal quality (from XRD data) that can be use in spin valve type structures as well as a RHEED pattern that looks promising in growth, and preliminary studies of ultra-thin films of Sb shows interesting transport properties at 300 K, such as a high mobility. I studied the structural and electronic properties of Sb/MnSb(0001) interfaces using a DFT approach.

Table 5.2: Measured a lattice parameters of the films grown compared with their bulk values. The films a lattice parameters are computed from GaAs scaling.

Material	**Bulk *a* lattice parameter (Å)**	**Films *a* lattice parameter (Å)**
GaAs	3.997	3.997
MnSb	4.128	4.169±0.129
Sb	4.308	4.216±0.09

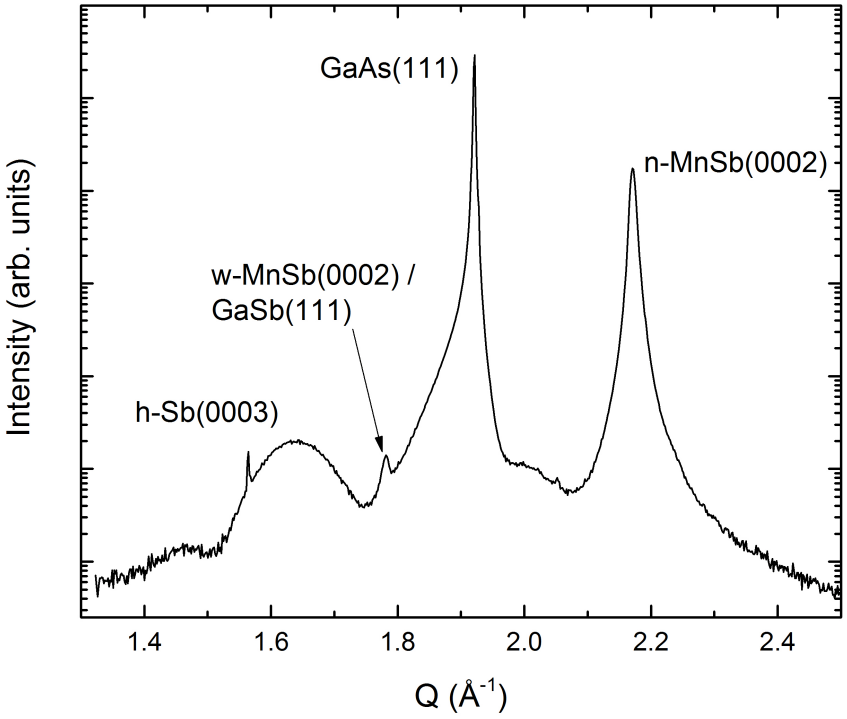

Figure 5.4: XRD data for the Sb-capped MnSb sample showing the expected peaks from the substrate, *n*-MnSb film and Sb cap.

5.2 Models and Computational Method

Here I have studied the structural and electronic properties of the interface between Sb(0001) and nMnSb(0001) using ultra-soft pseudopotentials (a CASTEP on the fly generated USP). First, I optimized the bulk Sb structure given in figure 5.1 with the PBE functional and a cutoff energy of 400 eV. A Monkhorst Pack **K**-point grid of 7×7×5 have been used. For the interface, a PBE+U (U = 1.0 eV on Mn) exchange correlation functional was used with cutoff energy of 400 eV and Monkhorst Pack **K**-point grid of 7×7×1. The Sb(0001)/*n*-MnSb(0001) interfaces were made as a heterostructure, in which a slab of 13 atomic layers of Sb(0001) is placed on a 13-layer *n*-MnSb(0001) slab. Their in-plane lattice mismatch is 3.65% and the surface lattice of *n*-MnSb was adopted for the supercell geometry lateral lattice. To ascertain which interfacial geometry has promising features, the two possible interface terminations were considered, i.e Mn-Sb and Sb-Sb termination, as shown in

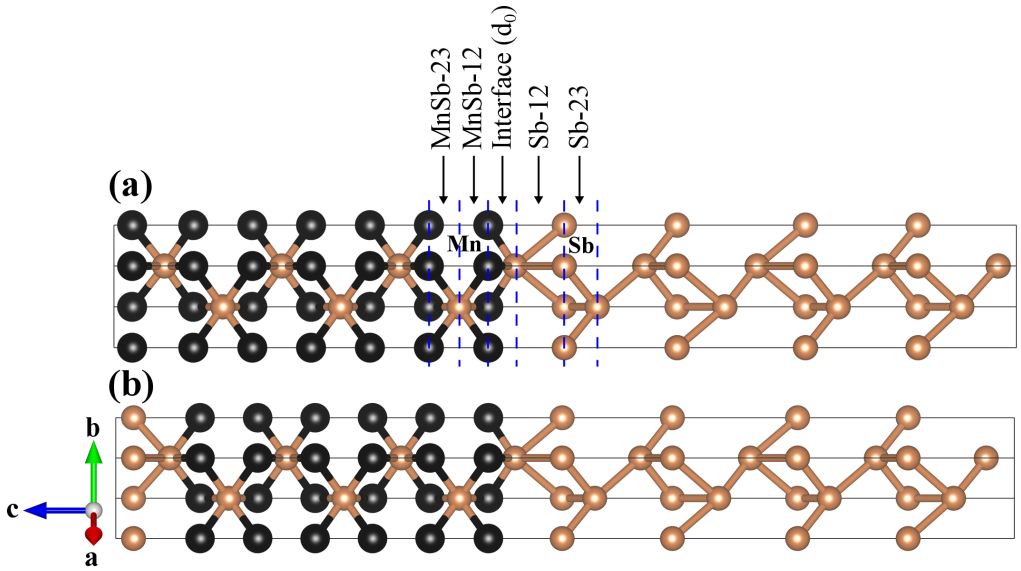

Figure 5.5: Superlattice geometry for Sb(0001)/n-MnSb(0001) interfaces: (a) Mn-Sb and (b) Sb-Sb termination. Black (brown) spheres represent Mn (Sb) atoms. d_0 is the interface separation between Sb(0001) and MnSb(0001) slabs. MnSb-12 is the interlayer distance between layer 1 and 2 of the MnSb(0001) slab, while MnSb-23 is the interlayer distance between layer 2 and 3. Similarly, Sb-12 and Sb-23 represent the interlayer distances in the Sb(0001) slab.

Fig. 5.5. Structural and electronic properties were then calculated for these, after full atomic relaxation.

5.3 Results

Lattice parameters of $a = 4.37$ Å and $c = 11.39$ Å were obtained after optimization of the bulk Sb structure shown in figure 5.1. These are similar to the lattice parameters ($a = 4.22$ Å and $c = 11.48$ Å) obtained in the Sb thin film growth studies in figure 5.3 and previous experimental results of $a = 4.31$ Å and $c = 11.27$ Å [119, 120]. Sb is a paramagnetic material with zero band gap as can be seen in the electronic band structure and DOS plots given in figure 5.6, where bands crossing the Fermi level can be seen near A and L in the band structure plot (figure 5.6 (b)).

Work of separations W_R given in table 5.3 were calculated in order to investigate the effect of lattice relaxation on bonding at the Sb(0001)/n-

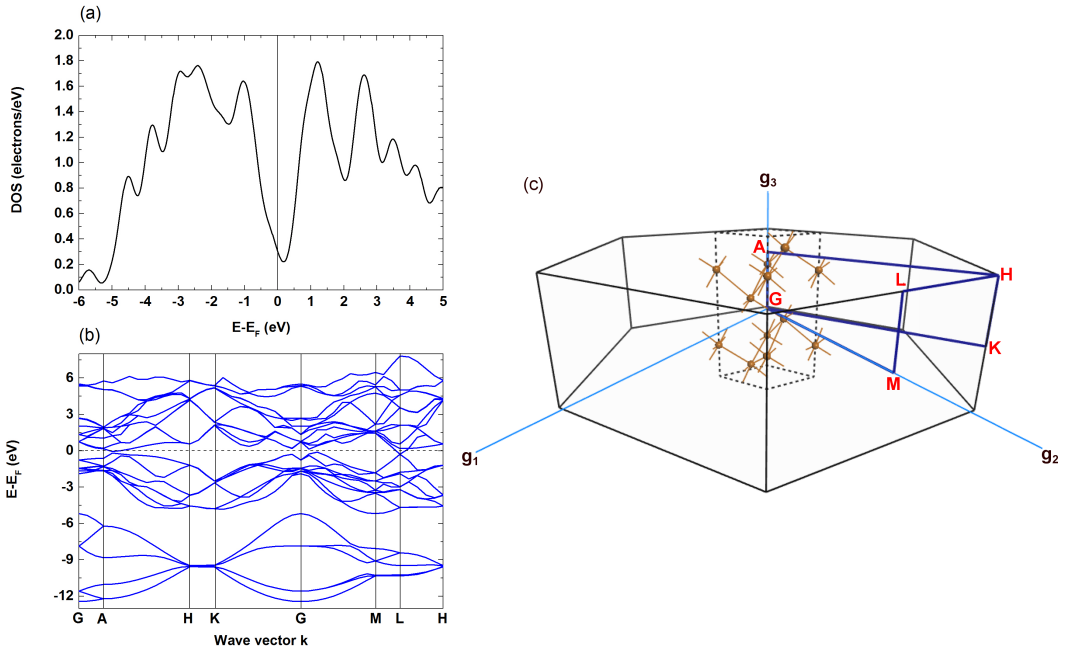

Figure 5.6: The semimetallic behaviour of Sb, indicated by a small density of state at the Fermi level and it has no band gap. (a) DOS, (b) band structure of Sb and (c) Brillouin zone of hexagonal Sb showing its crystalline structure and the wave vectors.

MnSb(0001) interface. From this table, one can find that the highest W is 1.29 J/m^2 for the Mn-Sb interface order, which also has the smallest interfacial bond distance of 2.77 Å. This is an indication that, structurally Sb(0001)/*n*-MnSb(0001) layered growth will prefer to form with Mn-Sb bonding at the interface over Sb-Sb. In Fig. 5.7, the contour map for the charge density difference of the Mn-Sb stacking sequence is shown and the electron density accumulates somewhat close to the Mn atom. This is an indication of a bonding character that is somewhere between ionic and covalent. The white area in figure 5.7(b) is a vacancy site with no interaction.

After geometry optimization is performed, the degree of relaxation of the first two interlayer distances of the MnSb and Sb slabs, as well as the interfacial separation d_0 for the two Sb/*n*-MnSb(0001) interfaces are shown in table 5.4 (the interlayer distance notations used are illustrated in figure 5.5). Before atomic relaxation, the first two interface layers on *n*-MnSb(0001) surface slab (MnSb-12 and MnSb-23) have interlayer separations of 1.44 Å and

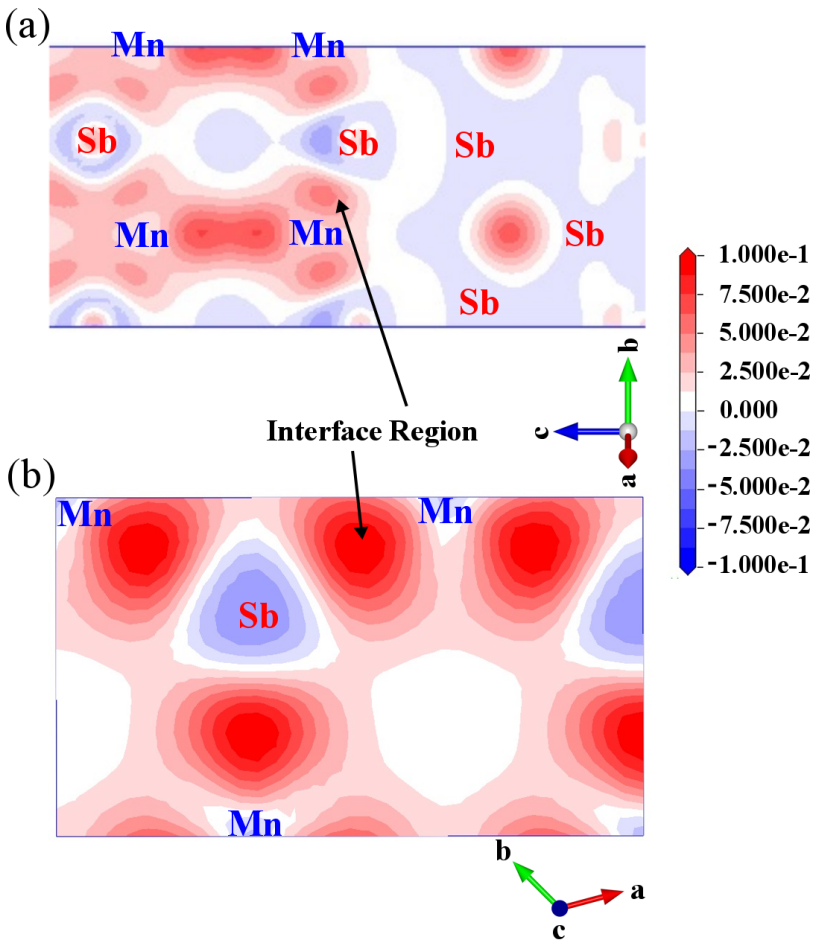

Figure 5.7: Electronic charge density difference of the atoms in Mn-Sb model sliced at the interface; (a) lateral view and (b) viewed along the c-axis. Contour maps: electron deficient region in blue, and regions in red is electron enrich. Small changes in electron density is white region. The field values ranges from -0.1 to 0.1 e/Å^2.

Table 5.3: The optimized bond length (L) between the interfacial atoms, the calculated work of separation (W_R) for the various interface ordering studied and there average magnetic moments.

Interface termination	**Bond Length (Å)**	**Work of Separation (J/m^2)**	**Magnetic moment (μ_B)**
Mn-Sb	2.77	1.29	3.94
Sb-Sb	3.00	0.45	3.88

Table 5.4: Interfacial separation for the n-MnSb/Sb(0001) interfaces, and given in brackets are changes in percentage of the interlayers.

Interlayer	**Interlayer Distance (Å)**	
	Mn-Sb	Sb-Sb
MnSb-23	1.53 (+6.25%)	1.49 (+3.47%)
MnSb-12	1.48 (+2.78%)	1.37 (-4.86%)
Interface	1.36	2.44
Sb-12	2.50 (+55.28%)	1.68 (-21.86%)
Sb-23	1.67 (-22.33%)	2.36 (+46.58%)

1.44 Å, whereas those of Sb-12 and Sb-23 are 1.61 Å and 2.15 Å respectively. From table 5.4, note that the changes in the interlayer distance for Sb slabs is far greater than that of n-MnSb because its in-plane lattice was compressed to match the surface lattice of n-MnSb. For the Mn-Sb interface model, the neighboring layers of the interface relax towards Sb and the atoms on both sides of the interface move closer, thus reducing the interlayer separation distance. On the other hand, the relaxed atomic coordinates on both sides of the Sb-Sb interface, move away from each other and the interlayer distance increases. These data supports the fact the interface with Mn-Sb termination is energetically more favourable than the Sb-Sb one.

Figure 5.8, shows the total PDOS and orbital resolved DOS plots for the Sb(0001)/n-MnSb(0001) models, it can be seen that both systems show ferromagnetic behavior. From figure 5.8(d), the sum of the DOS (black curve) has contributions from the p states of Sb and the d states of Mn, which is an indication of a p-d hybridization taking place at the Mn-Sb interface order. The polarization here has reversed from a bulk polarization of about 18 % to

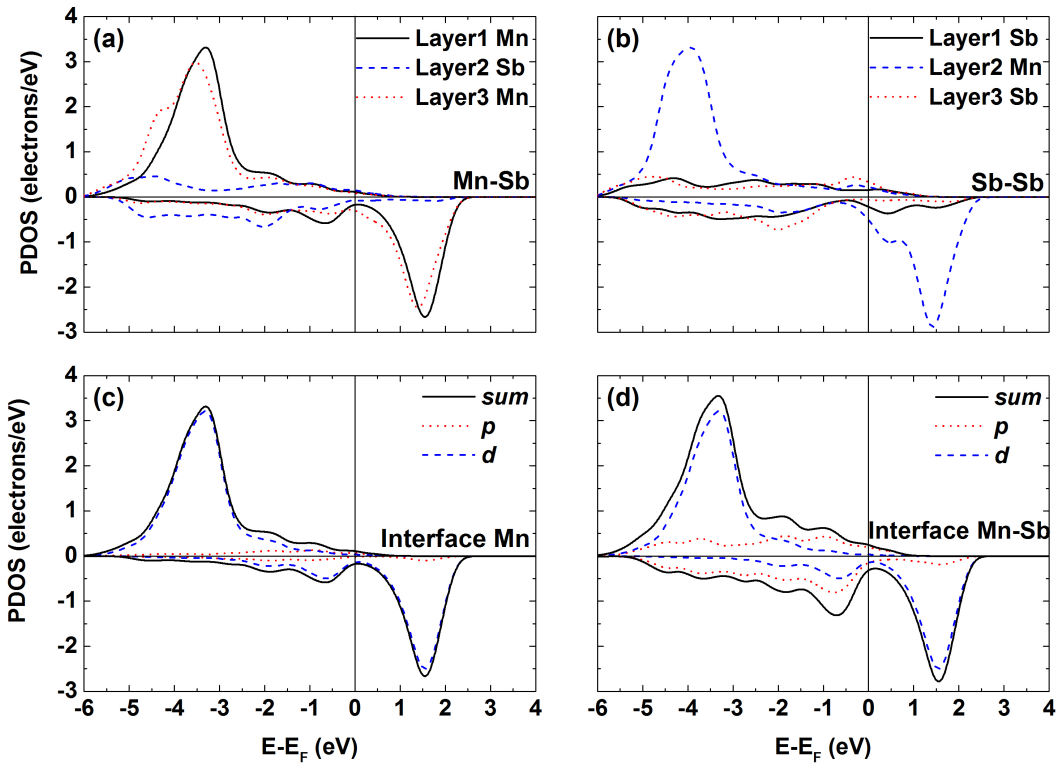

Figure 5.8: Partial density of state plots for the first three layers for the different interface order with (a) Mn-Sb and (b) Sb-Sb termination. While (c) and (d) are the orbital resolved dos for the interface Mn layer and Mn-Sb bi-layer respectively.

-57.7 % at the interface, then to -51.7 % on the first layer of Sb(0001) slab. For the magnetic property of the interfacial model Mn-Sb, Mn is seen to have an increased average magnetic moment of 3.94 μ_B as shown in table 5.3.

5.4 Summary

We have investigated the interface structural and electronic properties of the (0001) direction between MnSb and an Sb capping layer. The Sb(0001)/*n*-MnSb interfaces are ferromagnetic with lower or reversed polarization. The results from structural properties give an indication of the Sb cap layer used to prevent oxidation of the Mn is ready to bond with the *n*-MnSb. This is an indication of good structural compatibility (growth), which agrees with the RHEED and XRD results. Expected semimetallic behaviour in bulk Sb was observed. In the interfacial layers, the Mn-Sb interface with the highest work of separation is expected to be more stable than Sb-Sb interface. Ionic-covalent bond mix at the Mn-Sb interface is given by the charge localized on Mn. The magnetism of *n*-MnSb given by the spin moment 3.94 μ_B was not destroyed at the interface with the paramagnet Sb. Instead, the moment on Mn atom was boosted and polarization at the interface was reversed to -57.7% from 18% in the bulk. Such heterostructures could potentially be useful in transport applications of spin devices.

Chapter 6

NiO/MgO heterostructures

6.1 Introduction

Recently, an increasing number of studies have been carried out on the binary metal oxide, NiO, due to its interestingly diverse properties and promising technological applications. NiO, which is a wide energy gap material in simple cubic rock salt structure (see figure 6.1) has attracted lots of attention for applications in resistance random access memory due to the resistive switching effect it possess [122, 123, 124, 125, 126, 127, 128]. It has been shown to maintain an efficient spin-current injection at high temperature in magnetic heterostructures [129]. Improvements in the power conversion efficiency of organic photovoltaic cells have been achieved using interfacial NiO layer [122]. Another application for NiO, is catalytic support in spintronic devices [130, 131]. This antiferromagnetic material can also exhibit half-metallicity in some conditions, such as biaxial strain or induced cation vacancies [132, 133, 63]. Insulating antiferromagnets such as NiO, may be useful in spin interconnects and magnonics [63, 17, 134]. NiO is an antiferromagnetic insulator with an optical band gap of ≈3.6 eV and Néel temperature (T_N) of 525 K [122]. It crystallizes in the simple cubic rocksalt (B1) structure of space group $Fm\bar{3}m$ with number 225 as shown in figure 6.1.

Manipulating the antiferromagnetic moments of antiferromagnetic materials is very difficult due to their insensitivity to magnetic fields. For reorientation of the antiferromagnetic moments a non-magnetic polarizer (e.g MgO) is now being used instead of a ferromagnetic polarizer in a stacking

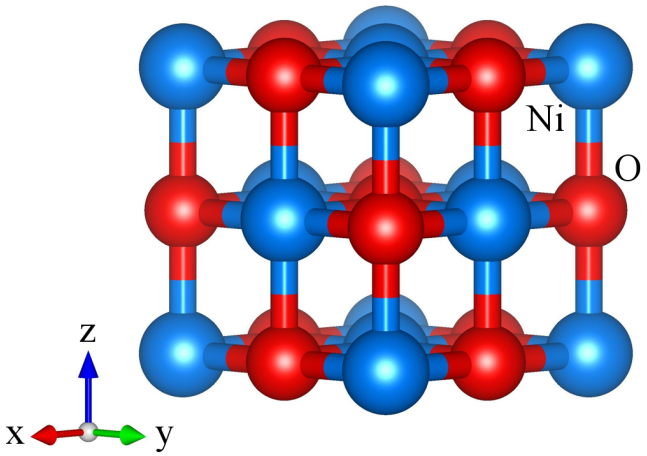

Figure 6.1: Rock salt crystal structure of NiO in space group $Fm\bar{3}m$ (no. 225). Blue (red) spheres represents Ni (O) atoms.

geometry. The non-magnetic conductor/antiferromagnetic bilayer becomes an efficient spin injector due to the presence of spin Hall effect (SHE) in the non-magnetic layer [17, 135, 136]. Still, this SHE device structure is limited by the spin torques sensitiveness to the interface quality of the non-magnet/antiferromagnet bilayer, which loses efficiency for antiferromagetic layer thicknesses beyond the nanometer scale. MgO is a widely used substrate for growing metallic thin films and currently is being used for the growth of magnetic oxides layers [137, 138, 139, 140]. MgO similarly crystallizes in the rocksalt structure and have a wide band gap of ≈7.8 eV. It is a II-VI compound that forms an ionic bond between magnesium and oxygen atom [141].

In this study, first-principles calculations of half-metallic/non-magnetic polarizer interfaces are carried out to determine a suitable structure for efficient spin transmission. The interfaces studied are NiO(111)/MgO(111), NiO(001)/MgO(001) and NiO(110)/MgO(110). The DFT calculations were performed using plane-wave pseudopotential method. To account for the magnetic nature of NiO, spin polarized calculations have been carried out using the GGA+U method with an optimal U value of 6.5 eV. This value of Hubbard U parameter can give an accurate description of the electronic structure of the NiO slab, when used for Ni $3d$ electrons and closely agrees with previous works [142, 143, 144, 145]. The PBE exchange-correlation functional was

Table 6.1: Comparison of the computed lattice parameters and band gap for MgO and NiO with previous works.

Species	Lattice Parameter (Å)			Band Gap (eV)		
	This Work	Experiment	Other Calculations	This Work	Experiment	Other Calculations
MgO	4.25	4.21	4.22 [141], 4.25 [147]	4.51	7.83	-
NiO	4.50	4.17	4.19 [63], 4.44 [132]	1.41	3.60 [148]	3.10 [63], 1.2 [148]

employed with Koelling-Harmon relativistic treatment for the self-consistent field calculations [146, 57]. The plane wave basis set energy cut-off was set to 500 eV, while the Brillouin zone was sampled within 6×6×6 K-point grid for bulk NiO and 6×6×1 k-point grid for the NiO/MgO interfaces. The BFGS optimization method was used to perform full structural optimization until the forces on all the atoms were less than 0.03 eV/Å.

Bulk NiO and MgO structures were fully optimized in a geometrical optimization calculation using similar computational details given above, with the exception of a non-spin polarized simulation was done for MgO. Table 6.1 summarises and compare the lattice parameters and band gaps obtained from this calculation with previous works. The slab layers of NiO and MgO surfaces are 5.6% lattice mismatched, with calculated bulk lattice parameters of 4.50 Å and 4.25 Å, respectively. A lattice strain of NiO from an experimental value of 4.17 Å to 4.50 Å after optimization, results in a half metallic bulk NiO with an integer moment of 2.00 μ_B. This is illustrated by the DOS plot in figure 6.2.

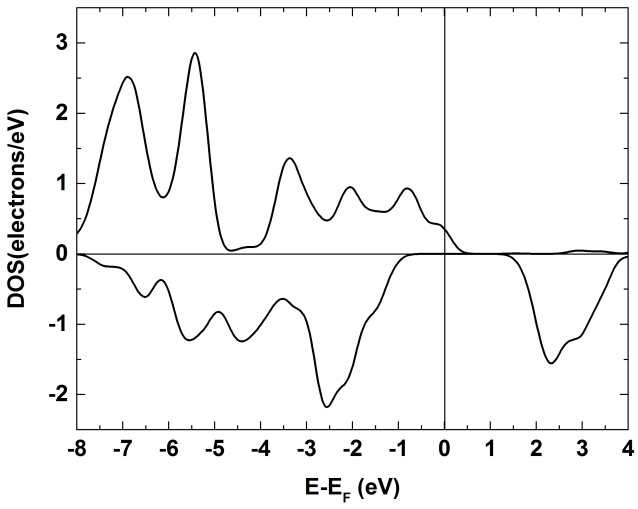

Figure 6.2: DOS for a half-metallic NiO in the B1 structure.

6.2 NiO/MgO(111)

6.2.1 Models and Computational Method

In the current study, I choose thirteen NiO(111) and eleven MgO(111) layers to model the NiO/MgO(111) slab geometry shown in Fig 6.3. These number of layers are sufficient to reproduce the respective bulk properties at the centre of NiO(111) and MgO(111) slabs. I constructed the interface models in such a way that the NiO(111) layers are stretched to the in-plane lattice constant of MgO(111) layer to form a coherent interface.

6.2.2 Results

The adhesion strength of an interface can be computed by the work of separation (W_R) expression given in equation (2.78), using the individual slab energies for NiO (E_{NiO}) and MgO (E_{MgO}) with the total energy of the interface 13NiO/11MgO(111) ($E_{interface}$) as well as the interface area A. The calculated values of W_R, interlayer distance d and interface bond length L for the four possible ways of terminating the NiO/MgO(111) interfaces are summarized in table 6.2. The Ni-O and O-Mg interface terminations show higher W_R than Ni-Mg and O-O interfaces, as anticipated. I found the Ni-O interface

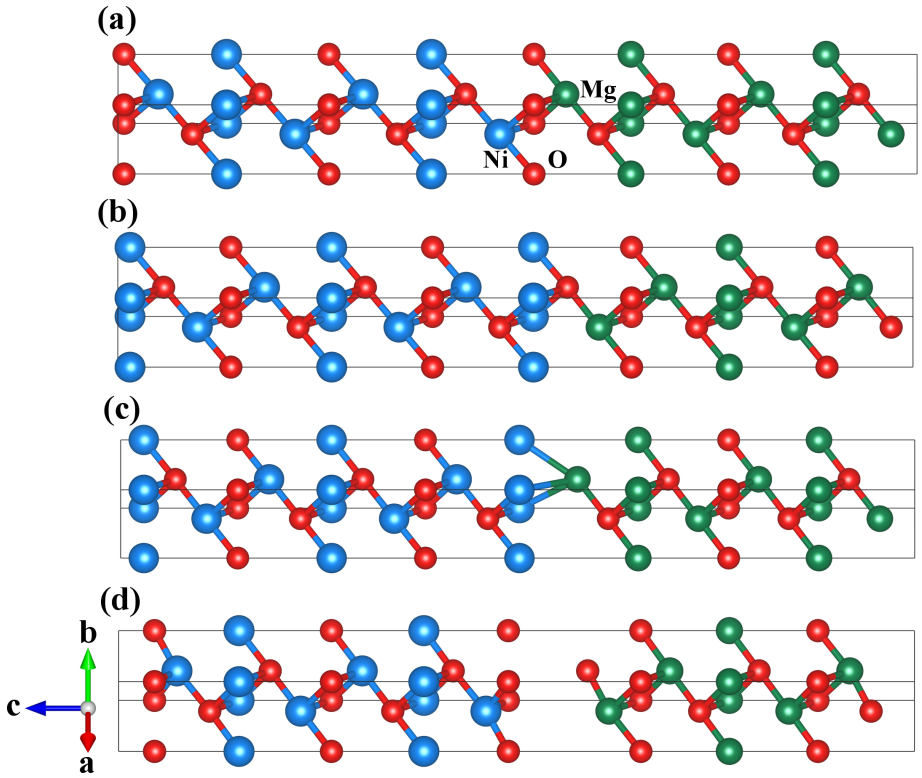

Figure 6.3: Optimized interface terminations of NiO/MgO(111) with (a) Mg-O, (b) Ni-O (c) Mg-Ni and (d) O-O.

Table 6.2: The calculated work of separation (W_R) for the various interface ordering studied, there optimized bond length (L) between the interfacial atoms, and the interlayer distances (d).

Interface Termination	**Work of Separation (J/m^2)**	**Interlayer Distance (Å)**	**Interfacial Bond Length (Å)**
Ni-O	6.84	1.41	2.23
Ni-Mg	2.33	2.44	2.99
O-Mg	6.57	1.33	2.17
O-O	0.74	3.28	3.70

model with W_R of 6.84 J/m^2 to be energetically most favorable, while the O-O terminated interface is the most unfavorable. In all cases there is attraction from both oxide materials at the interfaces, except in the case of O-O interface order, where repulsion between NiO and MgO slabs is seen. This led

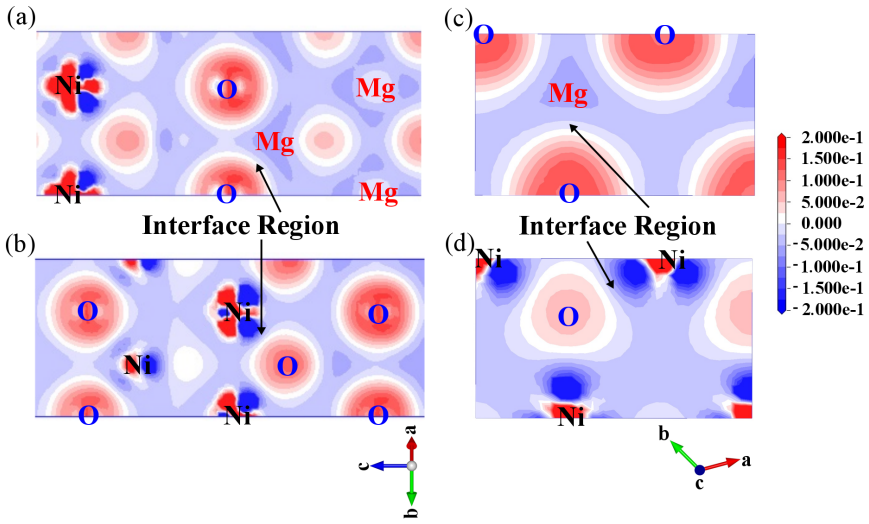

Figure 6.4: Electronic charge density difference of the atoms in Mg-O and Ni-O models sliced at the interface edge; (a) lateral view of O-Mg, (b) lateral view of Ni-O (c) O-Mg viewed along the c-axis and (d) Ni-O viewed from the top. Contour maps: electron deficient region in blue, and electron rich regions in red. Small changes in electron density is white region. The field values ranges from -0.2 to 0.2 eV/Å^2.

to reduced interlayer distances for the Ni-O, O-Mg and Ni-Mg terminations, as their interface layers relaxed towards each other. The minimum interface bond length of 2.17 Å was observed for the O-Mg interface, with 6.57 J/m^2 W_R that closely matches the energetically favorable Ni-O interface. In general bond length decreases with increasing W_R, because, as the molecules from a substrate and thin film materials approach each other, the interfacial bond distance decreases due to attractive forces and the reversible work necessary to separate the interface between two materials increases. Repulsive and van der Waals forces are also invoved during interfacial interactions [149]. However, the interface with lowest bond length (O-Mg termination) does not have the highest W_R. This is due to the binding behaviour at the O-Mg interface as shown in Fig. 6.4(a) & (c).

Figure 6.4 gives an illustration of contour maps for the charge density difference of the atoms in O-Mg and Ni-O models. Weak ionic bonding can be seen between the interfacial Ni atoms and O atoms in Figures 6.4(b) & (d), while the density difference of O-Mg (Figures 6.4(a) & (c)) reveals weak

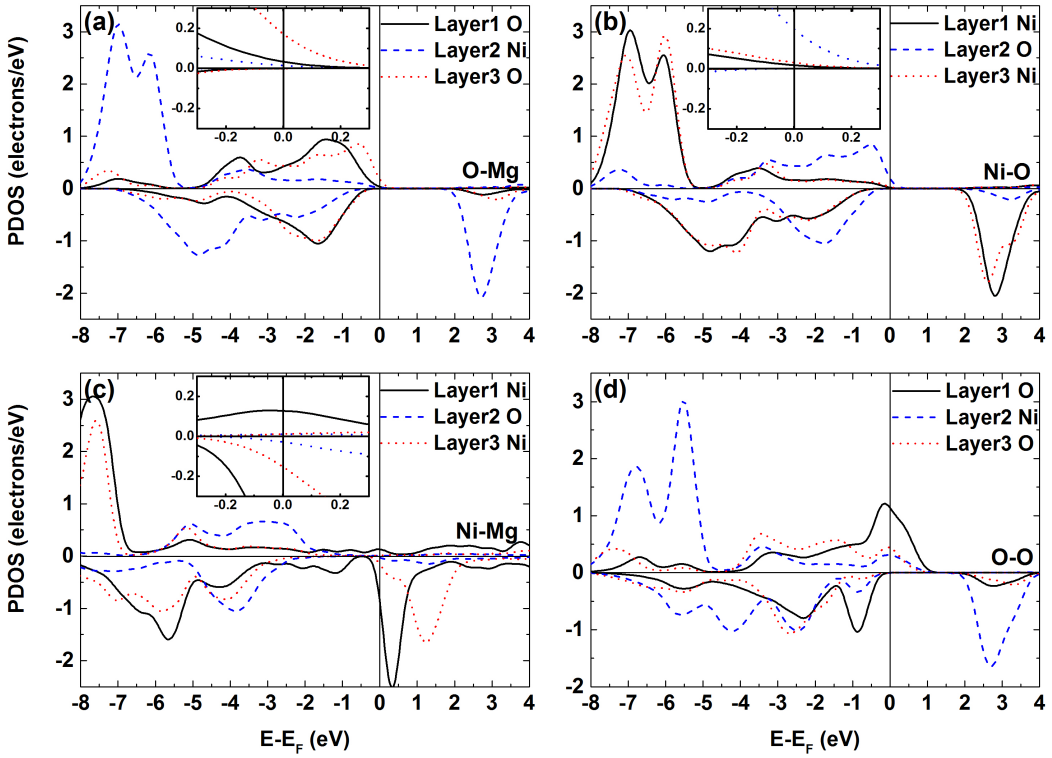

Figure 6.5: Partial density of state plots of the first three layers for the different interface terminations with (a) O-Mg and (b) Ni-O showing half metallicity at the interface. (c) Ni-Mg and (d) Ni-Mg terminations.

ionic bonds with covalent character, which indicates the existence of a coupling interaction. Considering the Mulliken population analysis [150], the bond population of O-Mg interface bond has a higher value of 0.60 when compared with that of Ni-O interface of 0.57. This indicates that the coupling interaction is slightly more between the electronic populations of Mg and O atoms, hence its lower interfacial bond length [151, 152, 153]. The spilling parameter resulting from these calculations is about 0.18%, indicating that the basis set represent the plane wave (PW) states accurately and this population analysis results are reliable [151, 153]. A reduced O-Mg bond length at the interface of magnetic oxide (Fe_3O_4) and MgO was also observed by Lazarov *et al*, when compared with the magnetic element (Fe)-O bond length [154]. Recent work by Lazarov *et al*, on polar oxide NiO(111)/MgO(111) interface arrived at a similar result that this interface is formed with Ni(to Mg) at the interface region [155].

In order to understand the electronic properties of the interface model, the density of states (DOS) and band structure of the optimized supercell was computed. In figure 6.5, I present the layer resolved partial density of states (PDOS) for the first three layers into the NiO slab of the four interface models of NiO/MgO(111). As can be seen there is no notable difference between the PDOS of half-metallic bulk NiO (see fig. 6.6) and these interface layers. Except the Ni-Mg terminated interface, the other interfaces (Ni-O, O-Mg and O-O terminated) show a half-metallic ferromagnetic behavior at the first three layers of the interface of the NiO slab. This is contrary to the report by Huang *et al.*, where a study using full potential linearized augmented plane wave (FP-LAPW) method was used to show that the NiO/MgO(111) interface is metallic and the electronic structures in each interfacial layer is different [156]. The difference observed in the results here and that of the FPLAPW ones is due to the half-metallic bulk NiO used in this study, while in the work of Huang *et al.*, the well known antiferromagnetic ground state of NiO have been used in their calculation. Shown in fig. 6.7 is the bandstructure of Ni-O (a-b) and O-Mg (c-d) interface terminations with unresolved bands. I present these results to show the minority spin gap of 2.05 eV for Ni-O termination (see fig. 6.7(a)) and 2.02 eV for O-Mg terminations (fig. 6.7(c)). The states of the spin up bands are above the fermi-level as can be clearly seen from the insets in fig. 6.5(a-b).

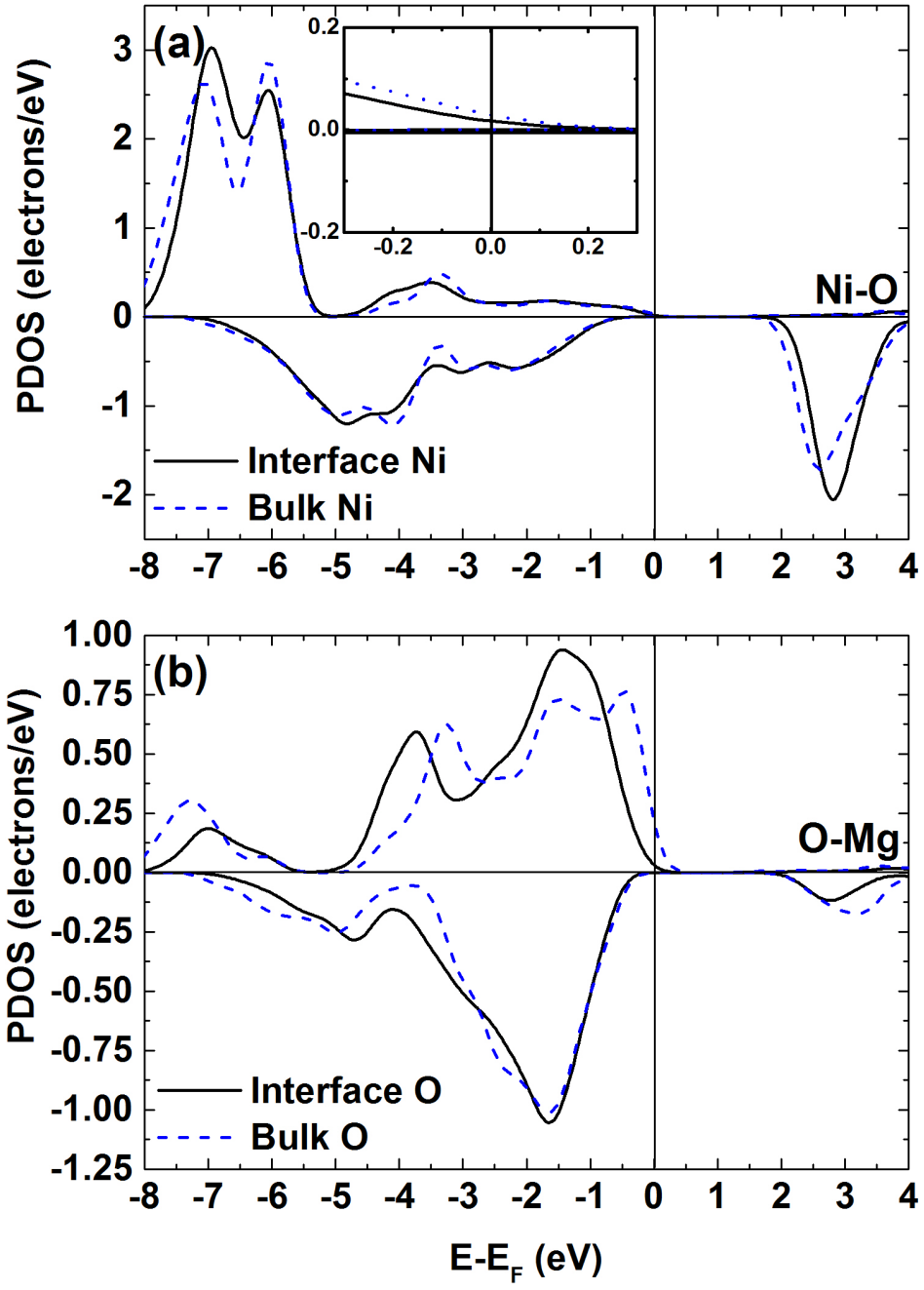

Figure 6.6: Comparison of the atom resolved PDOS of the interface layers with their respective bulk layer in (a) Ni-O and (b) O-Mg interface termination.

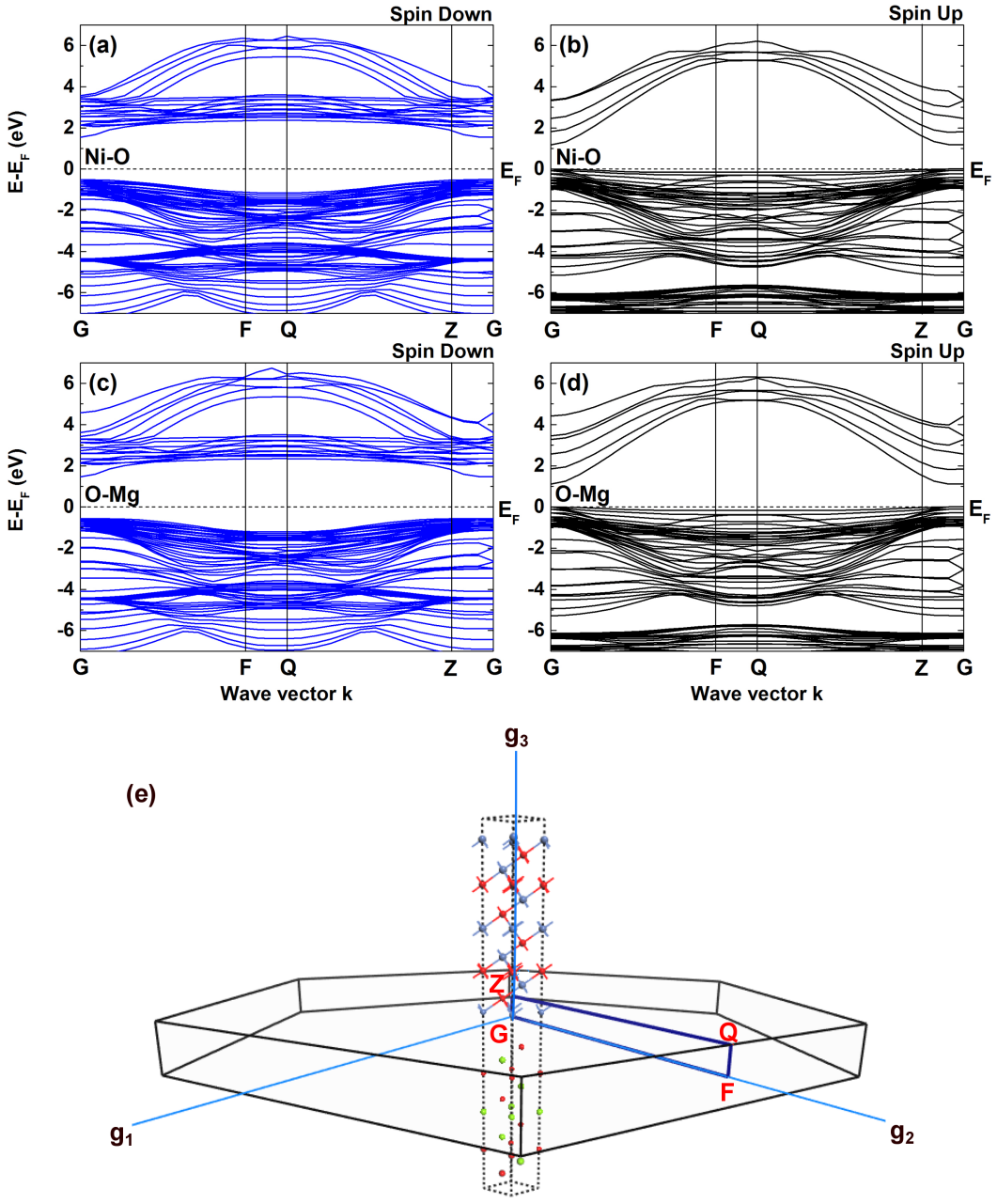

Figure 6.7: Band structure of Ni-O (a-b) and O-Mg (c-d) interface models showing energy gap in the spin down directions. The brillouin zone structure for the hexagonally shaped NiO/MgO(111) supercell is given in (e), with the labels G, F, Q, Z representing the wave vectors high symmetry points.

A look at the changes in magnetic properties of the interface models indicate that the interfacial Ni-O layer of the Ni-O interface termination has a negative moment of -1.84 μ_B. This is the reverse direction of the middle Ni-O layer with bulk-like moment of 2.00 μ_B. The presence of MgO in the stacking geometry results in reorientation of the Ni-O spin moment at the interface and slightly destroys the half-metallicity seen in the bulk (figure 6.2). The total moment for the O-Mg terminated interface was reduced to 1.91 μ_B. Both the p and d orbitals contribute to the close to half metallicity observed in Ni-O termination, while p-p orbital hybridization is responsible for similar behavior in the O-Mg interface.

6.3 NiO/MgO(001)

6.3.1 Models and Computational Method

Here I built a supercell structure of NiO/MgO in the (001) direction from seven (7) atomic layers each of NiO(001) and MgO(001) slabs. To form a uniform multilayered structure the NiO(001) surface lattice is stretched to match that of MgO(001). These new heterostructures are presented in Fig. 6.8 showing the four possible ways of terminating the atoms at the interface of two binary compounds. The four ways are labelled according to the interface atoms on the edge of the cell structure i.e: (a) O-Mg, (b) Ni-O, (c) Ni-Mg and (d) O-O interface terminations. With their in-plane lattice a set to 2.998 Å and a fixed cell structure, the atomic positions were fully relaxed in a geometry optimization calculation using the BFGS method. The Brillouin zone sampling here was done within a 5×5×1 $\boldsymbol{K}$ point grid parameter.

6.3.2 Results

The relaxation of atoms in the layered structures in fig. 6.8 results in an epitaxial growth model with novel features at the interface between NiO(001) and MgO(001) slabs. To analyze the strength of the interface bond and its readiness to form when the interfacial atoms interact, the work of separation is calculated as shown in table 6.3. Also, the measured interlayer bond length and distance after structural optimization is given in this table. From table

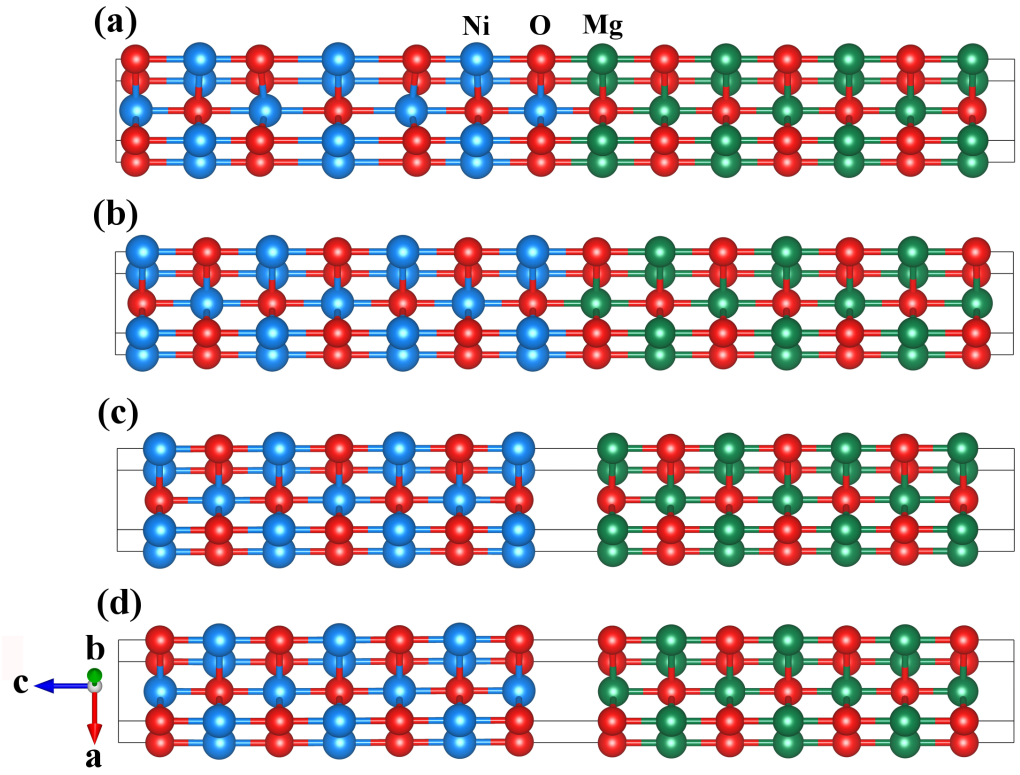

Figure 6.8: Optimized interface terminations of NiO/MgO(001) with (a) O-Mg, (b) Ni-O (c) Ni-Mg and (d) O-O.

6.3, the most favorable structure is the Ni-O terminated interface with the highest work of 1.09 J/m^2. Again, the O-Mg interface termination has the shortest bond length of 2.18 Å for the same reason started earlier. Also the interlayer distances follow a similar trend as the interface bond lengths. The negative values of work of separations in the Ni-Mg and O-O interfaces is an indication that cation-cation or anion-anion bonding at the interface are difficult to form.

Figures 6.9((a) & (c)) shows a 2D slice of the electronic charge differences plot through the interface O-Mg atoms, which indicates that the electrons are concentrated on the oxygen (O) atoms (red regions). While the blue regions around Ni atoms means they are electron deficient. Figures 6.9((b) & (d)) are slices through the interface O-Ni atoms also showing enrichment of electrons around the O atoms and none on the bonds. The electron cloud concentrated on the O atom, indicates there is ionic bonding at the interface.

Table 6.3: The calculated work of separation (W_R), interlayer distances and optimized bond length (L) between the interfacial atoms for the various interface ordering studied.

Interface Termination	**Work of Separation (J/m^2)**	**Interlayer Distance (Å)**	**Interfacial Bond Length (Å)**
Ni-O	1.09	2.25	2.28
Ni-Mg	-0.16	3.30	3.37
O-Mg	0.16	2.24	2.18
O-O	-0.17	3.39	3.33

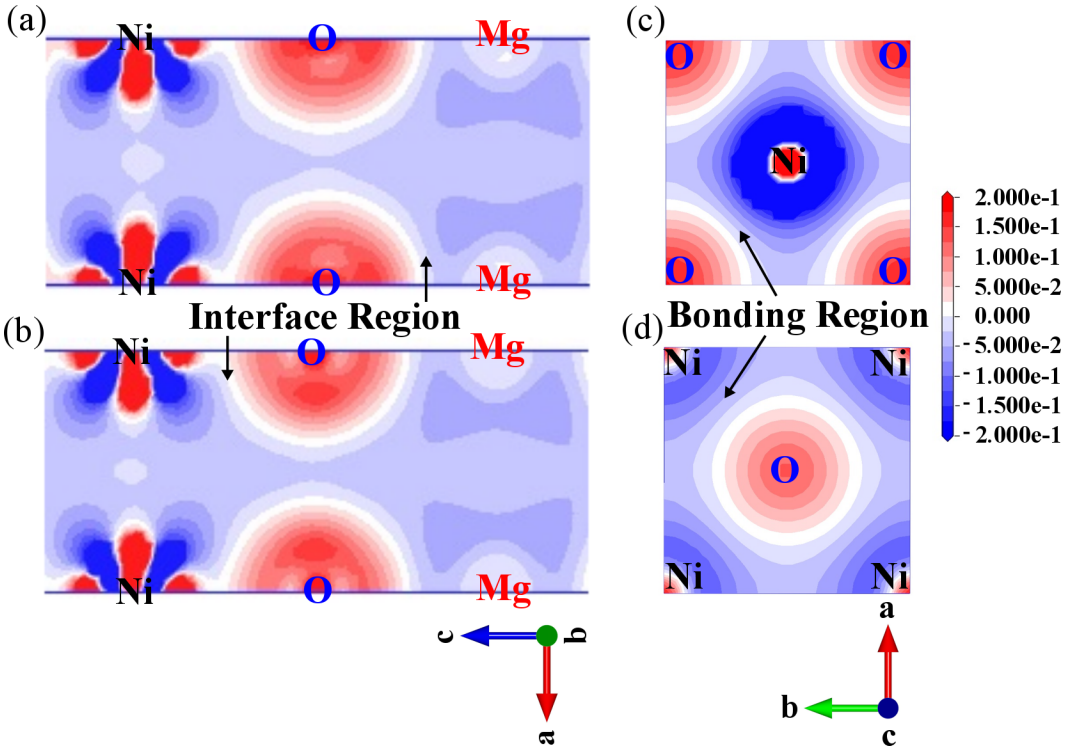

Figure 6.9: Electronic charge density difference of the atoms in O-Mg and Ni-O models sliced at the interface edge; (a) lateral view of O-Mg, (b) lateral view of Ni-O (c) O-Mg viewed along the c-axis and (d) Ni-O viewed along c-axis. Contour maps: electron deficient region in blue, and electron rich region in red. Small changes in electron density is white region. The field values ranges from -0.2 to 0.2 e/Å^2

Now considering the density of states plots in figure 6.10, half-metallicity of bulk-like layers in the middle of the NiO slabs have been destroyed in the Ni-O, Ni-Mg and O-O interface models. The half-metallicity was maintained in the O-Mg model, up until its interface layer. On the other hand, Ni-O termination with better structural stability shows half-metallic antiferromagnetic behavior (see fig. 6.10(b)) at its interface [157, 158]. A half-metallic antiferromagnet has 100% spin polarization of its conduction electrons and a zero net magnetic moment. That is a gap exist in the spin up direction at the Fermi level with 100% spin polarization as seen in figure 6.10(b). To get further insight into this behavior, I look at the Ni-O bilayer forming the interface and the total spin magnetic moment as they interact in the interface region. In fig. 6.11(a) comparing the PDOS of NiO interface layer with that in bulk-like region indicates the half-metallic antiferromagnetism originated from the center and runs through the NiO(001) slab (see fig. 6.10(b)). However the total spin moment is an integer value of 2.00 μ_B, which makes the interface layer a fully compensated half-metallic ferrimagnet. At this interface with Ni-O termination, ferrimagnetism co-exist with the half-metallicity, but its compensation temperature was not computed here. In the case of O-Mg termination given in fig. 6.11(b) a total spin moment of 1.94 μ_B was computed and likewise is not perfectly half-metallic.

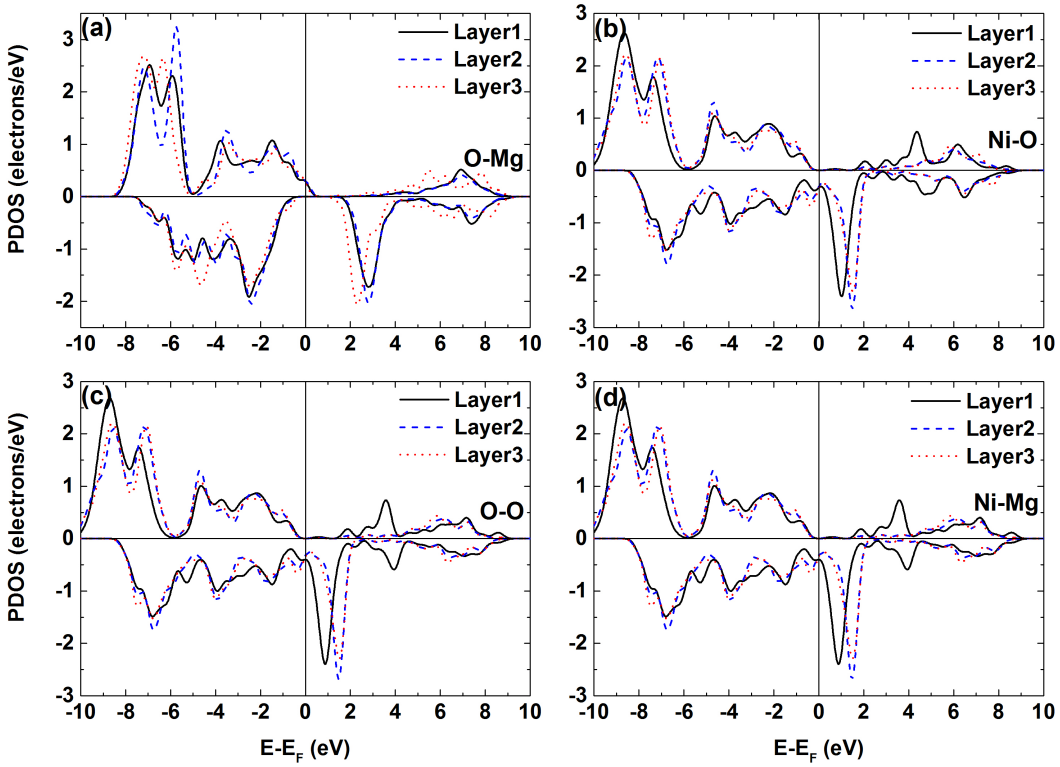

Figure 6.10: Partial density of state plots for the first three layers for the different interface terminations with (a) Mg-O showing half metallicity at the interface. While (b) Ni-O (c) O-O and (d) Ni-Mg terminations are negatively polarized.

6.4 NiO/MgO(110)

6.4.1 Models and Computational Method

The supercell structures in fig. 6.12 were modelled in a similar fashion like those of fig. 6.8 and the same computational details used for simulating the NiO/MgO(001) interfaces were also implemented here. Four hetero-structured models of NiO/MgO(110) interfaces have been made from five and seven layers of NiO(110) and MgO(110) slabs respectively. These are labelled: (a) O-Mg, (b) Ni-O, (c) Ni-Mg and (d) O-O, according to the atoms found at the edge of the cell structure in the interface region shown in fig. 6.12.

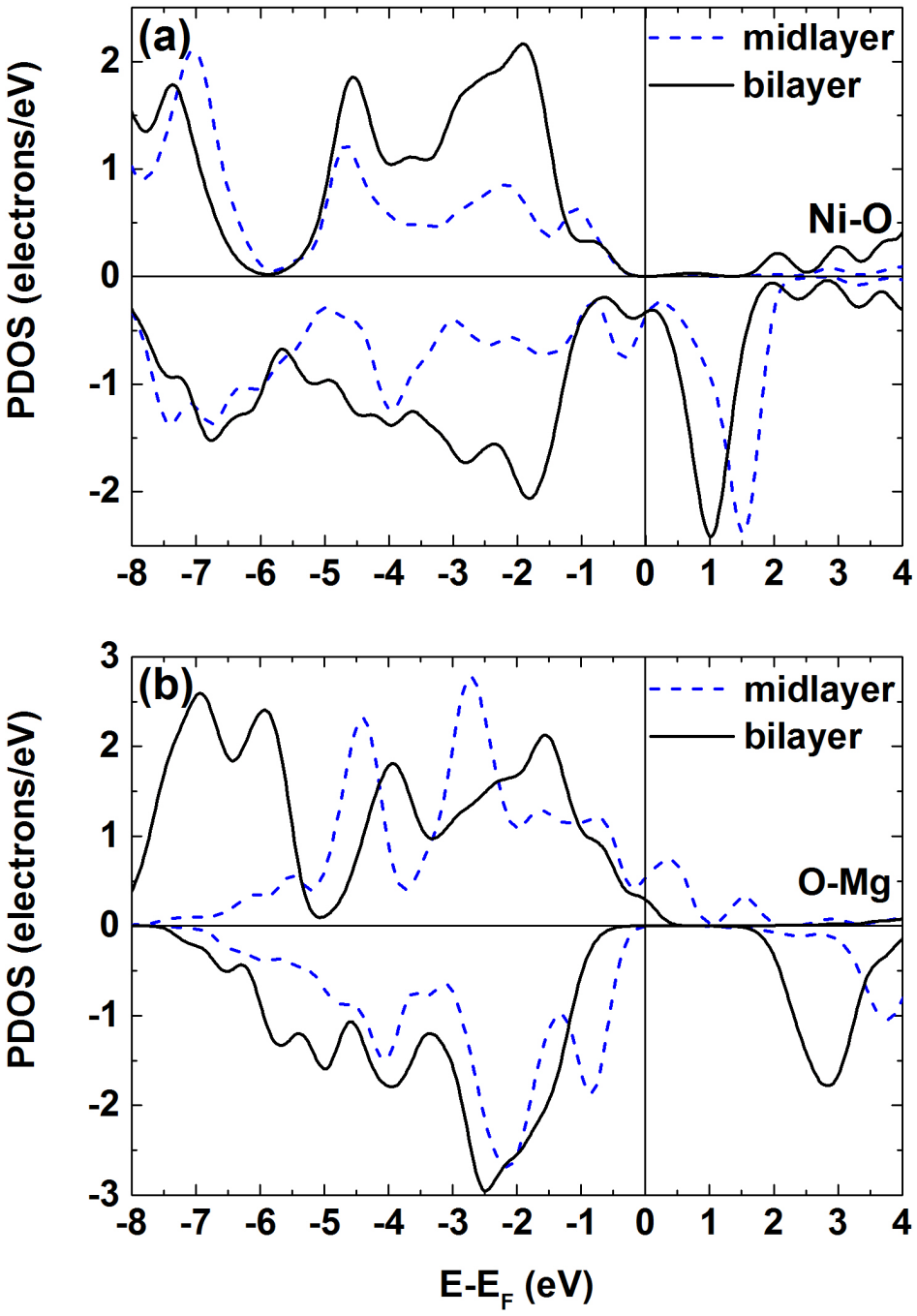

Figure 6.11: PDOS comparison of the bulk-like middle layer of NiO(001) slab with the bilayer forming the interfacial layers of (a) Ni-O and (b) O-Mg interface termination.

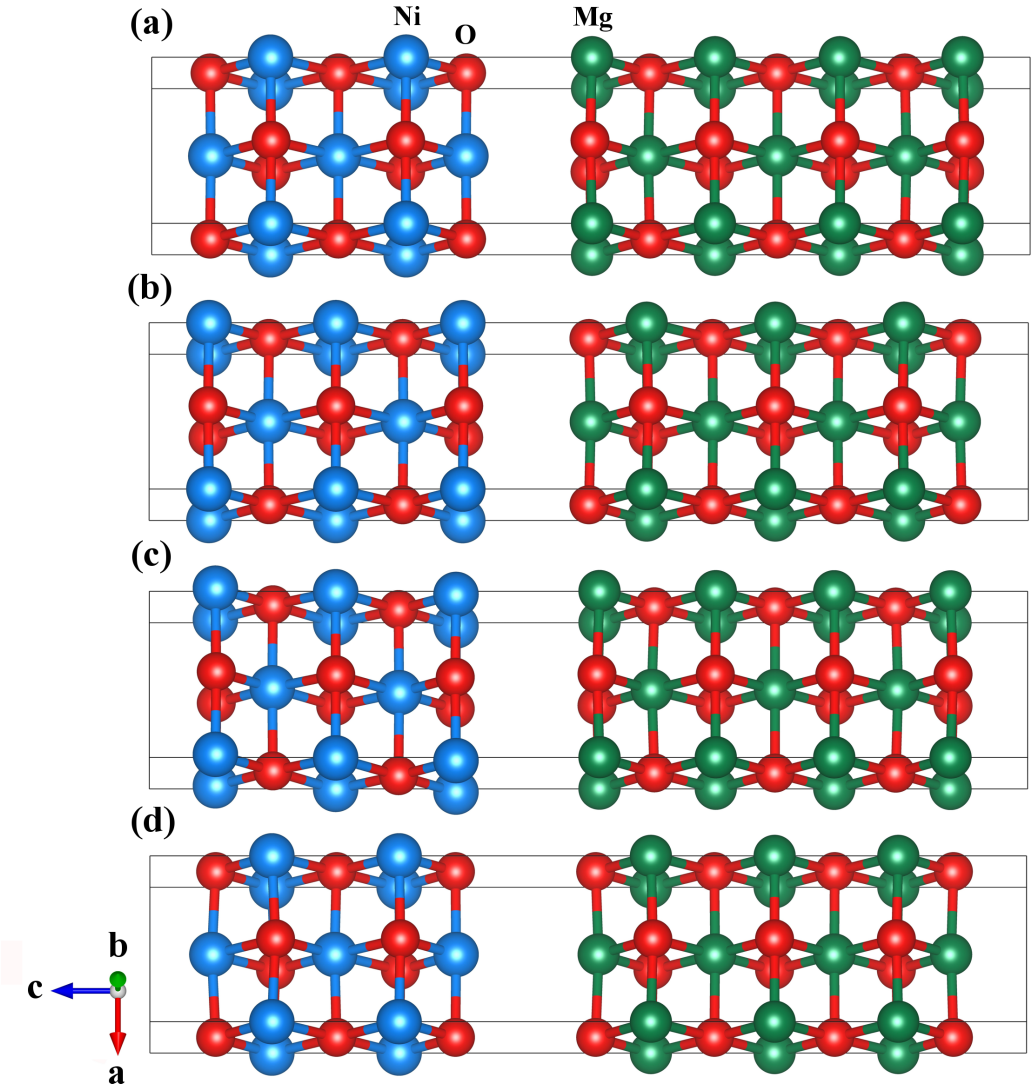

Figure 6.12: Optimized interface terminations of NiO/MgO(110) with (a) O-Mg, (b) Ni-O (c) Ni-Mg and (d) O-O.

6.4.2 Results

After a full geometry optimization of the NiO/MgO(110) structures, allowing the atoms to freely relax we computed the structural properties given in table 6.4. Here we measured interlayer distances greater than the optimum Ni-O or Mg-O bond lengths in all four possible interfacial terminations (O-Mg, Ni-O, Ni-Mg and O-O). The work of separation values are not far from zero, it has a negative value for the Ni-Mg and O-O terminations as before. On the

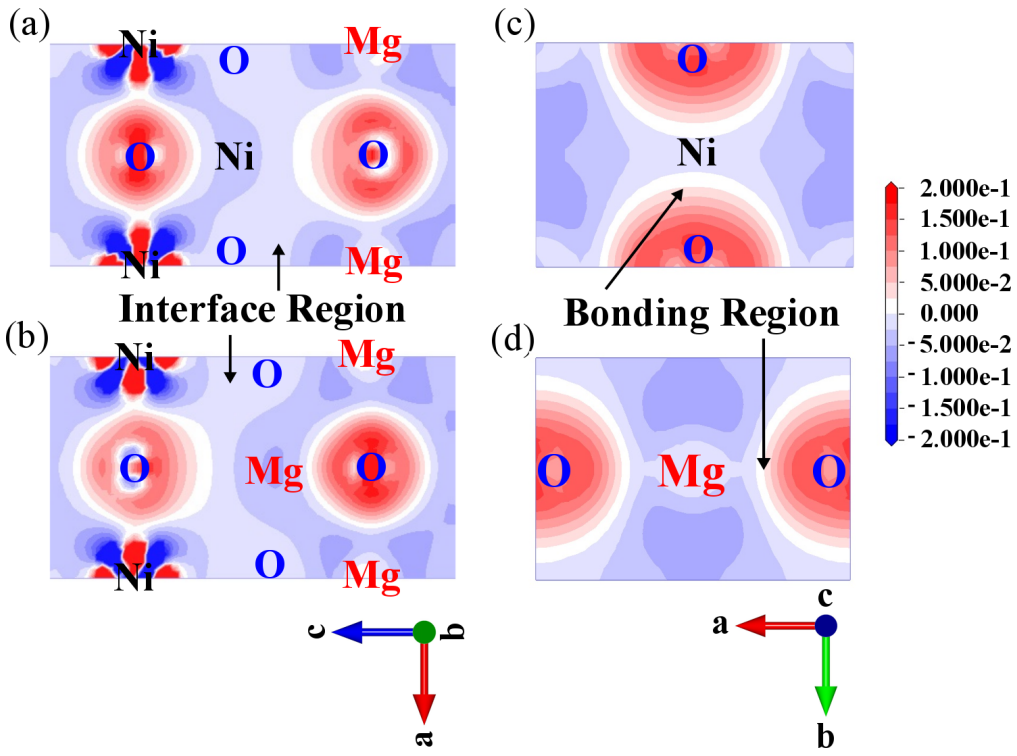

Figure 6.13: Electronic charge density difference of the atoms in O-Mg and Ni-O models sliced at the interface edge; (a) lateral view of O-Mg, (b) lateral view of Ni-O (c) O-Mg viewed along the *c*-axis and (d) Ni-O viewed from the top. Contour maps: electron deficient region in blue, and electron rich regions in red. Small changes in electron density is white region. The field values ranges from -0.2 to 0.2 e/Å^2.

Table 6.4: The calculated work of separation (W) and interlayer distances between the interfacial atoms for the various interface ordering studied.

Interface Termination	**Work of Separation (J/m^2)**	**Interlayer Distance (Å)**
Ni-O	0.62	3.13
Ni-Mg	-0.13	3.56
O-Mg	0.59	3.09
O-O	-0.37	3.46

O-Mg and Ni-O terminated interfaces (see fig.6.12) there seem to be little or no interaction between the interfacial layers, so we went on to look at their charge density difference plots.

Figure 6.13(a) is a 2D slice through the edge of the O-Mg interface termination. With the charge density cloud around O atoms (red regions) and blue electron density cloud around Ni indicates electron pairs are not shared. Figure 6.13(b) is a slice at the edge of the Ni-O structure and figures 6.13(c) & (d) are views from the top through *c*-axis. Looking at the electron density difference plots given in fig. 6.13 for O-Mg and Ni-O interface models, a light-blue to white region of little interaction can be seen on the interface regions. The individual NiO(110) and MgO(110) layers still exhibit ionic bonding in their slabs without much interaction with each other.

Finally, I examined the PDOS near the interface region of NiO/MgO(110) interfaces to note the changes in its electronic properties and the spin magnetic moment for the interface layers was computed as well. These analysis were focused on the NiO(110) slab(s). The PDOS plots depicts some half-metallic antiferromagnetic characteristics as before, for the O-Mg and Ni-O interface terminations (see fig. 6.14). Magnetic moment measurements give a non-zero value, indicating that it is not truly a HMA interface model.

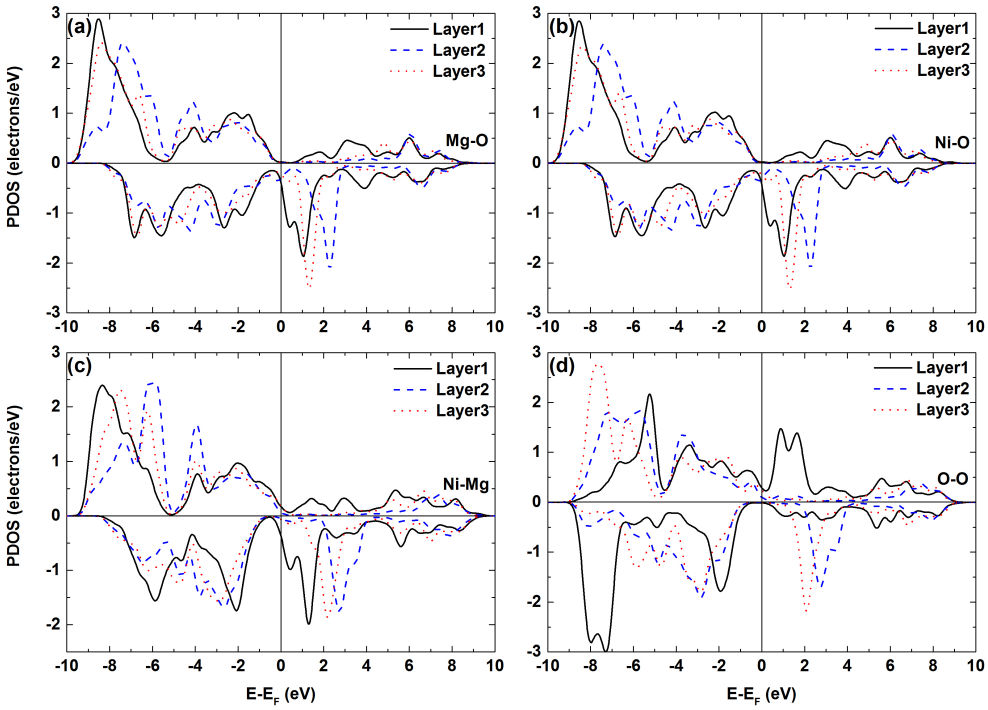

Figure 6.14: Partial density of state plots for the first three layers for the different interface terminations with (a) O-Mg (b) Ni-O (c) Ni-Mg and (d) O-O terminations.

6.5 Summary

The plane-wave pseudo-potential study of the NiO/MgO interfaces indicate that the NiO/MgO(001) and NiO/MgO(110) interfaces have a weak stability based on their adhesion strength. The NiO/MgO(111) interface structure is more favorable for the Ni-O terminated interface. The Ni-O and O-Mg terminated interfaces of the NiO/MgO(111) structures exhibit a half-metallic like characters and comparable structural properties. On the other hand, the same interface terminations for the NiO/MgO(001) and NiO/MgO(110) supercell models behaves like a half-metallic ferrimagnet. Due to possessing high spin polarization, the energetically favourable terminations of Ni-O could be useful for spintronic applications.

Chapter 7

Conclusion

In trying to address the challenges of spin injection in a spintronic device, the structural, electronic and magnetic properties of functional materials interfaces have been investigated using DFT. This work is mainly focussed on modeling interfaces with high spin polarization and Schottky contacts with small lattice mismatch. The first result chapter was dedicated to the *c*-MnSb(111)/InSb(111) interfaces. A work of separation calculation reveals that terminating the interface with Mn atom from *c*-MnSb and Sb atom from the InSb (Mn-Sb terminated) side is energetically more stable than the other interface terminations. This termination also exhibited a high spin polarization of 92.6% and a slight increase in the value of magnetic moment per Mn atom.

A study of the interface models of *n*-MnSb(0001)/InP(111) and *n*-MnSb(0001)/GaAs(111) was carried out in chapter 4. The Mn-P and Mn-As terminated interfaces showed, respectively, an enhanced spin polarization of 63.9% and 61.1% when compared to a *n*-MnSb bulk polarization of about 18%. They are covalently bonded and possess a strong *p*-*d* hybridization. Investigating the structural stability through the calculation of work of separation and measurement of interfacial bond distance show that the Mn-P terminated interface model is energetically more favourable. The behavior at the interface of n-MnSb(0001) when capped with Sb(0001) was looked at in chapter 5. The Sb cap prevented oxidation of the Mn and can grow smoothly on n-MnSb(0001) as indicated by the RHEED, XRD and DFT structural analysis of the interface. At the Sb/*n*-MnSb(0001) interface structure magnetism was maintained

with boosted moment of 3.94 μ_B on Mn atom and a polarization of -57.7% at the Mn-Sb interface was computed. The ferromagnetic/paramagnetic layered structure Sb/*n*-MnSb(0001) could be used in spin transport applications.

In chapter 6, stability calculations showed that the Ni-O termination of the NiO/MgO(111) interface is energetically more favourable than the NiO/MgO(001) and NiO/MgO(110) interfaces. The Ni-O and O-Mg terminations for the NiO/MgO(111) interface have a half-metallic like character. Whereas, these terminations showed a half-metallic antiferromagnet behavior in the NiO/MgO(001) and NiO/MgO(110) interface structures.

In this study I focused on (1×1) surface slabs in the search for new interface systems with interesting properties, mainly due to the computational cost of increasing all three dimensions of a periodic model. However, III-V semiconductor surfaces do reconstruct to energetically favourable form as discussed in section 1.4. Designing models that put into consideration the minimum energy surfaces of these slabs and the preferred absorption site for atoms at the interface would be a good starting point for further works on these interfacial systems.

The interfaces studied have no tunnel barrier and the *c*-MnSb/InSb(111) interface should have a Schottky barrier in one spin direction, i.e the metal / semiconductor junction. Understanding the Schottky barrier height here, will give the interface resistance and the probability of getting spin up or spin down diffusively into the semiconductor. This is important and can be addressed with DFT in the future. There is different effective barrier heights for spin up and spin down, which can be extracted from a DFT calculation.

With an enhanced polarization at the *n*-MnSb(0001)/InP(111) and *n*-MnSb(0001)/GaAs(111) interface, further work focusing on transport related properties such as electrical conductivity can be done. Calculations to support ongoing growth study of MnSb/Sb/MnSb(0001) spin valve structure in the group, which shows promise as a suitable material for making current perpendicular to plane device model could be carried out.

The I-V curves characteristics of NiO/MgO films will be studied using the Korringer-Kohn-Rostoker (KKR) method to determine the nature of its stability. Applications for memory switching requires a stable I-V curve [124, 159]. Their conductivities will be measured and compared to that of bulk NiO

which is between $10^{-15} - 10^{-17}/\Omega cm$ at low temperature [160].

Bibliography

[1] C. Chappert; A. Fert and F. N. Van Dau. *Nat. Mater.*, 6(11):813–823, (2007).

[2] S. A. Wolf; D. D. Awschalom; R. A. Buhrman; J. M. Daughton; S. von Molnar; M. L. Roukes; A. Y. Chtchelkanova and D. M. Treger. *Science*, 294(5546):1488–1495, (2001).

[3] F. Mikailzade. *Nanomagnetism and SpintroSpin: Fabrication, Materials, Characterization and Applications*. World Scientific Publishing Co. Pte. Ltd., (2011).

[4] T. Shinjo. *Nanomagnetism and Spintronics*. Elsevier B.V, (2009).

[5] K. Y. Camsari; S. Ganguly and S. Datta. *Sci. Rep.*, 5:10571, (2015).

[6] J. D. Aldous; C. W. Burrows; A. M. Sánchez; R. Beanland; I. Maskery; M. K. Bradley; M. d S. Dias; J. B. Staunton and G. R. Bell. *Phys. Rev. B*, 85(6), (2012).

[7] S. J. Jenkins. *Phys. Rev. B*, 70(245401), (2004).

[8] A. Fert. *Rev. Mod. Phys.*, 80, (2008).

[9] S. Datta and B. Das. *Appl. Phys. Lett.*, 56(7):665–667, (1990).

[10] I. Galanakis and P. H. Dederichs, editors. *Half-Metallic Alloys: Fundamentals and Applications.* Springer-Verlag, Berlin, (2005).

[11] C. Y. Fong; J. E. Pask and L. H. Yang. *Half-Metallic Materials and Their Properties*. World Scientific Publishing Co. Pte. Ltd., Singapore, (2013).

[12] J. D. Aldous; C. W. Burrows; I. Maskery; M. S. Brewer; T. P. A. Hase; J. A. Duffy; M. R. Lees; C. Sánchez-Hanke; T. Decoster; W. Theis; A. Quesada; A. K. Schmid and G. R. Bell. *J. Phys.: Condens. Matter*, 24(14):146002, (2012).

[13] G. Schmidt; D. Ferrand; L. W. Molenkamp; A. T. Filip and B. J. van Wees. *Phys. Rev. B*, 62(8):R4790–R4793, (2000).

[14] S.A. Hatfield and G.R. Bell. *J. Cryst. Growth*, 296(2):165–173, (2006).

[15] J. Tang and K. L. Wang. *Nanoscale*, 7(10):4325–4337, (2015).

[16] J. J. Attema; G. A. de Wijs and R. A. de Groot. *J. Phys. D: Appl. Phys.*, 39(5):793–796, (2006).

[17] T. Jungwirth; X. Marti; P. Wadley and J. Wunderlich. *Nature Nanotech*, 11(3):231–241, (2016).

[18] F. L. A. Machado; P. R. T. Ribeiro; J. Holanda; R. L. Rodríguez-Suárez; A. Azevedo and S. M. Rezende. *Phys. Rev. B*, 95(10), (2017).

[19] D. C. Ralph and M. D. Stiles. *J. Magn. Magn. Mater.*, 320(7):1190–1216, (2008).

[20] W. S. Zhao; T. Devolder; Y. Lakys; J. O. Klein; C. Chappert and P. Mazoyer. *Microelectron. Reliab.*, 51(9-11):1454–1458, (2011).

[21] T. Kawahara; K. Ito; R. Takemura and H. Ohno. *Microelectron. Reliab.*, 52(4):613–627, (2012).

[22] R. J. Soulen-Jr.; J. M. Byers; M. S. Osofsky; B. Nadgorny; T. Ambrose; S. F. Cheng; P. R. Broussard; C. T. Tanaka; J. Nowak; J. S. Moodera; A. Barry and J. M. D. Coey. *Science*, 282:85, (1998).

[23] I. I. Mazin. *Phys. Rev. Lett.*, 83(7):1427–1430, (1999).

[24] E. Sartipi; A. Hojabri; A. Bouchani and M. H. Shakib. *Chin. J. Chem. Phys.*, 24(2):155–161, (2011).

[25] W. S. Yun; J. Choi; G. B. Cha; S. Cho and S. C. Hong. *J. of the Kor. Phy. Soc.*, (2006).

[26] J. M. K. Al zyadi; G.Y. Gao and K-L. Yao. *Thin Solid Films*, 531:266–270, (2013).

[27] J. E. Pask; L. H. Yang; C. Y. Fong; W. E. Pickett and S. Dag. *Phys. Rev. B*, 67(22), (2003).

[28] R. A. de Groot; F. M. Mueller; P. G. van Engen and K. H. J. Buschow. *Phys. Rev. Lett.*, 50(25):2024–2027, (1983).

[29] J. M. D. Coey and M. Venkatesan. *J. Appl. Phys.*, 91(10):8345, (2002).

[30] W. E. Pickett and H. Eschrig. *J. Phys.: Condens. Matter*, 19(315203), 2007.

[31] I. Galanakis; P. H. Dederichs and N. Papanikolaou. *Phys. Rev. B*, 66(134428), 2002.

[32] J. Kubler. *Physica B*, 127:257–263, (1984).

[33] S. Mollet and S. J. Jenkins. *J. Phys.: Condens. Matter*, 19(315214), (2007).

[34] S. C. Rasmussen. The 18-electron rule and electron counting in transition metal compounds: theory and application. *ChemTexts*, 1(1), (2015).

[35] G.P. Srivastava. *Appl. Surf. Sci.*, 252(21):7600–7607, (2006).

[36] J. Robertson and L. Lin. Gaas: Gap state passivation at interfaces and surfaces. In *2010 International Electron Devices Meeting*. Institute of Electrical and Electronics Engineers (IEEE), (2010).

[37] P. W. Tasker. *J. Phys. C: Solid State Phys.*, 12(22):4977–4984, (1979).

[38] C. W. Burrows. *Growth and Characterization of MnSb Thin Films and Interfaces*. PhD thesis, University of Warwick, (2012).

[39] M. D. Pashley. *Phys. Rev. B*, 40(15):10481–10487, (1989).

[40] D. J. Chadi. *Phys. Rev. Lett.*, 52(21):1911–1914, (1984).

[41] L. Zhang; E. G. Wang; Q. K. Xue; S. B. Zhang and Z. Zhang. *Phys. Rev. Lett.*, 97(12), (2006).

[42] E. Engel and R. M. Dreizler. *Density Functional Theory: An Advanced Course.* Springer-Verlag, Berlin, (2011).

[43] D. S. Sholl and J. A. Steckel. *Density Functional Theory: A Practical Introduction.* John Wiley & Sons, Inc., Hoboken, New Jersey, (2009).

[44] J. M. Wills; M. Alouani; P. Anderson; A. Delin; O. Eriksson and O. Grechnyev. *Full-Potential Electronic Structure Method: Energy and Force Calculation with Density Functional and Dynamical Mean Field Theory.* Springer-Verlag, Berlin, (2010).

[45] R. O. Jones. *Rev. Mod. Phys.*, 87(3):897–923, (2015).

[46] P. Hohenberg and W. Kohn. *Phys. Rev.*, 136(3B):B864–B871, (1964).

[47] W. Kohn and L. J. Sham. *Phys. Rev.*, 140(4A):A1133–A1138, (1965).

[48] V. Ozolins and M. Korling. *Phys. Rev. B*, 48(24):18304–18307, (1993).

[49] J. P. Perdew; J. A. Chevary; S. H. Vosko; K. A. Jackson; M. R. Pederson; D. J. Singh and C. Fiolhais. *Phys. Rev. B*, 46(11):6671–6687, (1992).

[50] B. Hammer; K. W. Jacobsen and J. K. Norskov. *Phys. Rev. Lett.*, 70(25):3971–3974, (1993).

[51] D. R. Hamann. *Phys. Rev. Lett.*, 76(4):660–663, (1996).

[52] A. D. Becke. *J. Chem. Phys.*, 96(3):2155–2160, (1992).

[53] J. P. Perdew and Y. Wang. *Phys. Rev. B*, 33(12):8800–8802, (1986).

[54] M. Levy and J. P. Perdew. *Phys. Rev. A*, 32(4):2010–2021, (1985).

[55] J. P. Perdew. *Phys. Rev. Lett.*, 55(21):2370–2370, (1985).

[56] J. P. Perdew and S. Kurth. *A Primer in Density Functional Theory.* Springer-Verlag, Berlin Heidelberg, (2003).

[57] J. P. Perdew; K. Burke and M. Ernzerhof. *Phys. Rev. Lett.*, 77(18):3865–3868, (1996).

[58] J. P. Perdew; K. Burke and Y. Wang. *Phys. Rev. B*, 54(16533), (1996).

[59] Y. Wang and J. P. Perdew. *Phys. Rev. B*, 43(11):8911–8916, (1991).

[60] V. I. Anisimov; J. Zaanen and O. K. Andersen. *Phys. Rev. B*, 44(3):943–954, (1991).

[61] M. Cococcioni and S. de Gironcoli. *Phys. Rev. B*, 71(035105), (2005).

[62] B. Himmetoglu; A. Floris; S. de Gironcoli and M. Cococcioni. *Int. J. Quantum Chem.*, 114(1):14–49, (2013).

[63] W. B. Zhang; N. Yu; W. Y. Yu and B. Y. Tang. *The Euro. Phy. J. B*, 64(2):153–158, (2008).

[64] V. I. Anisimov; F. Aryasetiawan and A. I. Lichtenstein. *J. Phys.: Condens. Matter*, 9:767–808, 1997.

[65] H. Ebert; D. Kodderitzsch and J. Minar. *Rep. Prog. Phys.*, 74(9):096501, (2011).

[66] M. C. Payne; M. P. Teter; D. C. Allan; T. A. Arias and J. D. Joannopoulos. *Rev. Mod. Phys.*, 64(4):1045–1097, (1992).

[67] D. Vanderbilt. *Phys. Rev. B*, 41(11):7892–7895, (1990).

[68] K. Laasonen; A. Pasquarello; R. Car; C. Lee and D. Vanderbilt. *Phys. Rev. B*, 47(16):10142–10153, (1993).

[69] R. Fletcher. *Practical Methods of Optimization.* John Wiley & Sons, Inc., New York, 2nd edition, (1987).

[70] T. H. Fischer and J. Almlof. *The J. of Phys. Chem.*, 96(24):9768–9774, (1992).

[71] B. G. Pfrommer; M. Côté; S. G. Louie and M. L. Cohen. *J. Comput. Phys.*, 131(1):233–240, (1997).

[72] S. J. Clark; M. D. Segall; C. J. Pickard; P. J. Hasnip; M. I. J. Probert; K. Refson and M. C. Payne. *Zeitschrift fr Kristallographie - Crystalline Materials*, 220(5/6), (2005).

[73] Dassault-Systemes; BIOVA. *Materials Studio 5.0*. Dassault Systemes, San Diego, (2009).

[74] M. W. Finnis. *J. Phys.: Condens. Matter*, 8(32):5811, (1996).

[75] D. J. Siegel; L. G. Hector and J. B. Adams. *Phys. Rev. B*, 67(9), (2003).

[76] R-J. Zhang; U. Eckern and U. Schwingenschlgl. *ACS Appl. Mater. Interfaces*, 6(16):14516–14521, (2014).

[77] H. Akinaga; T. Manago and M. Shirai. *Jpn. J. Appl. Phys.*, 39(Part 2, No. 11B):L1118–L1120, (2000).

[78] H. Akinaga and M. Mizuguchi. *J. Phys.: Condens. Matter*, 16(48):S5549–S5553, (2004).

[79] M. I. Katsnelson; V. Yu. Irkhin; L. Chioncel; A. I. Lichtenstein and R. A. de Groot. *Rev. Mod. Phys.*, 80(2):315–378, (2008).

[80] W-H. Xie; Y-Q. Xu; B-G. Liu and D. G. Pettifor. *Phys. Rev. Lett.*, 91(3), (2003).

[81] Q. Wu; Z. Wang; S. Fan and Kailun Yao. *J. Magn. Magn. Mater.*, 368:44–48, (2014).

[82] A. K. Das; C. Pampuch; A. Ney; T. Hesjedal; L. Dweritz; R. Koch and K. H. Ploog. *Phys. Rev. Lett.*, 91(8), (2003).

[83] B. Sanyal; L. Bergqvist and O. Eriksson. *Phys. Rev. B*, 68(5), (2003).

[84] H. C. Jeon; T. W. Kang; Sh. U. Yuldashev; T. W. Kim and S. Jin. *Appl. Phys. Lett.*, 89(11):112517, (2006).

[85] M. Mizuguchi; H. Akinaga; T. Manago; K. Ono; M. Oshima and M. Shirai. *J. Magn. Magn. Mater.*, 239(1-3):269–271, (2002).

[86] J. H. Zhao; F. Matsukura; K. Takamura; E. Abe; D. Chiba and H. Ohno. *Appl. Phys. Lett.*, 79(17):2776, (2001).

[87] V. H. Etgens; P. C. de Camargo; M. Eddrief; R. Mattana; J. M. George and Y. Garreau. *Phys. Rev. Lett.*, 92(16):167205, (2004).

[88] P. Mavropoulos; M. Ležaić and S. Blgel. *Phys. Rev. B*, 72(17):174428, (2005).

[89] Z. Nedelkoski; P. J. Hasnip; A. M. Sanchez; B. Kuerbanjiang; E. Higgins; M. Oogane; A. Hirohata; G. R. Bell and V. K. Lazarov. *Appl. Phys. Lett.*, 107(21):212404, (2015).

[90] S. G. Loui; S. Froyen and M. L. Cohen. *Phys. Rev. B*, 26(4):1738–1742, (1982).

[91] H. J. Monkhorst and J. D. Pack. *Phys. Rev. B*, 13(12):5188–5192, (1976).

[92] F. Birch. *Phys. Rev.*, 71(11):809–824, (1947).

[93] F. D. Murnaghan. *Pro. of the Nat. Acad. of Sci.*, 30(9):244–247, (1944).

[94] I. N. Remediakis and E. Kaxiras. *Phys. Rev. B*, 59(8):5536–5543, (1999).

[95] H. H. Landolt; R. Bornstein; K-H. Hellwege; O. Madelung; M. Schulz; H. Weiss and D. Bimberg. *Numerical data and functional relationships in science and technology : new series / Group III, Crystal and solid state physics, Semiconductors, Physics of group IV elements and III-V compounds*, volume 17a. Berlin: Springer, (1982).

[96] I. Vurgaftman; J. R. Meyer and L. R. Ram-Mohan. *J. Appl. Phys.*, 89(11):5815, (2001).

[97] J-C. Zheng and J. W. Davenport. *Phys. Rev. B*, 69(14), (2004).

[98] G. R. Bell; C. W. Burrows; T. P. A. Hase; M. J. Ashwin; S. R. C. McMitchell; A. M. Sanchez and J. D. Aldous. *SPIN*, 04(04):1440025, (2014).

[99] I. Galanakis and P. Mavropoulos. *Phys. Rev. B*, 67(10), (2003).

[100] N. Liu; G.Y. Gao; J.B. Liu and K.L. Yao. *Comput. Mat. Sci.*, 95:557–562, (2014).

[101] A. Yelisseyev; Z. S. Lin; M. Starikova; L. Isaenko and S. Lobanov. *J. Appl. Phys.*, 111(11):113507, (2012).

[102] A.V. Kolobov; M. Krbal; P. Fons; J. Tominaga and T. Uruga. *Nat. Chem.*, 3(4):311–316, (2011).

[103] S. Sanvito and N. A. Hill. *Phys. Rev. B*, 62(23):15553–15560, (2000).

[104] A. Continenza S. Picozzi and A. J. Freeman. *J. Appl. Phys.*, 94:4723, (2003).

[105] K. Nagao; Y. Miura and M. Shirai. *Phys. Rev. B*, 73:104447, (2006).

[106] I. Galanakis; M. Ležaić; G. Bihlmayer and S. Blgel. *Phys. Rev. B*, 71(21), (2005).

[107] K. Lawniczak-Jablonska; A. Wolska; J. Bak-Misiuk; E. Dynowska; P. Romanowski; J. Z. Domagala; R. Minikayev; D. Wasik; M. T. Klepka; J. Sadowski; A. Barcz; P. Dluzewski; S. Kret; A. Twardowski; M. Kaminska; A. Persson; D. Arvanitis; E. Holub-Krappe and A. Kwiatkowski. *J. Appl. Phys.*, 106(8):083524, (2009).

[108] K. H. Ploog. *J. Appl. Phys.*, 91:7256, (2002).

[109] O. Rader; A. Kimura; N. Kamakura; K-S. An; A. Kakizaki; S. Miyanishi; H. Akinaga; M. Shirai; K. Shimada and A. Fujimori. *Phys. Rev. B*, 57(2):R689–R692, (1998).

[110] N. Wiberg; A. F. Holleman and E. Wiberg. *Holleman-Wiberg's Inorganic Chemistry*. Academic Press, (2001).

[111] R. M. Biefeld. *Mat. Sci. and Eng.: R: Reports*, 36(4):105–142, (2002).

[112] B. R. Bennett; R. Magno; J. B. Boos; W. Kruppa and M. G. Ancona. *Solid-State Electron.*, 49(12):1875–1895, (2005).

[113] S. A. Hatfield and G. R. Bell. *Surf. Sci.*, 601:5368–5377, (2007).

[114] A. R. Babar; S. S. Shinde; A. V. Moholkar; C. H. Bhosale; J. H. Kim and K. Y. Rajpure. *J. Alloys Compd.*, 505(2):416–422, (2010).

[115] W. Mao; B. Xiong; Y. Liu and C. He. *Appl. Phys. Lett.*, 103(3):031915, (2013).

[116] N. Farahi; M. VanZant; J. Zhao; J. S. Tse; S. Prabhudev; G. A. Botton; J. R. Salvador; F. Borondics; Z. Liu and H. Kleinke. *Dalton Trans.*, 43(40):14983–14991, (2014).

[117] T. Komesu; C. N. Borca; H-K. Jeong; P. A. Dowben; D. Ristoiu; J. P. Nozieres; S. Stadler and Y. U. Idzerda. *Phys. Lett. A*, 273:245–251, (2000).

[118] J. D. Aldous. *Growth, characterisation and surface structures of MnSb and NiSb thin films.* PhD thesis, University of Warwick, 2011.

[119] C. S. Barrett; P. Cucka and K. Haefner. *Acta Cryst.*, 16:451, (1963).

[120] J. Donohue. *The Structure of the Elements.* R. E. Krieger Publishing Co., Malabar, Flo., 1982.

[121] C. W. Burrows; A. Dobbie; M. Myronov; T. P. A. Hase; S. B. Wilkins; M. Walker; J. J. Mudd; I. Maskery; M. R. Lees; C. F. McConville; D. R. Leadley and G. R. Bell. *Cryst. Growth Des.*, 13(11):4923–4929, (2013).

[122] M. D. Irwin; D. B. Buchholz; A. W. Hains; R. P. H. Chang and T. J. Marks. *Proceedings of the Nat. Acad. of Sci.*, 105(8):2783–2787, (2008).

[123] J. Sullaphen; K. Bogle; X. Cheng; J. M. Gregg and N. Valanoor. *Appl. Phys. Lett.*, 100(20):203115, (2012).

[124] S. H. Phark; R. Jung; Y. J. Chang; T. W. Noh and D.-W. Kim. *Appl. Phys. Lett.*, 94(2):022906, (2009).

[125] X. Cheng; J. Sullaphen; M. Weyland; H. Liu and N. Valanoor. *APL Materials*, 2(3):032109, (2014).

[126] M. Kawai; K. Ito and Y. Shimakawa. *Appl. Phys. Lett.*, 95(1):012109, (2009).

[127] Y. Nishi and T. Kimoto. *J. Appl. Phys.*, 120(11):115308, (2016).

[128] S. R. Lee; K. Char; D. C. Kim; R. Jung; S. Seo; X. S. Li; G.-S. Park and I. K. Yoo. *Appl. Phys. Lett.*, 91(20):202115, (2007).

[129] T. Shang; Q. F. Zhan; H. L. Yang; Z. H. Zuo; Y. L. Xie; L. P. Liu; S. L. Zhang; Y. Zhang; H. H. Li; B. M. Wang; Y. H. Wu; S. Zhang and R-W. Li. *Appl. Phys. Lett.*, 109(3):032410, (2016).

[130] R. H. Kodama; S. A. Makhlouf and A. E. Berkowitz. *Phys. Rev. Lett.*, 79(7):1393–1396, (1997).

[131] J. Park; E. Kang; S. U. Son; H. M. Park; M. K. Lee; J. Kim; K. W. Kim; H. J. Noh; J.-H. Park; C. J. Bae; J.-G. Park and T. Hyeon. *Adv. Mater.*, 17(4):429–434, (2005).

[132] R. Q. Wu; Y. P. Feng; Y. F. Ouyang; P. Zhou and C. H. Hu. *J. Appl. Phys.*, 104(4):046103, (2008).

[133] D. Kodderitzsch; W. Hergert; Z. Szotek and W. M. Temmerman. *Phys. Rev. B*, 68(12), (2003).

[134] A. A. Serga; A. V. Chumak and B. Hillebrands. *J. Phys. D: Appl. Phys.*, 43(26):264002, (2010).

[135] T. Moriyama; S. Takei; M. Nagata; Y. Yoshimura; N. Matsuzaki; T. Terashima; Y. Tserkovnyak and T. Ono. *Appl. Phys. Lett.*, 106(16):162406, (2015).

[136] I. M. Miron; K. Garello; G. Gaudin; P.-J. Zermatten; M. V. Costache; S. Auffret; S. Bandiera; B. Rodmacq; A. Schuhl and P. Gambardella. *Nature*, 476(7359):189–193, (2011).

[137] C. Martinez-Boubeta. Coverage effects on the magnetism of fe/MgO(001) ultrathin films. Technical report, (2004).

[138] O. Robach; G. Renaud and A. Barbier. *Phys. Rev. B*, 60(8):5858–5871, (1999).

[139] C. Caspers; A. Gloskovskij; W. Drube; C. M. Schneider and M. Mller. *Phys. Rev. B*, 88(24), (2013).

[140] M.-A. Leroy; A. M. Bataille; F. Bertran; P. Le Fèvre; A. Taleb-Ibrahimi and S. Andrieu. *Phys. Rev. B*, 88(20), (2013).

[141] N Munjal; P Bhambhani; G Sharma; V Vyas and B K Sharma. *J. Phys. Conf. Ser.*, 377:012067, jul (2012).

[142] A. Rohrbach; J. Hafner and G. Kresse. *Phys. Rev. B*, 69(7), (2004).

[143] V. Bellini; L. Di Giustino and F. Manghi. *Phys. Rev. B*, 76(21), (2007).

[144] W-B. Zhang; Y-L. Hu; K-L. Han and B-Y. Tang. *J. Phys.: Condens. Matter*, 18(42):9691–9701, (2006).

[145] J. Yang; B. Li; J. Wang; L. Chen and R. Li. *J. Phys.: Condens. Matter*, 22(1):015003, (2009).

[146] D. D. Koelling and B. N. Harmon. *J. Phys. C: Solid State Phys.*, 10(16):3107–3114, (1977).

[147] A. R. Oganov; M. J. Gillan and G. D. Price. *J Chem Phys*, 118(22):10174–10182, (2003).

[148] M. D. Irwin; J. D. Servaites; D. B. Buchholz; B. J. Leever; J. Liu; J. D. Emery; M. Zhang; J-H. Song; M. F. Durstock; A. J. Freeman; M. J. Bedzyk; M. C. Hersam; R. P. H. Chang; M. A. Ratner and T. J. Marks. *Chem. Mater.*, 23(8):2218–2226, (2011).

[149] D. S. Rimai; L. P. DeMejo and K. L. Mittal, editors. *Fundamentals of Adhesion and Interfaces*. VSP BV, The Netherlands, 1995.

[150] R. S. Mulliken. *The J. of Chem. Physics*, 23(10):1833, (1955).

[151] M. D. Segall; R. Shah; C. J. Pickard and M. C. Payne. *Phys. Rev. B*, 54(23):16317–16320, (1996).

[152] B. Winkler; C. J. Pickard; M. D. Segall and V. Milman. *Phys. Rev. B*, 63(21), (2001).

[153] M. D. Segall; C. J. Pickard; R. Shah and M. C. Payne. *Mol. Phys.*, 89(2):571–577, (1996).

[154] V. K. Lazarov; M. Weinert; S. A. Chambers and M. Gajdardziska-Josifovska. *Phys. Rev. B*, 72(19), (2005).

[155] V. K. Lazarov; D. Gilks; L. Lari; P. J. Hasnip; K. Matsuzaki; H. Hosono and T. Susaki. Number 1091, (2012).

[156] H. M. Huang; S. J. Luo and K. L. Yao. *Comput. Mater. Sci.*, 50(1):198–202, (2010).

[157] H. van Leuken and R. A. de Groot. *Phys. Rev. Lett.*, 74(7):1171–1173, (1995).

[158] K. zdogan and I. Galanakis. *J. Magn. Magn. Mater.*, 321(15):L34–L36, (2009).

[159] D. C. Kim; M. J. Lee; S. E. Ahn; S. Seo; J. C. Park; I. K. Yoo; I. G. Baek; H. J. Kim; E. K. Yim; J. E. Lee; S. O. Park; H. S. Kim; U-In Chung; J. T. Moon and B. I. Ryu. *Appl. Phys. Lett.*, 88(23):232106, (2006).

[160] M. D. Towler; N. L. Allan; N. M. Harrison; V. R. Saunders; W. C. Mackrodt and E. Aprà. *Phys. Rev. B*, 50(8):5041–5054, (1994).